First-principles Investigation of Small Polarons in Metal Oxides

Dissertation

zur Erlangung des akademischen Grades

Doctor rerum naturalium
(Dr. rer. nat.)

im Fach: Physik

Spezialisierung: Theoretische Physik

eingereicht an der Mathematisch-Naturwissenschaftlichen Fakultät
der Humboldt-Universität zu Berlin

von

M.Sc. Sebastian Kokott

Präsidentin der Humboldt-Universität zu Berlin:
Prof. Dr.-Ing. Dr. Sabine Kunst

Dekan der Mathematisch-Naturwissenschaftlichen Fakultät:
Prof. Dr. Elmar Kulke

Gutachter/innen:
1. Prof. Dr. Matthias Scheffler
2. Prof. Dr. Claudia Draxl
3. Prof. Dr. Paul Erhart

Tag der mündlichen Prüfung: 04.09.2018

Abstract

Metal oxides have become an important component in solar cells, (photo)catalysts, and (opto)electronic devices. Depending on the application conductivity is often either required or should be suppressed for certain types of charge carriers. For both scenarios a detailed theoretical understanding is necessary in order to predict new functional materials. One important factor limiting the conductivity is the interaction of the charge carrier with polar phonon modes. Such a phonon-dressed charge carrier is called polaron. The strength of the electron-phonon (el-ph) interaction determines the localization of the polaron, which in turn defines its characteristic temperature dependence for the charge-carrier mobility and ensuing properties. We focus on materials with strong el-ph coupling, where small polarons are formed, i.e., the localization length is in the order of the unit cell size, and consequently mobility is reduced.

Density-functional theory is often used for calculating properties of polarons. However, there are two challenges that have not been addressed systematically so far: sensitivity of the calculated properties to the errors in exchange-correlation (XC) treatment and finite-size effects in supercell calculations. In this work, we develop an approach that addresses these challenges. The polaron properties are obtained using a modified neutral potential-energy surface (PES). Using the hybrid HSE functional and considering the whole range $0 \leq \alpha \leq 1$ of exact exchange, we show that the modified PES model significantly reduces the dependence of the polaron energy level and binding energy on the XC functional. Based on Pekar's potential for the long-range el-ph coupling, we derive the proper elastic long-range behavior of the polaron and a finite-size correction that allows to obtain the polaron properties in the dilute limit. These findings are proofed by an extensively test for rock salt MgO and rutile TiO_2 using the all-electron, full-potential code package for material science FHI-aims.

Finally, the approach is used to investigate the influence of the crystal structure on the polaron properties for rutile and anatase TiO_2, as well as for the monoclinic β- and orthorhombic κ-phase of Ga_2O_3. While in rutile TiO_2 only small *electron* polarons are stable, only small *hole* polarons are found in anatase. Further, small hole polarons exist in both Ga_2O_3 polymorphs but have significantly different binding energies. Thus, we conclude that growing crystals of the same material but with different structure can be used to manipulate conductivity and charge-carrier mobility.

Zusammenfassung

Wichtige Bestandteile in Solarzellen, (Photo-)Katalysatoren, und (opto-)elektronischen Geräten werden mittlerweile aus Metalloxiden hergestellt. Je nach Anwendungsgebiet kann die Leitfähigkeit im Metalloxid für bestimmte Typen von Ladungsträgern entweder erwünscht oder unerwünscht sein. Für beide Szenarien ist ein genaues theoretisches Verständnis notwendig, um neue funktionelle Materialien vorhersagen zu können. Ein Faktor, der die Leitfähigkeit limitiert, ist die Wechselwirkung der Ladungsträger mit polaren Phononenmoden. Dabei wird das resultierende Quasiteilchen als Polaron bezeichnet. Die Stärke der Elektron-Phonon-Wechselwirkung bestimmt die Stärke der Lokalisierung des Polarons, welche wiederum die Charakteristik der Temperaturabhängigkeit der Ladungsträgermobliltät und darauf aufbauende Eigenschaften definiert. Wir fokussieren uns auf Materialien mit starker Elektron-Phonon-Kopplung, durch die sich kleine Polaronen bilden, d.h. sie lokalisieren in der Größenordnung der Elementarzelle. Infolgedessen wird die Mobilität reduziert.

Die Dichtefunktionaltheorie wird häufig für die Berechnung von Polaroneneigenschaften verwendet. Jedoch gibt es hierbei zwei Schwierigkeiten, welche noch nicht hinreichend systematisch untersucht wurden: Die Sensitivität der berechneten Eigenschaften in Abhängigkeit der Fehler im Austausch-Korrelations (XC)-Funktional und der Effekt der endlichen Größe der für die Simulation verwendeten Superzelle. In dieser Arbeit entwickeln wir eine Methode, die beide Probleme behandelt. Die Polaroneneigenschaften werden auf einer modifizierten neutralen Potentialoberfläche (PES) berechnet. Unter Verwendung des hybriden HSE-Funktional und der Berücksichtigung des gesamten Bereiches $0 \leq \alpha \leq 1$ für den Anteil der exakten Austauschenergie zeigen wir, dass das modifizierte PES-Modell deutlich die Abhängigkeit des Polaronenergielevels und der Polaronbindungsenergie vom XC-Funktional reduziert. Basierend auf dem Potential der Elektron-Phonon-Kopplung von Pekar leiten wir das korrekte elastische langreichweitige Verhalten des Polarons und darauf aufbauend eine Korrektur für die Reduzierung des Einflusses der endlichen Superzellgröße ab. Dies Erkenntnisse wurden durch ausgiebige Tests an Steinsalz MgO und Rutil TiO_2 mit dem FHI-aims Softwarepaket überprüft.

Anschließend wird die oben beschriebene Methode zur Untersuchung des Einflusses der Kristallstruktur auf die Bildung von Polaronen in Rutil und Anatas TiO_2 und in der monoklinischen β- und orthorhombischen κ-Phase von Ga_2O_3 angewendet. Während in Rutil nur kleine Elektronpolaronen stabil sind, finden wir in Anatas nur stabile Lochpolaronen. Hingegen existieren in beiden Phasen von Ga_2O_3 nur stabile Lochpolaronen, jedoch mit deutlich unterschiedlichen Bindungsenergien. Demnach können durch das Züchten von Kristallen desselben Materials mit unterschiedlichen Strukturen Eigenschaften wie Leitfähigkeit und Mobilität der Ladungsträger beeinflusst werden.

Acknowledgements

This thesis is the result of my research during a four years period at the Fritz Haber Institute (FHI) in Berlin and I have to admit that this time as PhD student was one of the best I have had so far. The project about polarons was brought into being by my supervisor Matthias Scheffler, head of the theory department. I am truly grateful to him for giving me this opportunity as well as for many beautiful conferences and all the resources and knowledge available at the FHI. However, the outcome of my work would have been less successful without the help of my group leader Sergey Levchenko. Spending uncountable hours on scientific discussions and correcting my wording and writing he did help so much to clarify my thoughts and to improve my scientific writing. Moreover, I also benefited from the excellent thesis of my predecessor, Norina Richter, underlining the great work you, Sergey, are doing as a group leader. For my first paper written at the FHI and main part of this thesis I am grateful for the help of Patrick Rinke for his suggestions, thoughts, and improvements. Additionally, special thanks to Honghui Shang and Christian Carbogno, whose suggestions and discussions improved my understanding about polarons and electron-phonon coupling at a very early stage of my PhD time. I also would like to thank the people from the Leibnniz ScienceCampus GraFOx giving me the opportunity to interact with experimentalists and to discuss the relevance of polarons in experiments.

Next, I would like to thank the people who shared the office T1.23 with me for this period. In the first place this is Saswata Bhattacharya who helped me to get started with FHI-aims. The last two years I thankfully could share T1.23 with Henrik Kowalski and Maja Lenz making the office to a harmonic place full of many useful discussions, funny stories, mutual help, and inappropriate comments. Of course, there are much more people I would like to thank: Björn Bieniek, Franz Knuth, Markus Schneider, Arvid Ihrig, Aliaksei Mazheika, Christopher Sutton, Florian Knoop, Niklas Menzel, Majid Mortazavi, Carsten Baldauf, and many more for their open ears, fruitful discussions and entertaining after-conference and -work-shop hours. Thanks to all the people, who are keeping the FHI theory department running and who helped me with so many things, especially Hanna, Julia, Steffen, and Birgit.

As life is a succession of events and any subsequent event is the consequence of previous ones this work did benefit – directly or indirectly – from every single moment of my life as well, which is why I am grateful for all the help, support, and inspiration I experienced from my friends and family accompanying me through my life. In the first place these are my parents, Sibylle and Rainer, as well as my grandparents, who did make everything possible for me. This is my brother Lukas, who enriched my life from the very beginning. In addition many thanks to my badminton team and friends for giving me the needed diversion for relaxation.

To Lena, thank you so much for all of your help, motivation, patience, listening, and understanding. You made everything seem a lot easier.

June 2018
Sebastian Kokott

Contents

Introduction

Metal oxides (MOs) have become a promising alternative to classical silicon-based or III-V semiconductors for electronic and optoelectronic devices. They are in many aspects different compared to their predecessors, e.g. in band structure, conductivity, or defect formation. Their success is founded in multiple and even contradicting features realizable in a single material. For example an oxymoron such as transparent conducting oxide implies that despite band gaps larger than 3 eV, at the same time these solids can provide a large number of charge carriers. Many of the desired features are present in crystalline and amorphous phases making them attractive for commercial applications on a large scale production [1]. Moreover, MOs are successful as important components in the design of new devices in other technological fields, too, such as (Photo-)Catalysis [2, 3] or Photovoltaics [4, 5]. Beside new experimental methods for designing and fabrication of oxide bulk materials and thin films, also fundamental theoretical understandings of elemental processes in oxides are needed. This work provides insights into the behavior of excess charge carriers in MOs. The diverse applications of MO require systems, where the conductivity should be either high or suppressed for certain types of charge carriers. The most limiting physical process of conductivity in pristine crystals is the interaction charge carriers with longitudinal-optical (LO) phonon modes.

Traditional band theory only provides an incomplete picture in order to predict the behavior of electrons and holes in polar semiconductors or insulators. In 1933 already Landau [6] pointed out that the polarization of the solid due to the presence of an excess electron enhances its effective mass and, thus, decreases its mobility right up to possible self-trapping of the charge carrier. The phenomenon of self-trapping was later studied in greater detail by Pekar [7], Fröhlich [8], and Holstein [9] and was extended to include the interaction of LO phonon modes with electrons. The quasiparticle of this electron-phonon (el-ph) interaction is called polaron and is further classified by its spatial extent: Large polarons are delocalized over several unit cells, whereas small polarons are typically strongly localized in one or very few unit cells. The proposed semi-empirical Hamiltonian by Fröhlich (only) represents an effective mass approximation of an electron (or hole) placed in a continuum polarizable medium and, thus, is only capable to describe large polarons appropriately, because of its lack of microscopic details. The localization itself depends on the strength of the el-ph coupling, which can be measured with the Fröhlich coupling constant [8]:

$$\alpha_{\mathrm{F}} = e^2 \sqrt{\frac{m_b}{2\hbar^3 \omega_{\mathrm{LO}}}} \left(\frac{1}{\varepsilon_\infty} - \frac{1}{\varepsilon_0} \right) \tag{1}$$

with the band mass[1] m_b, the frequency of the LO mode at the Γ-point, the macroscopic high-frequency dielectric constant ε_∞, and the static dielectric constant ε_0. The region of Fröhlich's large polarons corresponds to $\alpha_\mathrm{F} < 1$. The physics of small polarons ($\alpha >> 1$) was captured by Holstein's model [9] describing their very different motion through a crystal. The α_F provides a rough estimation whether small polarons could potentially form in a material. The needed parameters and the values of α_F for the oxides investigated in this work are summarized in table 1. The detailed discussion on the methods used for the *ab initio* calculations can be found in the chapters 2 and 3, where the materials are investigated in detail. The experimental and *ab initio* values are in good agreement (errors are about 10% and below).

Although Holstein's model was very successful in demonstrating the hopping of small polarons and the ensuing temperature dependence, it only includes short-range interactions of electrons and phonons. However, in ionic materials the formation of small polarons occurs due to the (long-range) polarization of the medium. This means both long- and short-range effects have to be considered. There is no (semi-)empirical model that could capture the physics of small polarons in realistic materials. On the other hand, *first-principles* methods provide a promising solution to the small-polaron problem. Nowadays, density-functional theory (DFT) is widely used to model small polarons. A first-principles model (without need of experimental references) is also desirable for a prediction of small polaron properties in materials that have not been synthesized yet. DFT provides access to approximations that enable solution of the Schrödinger equation with sufficient accuracy. To simulate the host crystal, the supercell approach is most commonly used, where the polaron is embedded in a cell including multiple unit cells. However, there are two challenges that have to be addressed and are the main subject of the methodological part of this thesis: the sensitivity of the calculated properties to the errors in exchange-correlation treatment and finite-size effects in supercell calculations.

The structure of this thesis is as follows. In the first chapter the reader is guided through the different approximations needed for calculating properties of electrons and phonons, as well as their interactions, from *first principles*. First, the Kohn-Sham scheme in DFT and famous approximations of the exchange-correlation functional are introduced. Subsequently, we present main features of the electronic-structure package FHI-aims used throughout this work. Building on this, we explain the frozen-phonon approach for describing properties of phonons in crystals. In the following section, we lay out the general framework for modeling electron-phonon interaction with DFT. Next, we demonstrate that self-trapping cannot be obtained from linear-response perturbation, since anharmonicity plays an important role in this phenomenon. The formation of small polarons requires an explicit evaluation of the potential-energy surface (PES).

The second chapter presents a detailed analysis of the polaron PES dependence on the exchange-correlation functional approximations and the finite-size effects. As a

[1] We denote as band mass the effective mass of a charge carrier derived from the band dispersion of the conduction or valence band (given as $m_b^{-1} = \hbar^{-2}\partial^2\epsilon(k)/\partial k^2|_{k_0}$, where ϵ is the single-particle energy close to a conduction or valence band extremum k_0). This should be distinguished from the effective mass of the polaron m_p introduced later.

	ω_{LO}/THz	ε_∞	ε_0	m_{e}	m_{h}	$\alpha_{\mathrm{F}}^{\mathrm{e}}$	$\alpha_{\mathrm{F}}^{\mathrm{h}}$
rs-MgO	21.41 (21.52[a])	3.08 (2.94[a])	(9.83[a])	0.35	3.65	1.1	4.4
r-TiO_2	25.3 (25.24[b])	7.25 (7.33[b])	(114[b])	2.1-6.7	3.1	2.2–3.8	2.6
a-TiO_2	25.8 (26.36[c])	6.58 (5.67[c])	(37.67[c])	2.5	0.4	1.2	2.6
β-Ga_2O_3	22.5* (24.28[d])	4.11 (3.57[d])	(10[d])	0.41	36	1.1	7.5
κ-Ga_2O_3	22.3*	4.33	(10**)	0.22	57	1.0	12.8

*Value is given without non-analytic correction for the LO/TO splitting.
**Value is taken from the β-Ga_2O_3 phase, since no experimental values found.
[a] Ref. [10]
[b] Ref. [11] and references therein
[c] Ref. [12]
[d] Ref. [13]

TABLE 1: The Fröhlich coupling constants for electrons and holes, $\alpha_{\mathrm{F}}^{\mathrm{e}}$ and $\alpha_{\mathrm{F}}^{\mathrm{h}}$, respectively, for the materials treated in this thesis. The high-frequency dielectric constants ε_∞, the band masses of the electron and hole m_{e} and m_{h}, and the frequency of the highest LO mode ω_{LO} have been calculated from electron and phonon band structures on the basis of Kohn-Sham DFT simulations using the PBE exchange-correlation approximation. The values in parenthesis represent results from experiments. The detailed analysis of the basic material properties such as ε_∞, ε_0, m_b, and ω_{LO} can be found in the chapters 2 and 3. In case of anisotropic materials the tensor of the corresponding property has been averaged, e.g. $\varepsilon_\infty = (\varepsilon_{\infty,xx} + \varepsilon_{\infty,yy} + \varepsilon_{\infty,zz})/3$.

main result, an accurate and at the same time computationally efficient approach for calculating polaron properties is presented. In this work, we focus on calculating the geometry of the self-trapped polaron, its binding energy, and the polaron energy level.

In the last chapter we apply the developed approach to investigate the dependence of the formation of small polarons on the crystal structure. For this, two different polymorphs of TiO_2 and Ga_2O_3 are studied. The results are compared to available experimental values. Finally, we present an outlook on the stability of distinct hole polarons in the phases of Ga_2O_3.

Chapter 1

Ab initio concepts for electrons, phonons, and their interactions

1.1 The crystalline solid

In this thesis, we only treat crystalline solids, where atoms are arranged in a lattice, i.e., amorphous solids and glasses are not discussed in this work. The smallest (and simplest) unit of the crystal is the *unit cell*[1] defined by the lattice vectors $\boldsymbol{a}_1$, $\boldsymbol{a}_2$, and $\boldsymbol{a}_3$. The positions of the atoms $\boldsymbol{\tau}_\kappa$ within one unit cell are called *basis*. With this, any nucleus can be addressed by its position:

$$\boldsymbol{\tau}_{\kappa\boldsymbol{p}} = \boldsymbol{\tau}_{\boldsymbol{p}} + \boldsymbol{\tau}_\kappa, \tag{1.1}$$

where $\boldsymbol{\tau}_{\boldsymbol{p}} = p_1 \cdot \boldsymbol{a}_1 + p_2 \cdot \boldsymbol{a}_2 + p_3 \cdot \boldsymbol{a}_3$ is an arbitrary lattice vector. Moreover, the definition of the lattice in real space allows us to define the reciprocal space represented by the reciprocal lattice vectors $\boldsymbol{b}_1$, $\boldsymbol{b}_2$, and $\boldsymbol{b}_3$, where $\boldsymbol{b}_i \boldsymbol{a}_j = 2\pi\delta_{ij}$. The unit cell in reciprocal space (k-space) is called *Brillouin zone* (BZ). We denote an arbitrary reciprocal lattice vector with $\boldsymbol{G}$. The reciprocal space is occasionally a useful concept for explicitly calculating periodic observables f obeying $f(\boldsymbol{\tau}_{\boldsymbol{p}} + \boldsymbol{\tau}_\kappa) = f(\boldsymbol{\tau}_\kappa)$. Every function $f(\boldsymbol{\tau}_{\boldsymbol{p}})$ can be represented in Fourier space via a Fourier transform $f(\boldsymbol{k}) = \sum_{\boldsymbol{p}} f(\boldsymbol{\tau}_{\boldsymbol{p}}) \mathrm{e}^{i\boldsymbol{k}\boldsymbol{\tau}_{\boldsymbol{p}}}$ with $\boldsymbol{k}$ inside the BZ, which allows for a compact representation of sums (or integrals) in a finite region.

The translational symmetry defined by the lattice vectors, and rotational symmetry given by the basis atoms define the space group of the crystal. There exist 230 different space groups in 3-dimensional space. Every space group generates specific classes of points in the space with a certain symmetry. These points are called Wyckoff positions and the corresponding symbol includes also the multiplicity of the site in the conventional unit cell. This means that often even less parameters are needed than the three lengths of the lattice vectors, the three angles between the vectors, and the positions of all basis atoms. For example, rock salt MgO is fully determined by the specification of

[1]There are two commonly used types of unit cell: the conventional and the primitive unit cell. The primitive unit cell has the smallest possible volume, whereas the conventional unit cell is the smallest with defined lattice vectors according to their crystal system (e.g. cubic, hexagonal, trigonal, etc.)

the space group number 225, the lattice constant $a = 4.21$ Å, and the Wyckoff position of the magnesium atom $4a$=(0,0,0) and the oxygen atom $4b$=(0,0,1/2).

1.2 The many-body problem

To illustrate the complexity of the many-body problem we start with the non-relativistic, time-independent Hamiltonian[2] of a system containing N electrons and N_{nuc} nuclei with charges Z_n and masses M_n:

$$\begin{aligned} H =& T(\boldsymbol{R}) + T(\boldsymbol{r}) + H_{\text{nn}} + H_{\text{en}} + H_{\text{ee}} \\ =& -\frac{\hbar^2}{2}\sum_n^{N_{\text{nuc}}} \frac{1}{M_n}\nabla^2_{\boldsymbol{R}_n} - \frac{\hbar^2}{2}\sum_n^{N}\frac{1}{m}\nabla^2_{\boldsymbol{r}_n} + \frac{1}{2}\sum_{n\neq n'}^{N_{\text{nuc}}} Z_n Z_{n'} v(\boldsymbol{R_n} - \boldsymbol{R_{n'}}) \\ & - \sum_n^{N_{\text{nuc}}}\sum_{n'}^{N} Z_n v(\boldsymbol{R}_n - \boldsymbol{r}_{n'}) + \frac{1}{2}\sum_{n\neq n'}^{N} v(\boldsymbol{r}_n - \boldsymbol{r}_{n'}) \\ =& T(\boldsymbol{R}) + H_{\text{el}}(\boldsymbol{r}, \boldsymbol{R}) \end{aligned} \tag{1.2}$$

with

- the electron coordinates $\boldsymbol{r} = (\boldsymbol{r}_1, \boldsymbol{r}_2, \dots)$,
- the nuclei coordinates $\boldsymbol{R} = (\boldsymbol{R}_1, \boldsymbol{R}_2, \dots)$,
- the nuclei kinetic energy operator $T(\boldsymbol{R}) = -\frac{\hbar^2}{2}\sum_n^{N_{\text{nuc}}} \frac{1}{M_n}\nabla^2_{\boldsymbol{R}_n}$,
- the electron kinetic energy operator $T(\boldsymbol{r}) = -\frac{\hbar^2}{2}\sum_n^{N} \frac{1}{m}\nabla^2_{\boldsymbol{r}_n}$,
- the nucleus-nucleus interaction operator $E_{\text{nn}} = \frac{1}{2}\sum_{n\neq n'}^{N_{\text{nuc}}} Z_n Z_{n'} v(\boldsymbol{R_n} - \boldsymbol{R_{n'}})$,
- the electron-nucleus interaction operator $E_{\text{en}} = \sum_n^{N_{\text{nuc}}}\sum_{n'}^{N} Z_n v(\boldsymbol{R}_n - \boldsymbol{r}_{n'})$,
- the electron-electron interaction operator $H_{\text{ee}} = \frac{1}{2}\sum_{n\neq n'}^{N} v(\boldsymbol{r}_n - \boldsymbol{r}_{n'})$,

and the Coulomb interaction:

$$v\left(\boldsymbol{x}\right) = \frac{e^2}{4\pi\epsilon_0|\boldsymbol{x}|} \tag{1.3}$$

The Hamiltonian of the electron problem is denoted by

$$H_{\text{el}}(\boldsymbol{r}, \boldsymbol{R}) = H - T(\boldsymbol{R}). \tag{1.4}$$

[2]Here, we do not explicitly restrict the Hamiltonian to periodic systems to avoid an overloaded index notation. However, this can be simply adapted e.g. by changing the coordinates of the ions $\boldsymbol{R}_n \to \tau_{\kappa\boldsymbol{p}}$ with the notation introduced in Eq. (1.1).

The states of this system and their corresponding energies are solutions of the eigenvalue problem:

$$H\Psi\left(\boldsymbol{r},\boldsymbol{R}\right)=E\Psi\left(\boldsymbol{r},\boldsymbol{R}\right) \tag{1.5}$$

(Numerically) exact solutions of Eq. (1.5) exist only for a few number of systems (hydrogen atom, helium ion He^{+}, or the ionized hydrogen molecule H_2^{+} [14]). For solids no exact solution exists, and even a numerical solution is impossible to obtain for realistic systems with today's computational power.

1.3 Adiabatic approximations

A first step towards an approximate solution of Eq. (1.5) is the separation of the electronic and nuclear degrees of freedom. Let $\Phi_k(\boldsymbol{r};\boldsymbol{R})$ be the K orthonormal eigenfunctions of

$$H_{\mathrm{el}}\Phi_k(\boldsymbol{r};\boldsymbol{R})=E_k(\boldsymbol{R})\Phi_k(\boldsymbol{r};\boldsymbol{R}) \tag{1.6}$$

for each fixed $\boldsymbol{R}$. This allows the following parametrization of the wave function of the Hamiltonian Eq. (1.5):

$$\Psi\left(\boldsymbol{r},\boldsymbol{R}\right)=\sum_{k}^{K}X_k(\boldsymbol{R})\Phi_k(\boldsymbol{r};\boldsymbol{R}) \tag{1.7}$$

The semicolon separating the $\boldsymbol{R}$ coordinates indicates that they are only treated as parameters. Substituting into Eq. (1.5), multiplying by $\Phi_{k'}$, and integrating over electronic coordinates yields:

$$\sum_{k}^{K}\left[E_k(\boldsymbol{R})\delta_{kk'}+T(\boldsymbol{R})\delta_{kk'}+\Gamma_{kk'}(\boldsymbol{R})\right]X_k(\boldsymbol{R})=EX_{k'}(\boldsymbol{R}) \tag{1.8}$$

$$\begin{aligned}\Gamma_{kk'}(\boldsymbol{R})=-\sum_{i}^{N_{\mathrm{nuc}}}\frac{\hbar^2}{M_i}\Bigg[&\int \mathrm{d}\boldsymbol{r}\Phi_k^*(\boldsymbol{r};\boldsymbol{R})\frac{\partial}{\partial\boldsymbol{R}_i}\Phi_{k'}(\boldsymbol{r};\boldsymbol{R})\frac{\partial}{\partial\boldsymbol{R}_i}\\&+\frac{1}{2}\int \mathrm{d}\boldsymbol{r}\Phi_k^*(\boldsymbol{r};\boldsymbol{R})\frac{\partial^2}{\partial\boldsymbol{R}_i^2}\Phi_{k'}(\boldsymbol{r};\boldsymbol{R})\Bigg]\end{aligned} \tag{1.9}$$

The first term inside the sum in Eq. (1.9) vanishes for continuous and differentiable parameterizations (this can be seen from integration by parts). Note that Eq. (1.8) is still exact. The non-diagonal matrix elements $\Gamma_{kk'}$ describe the transition between different electronic states of the system due to the motion of the nuclei and are commonly referred to as *non-adiabatic* or *vibronic interactions*. However, these elements are usually small and can be neglected, if the difference between electronic energies is sufficiently large (see Eq. (1.11) for a sufficient condition). Equation (1.8) with he remaining diagonal elements $k = k'$ included is called the *Born-Huang* approximation [15]. In this approximation, every electronic state of the system can be treated separately. The wave functions for the kth potential energy surface (PES) are then given by:

$$\Psi_k\left(\boldsymbol{r}, \boldsymbol{R}\right) = X_k(\boldsymbol{R})\Phi_k(\boldsymbol{r}; \boldsymbol{R}) \tag{1.10}$$

The approximation of Eq. (1.7) as Eq. (1.10) is reasonable, if the following condition holds:

$$(m/M_i)^{1/4} \ll 1 \tag{1.11}$$

Even the diagonal elements of $\Gamma_{kk'}$ are small compared to the kinetic energy of the nuclei and are commonly neglected in the adiabatic approximation, too. If we do so, we get the Born-Oppenheimer approximation:

$$\left[E_k(\boldsymbol{R}) + T(\boldsymbol{R})\right] X_k(\boldsymbol{R}) = E_k^{\mathrm{BO}} X_k(\boldsymbol{R}). \tag{1.12}$$

Interestingly, the energy of the ground state in the Born-Oppenheimer approximation E_0^{BO} is always a lower bound of Eq. (1.5) [16], and the energy of the Born-Huang approximation E_0^{BH} is an upper bound [15]:

$$E_0^{\mathrm{BO}} \leq E_{0,\mathrm{solid}} \leq E_0^{\mathrm{BH}} \tag{1.13}$$

The BO approximation decouples the dynamics of the electrons and the nuclei and allows to calculate the electronic ground-state energy of a solid separately. The energy of the electrons can then be corrected for the motion of the nuclei. From now on we only work within the BO approximation throughout this study and drop the index "BO" for simplicity.

According to the theorem of Hellmann and Feynman the interatomic-forces can be evaluated parametrically on the BO PES of the ground state ($k = 0$) as follows:

$$\boldsymbol{F}_\kappa = \left\langle \Phi_0(\boldsymbol{r}; \boldsymbol{R}) | \boldsymbol{\nabla}_{\boldsymbol{R}_\kappa} H_{\mathrm{el}} | \Phi_0(\boldsymbol{r}; \boldsymbol{R}) \right\rangle, \tag{1.14}$$

where $\boldsymbol{F}_\kappa$ denotes the force of the κth nuclei. Equation. (1.14) is important for describing the classical motion of the nuclei. Note that additional force contributions (e.g. Pulay forces in case of atom-centered orbitals) can appear depending on the choice of the electronic basis functions.

1.4 Density-functional theory

In the previous section we have separated the dynamics of the electrons and the nuclei by means of the BO approximation. The Coulomb potential of the nucleus-nucleus interaction now only appears as external potential v_{ext} in the Hamiltonian of the electrons, Eq. (1.4), which means all coordinates of the nuclei are treated as parameters. This is a great simplification, but solving the Schrödinger equation for the electrons still remains impossible for many-electron systems. One way to tackle the problem is by using wave-function-based methods. The first step in this framework is usually the Hartree-Fock (HF) approximation, where single-electron wave functions (orbitals) are varied in order to find the minimum energy for a single Slater determinant (cf. App. A). The HF energy is variational and includes the correct exchange energy. The remaining difference between the HF and exact energy is called correlation energy (to emphasise the mean-field nature of HF approximation). In order to add correlation, post-HF methods such as Møller-Plesset perturbation theory [17], the coupled-cluster approach [18], or the configuration interaction [19] are used. The price for the higher accuracy in energy and wave functions is an increase in computational cost.

A groundbreaking new approach emerged based on the theory of Hohenberg and Kohn in 1964 [20], where the ground state of the system is obtained by minimizing an energy functional with respect to the electron density as the fundamental variable. However, the breakthrough in terms of balancing accuracy and numerical effort was made when the scheme proposed by Kohn and Sham [21] appeared just one year later, which enabled the self-consistent calculation of single-electron orbitals similar to the HF approach. The next section introduces the main ideas and approximations of this theory, as well as the numerical realization within the software package FHI-aims.

1.4.1 Fundamentals

Before trying to cast the many-electron Schrödinger equation into a density-functional form, we have to ensure that the mapping between the external potential, the wave function, and the density is unique. We will start with some trivial maps first. With $v_{\text{ext}} \in V$ we collect all local potentials[3] leading to a non-degenerate ground state. The external potential v_{ext} defines the form of the Hamiltonian $\hat{H}$:

$$\hat{H}\left|\Psi\right\rangle = \left(\hat{T} + \hat{W} + \hat{v}_{\text{ext}}\right)\left|\Psi\right\rangle = E\left|\Psi\right\rangle, \tag{1.15}$$

where $\hat{W}$ is the operator of the electron-electron interaction. By solving the eigenvalue problem we obtain a set of eigenfunctions $\{\Psi_i\}$, where the solutions are numbered with ascending energy with $i = 0$ denoting the ground state. With this the solution of $\hat{H}$ defines a surjective map $C : v_{\text{ext}} \to \Psi_0$. Further, defining the ground-state electron

[3] In the context of the Hamiltonian of the solid Eq. (1.5) in the BO approximation $v_{\text{ext}} = -\sum_n^{N_{\text{nuc}}}\sum_{n'}^{N} Z_n v(\boldsymbol{R}_n - \boldsymbol{r}_{n'}) + \frac{1}{2}\sum_{n\neq n'}^{N} v(\boldsymbol{R}_n - \boldsymbol{R}_{n'})$ is the potential of the electron-nuclei and nuclei-nuclei interaction and, with this, a one particle operator of the electrons.

density as:

$$n_0(\boldsymbol{r}) = \langle \Psi_0 | \sum_{i=1}^{N} \delta\left(\boldsymbol{r} - \boldsymbol{r_i}\right) | \Psi_0 \rangle \tag{1.16}$$

we get a second surjective map $D : \Psi_0 \to n_0$. The question to be answered is whether any ground-state density can be uniquely mapped onto the external potential, which leads to the formulation of the following theorem first proposed by Hohenberg and Kohn in 1964 [20]:

Theorem 1 (Hohenberg-Kohn I) *The map $C \circ D : v_{ext} \to n_0$ is bijective, apart from a trivial additive constant for v_{ext}.*

We follow the proof given by Dreizler and Gross [22]. First, for the map C we have to show that external potentials differing by more than a constant, $v_{\text{ext}} \neq v'_{\text{ext}} + const$, always lead to different ground states. We start with the two Hamiltonians:

$$\left(\hat{T} + \hat{W} + \hat{v}_{\text{ext}}\right) |\Psi_0\rangle \quad = E_0 \, |\Psi_0\rangle \tag{1.17}$$

$$\left(\hat{T} + \hat{W} + \hat{v}'_{\text{ext}}\right) |\Psi'_0\rangle \quad = E'_0 \, |\Psi'_0\rangle \tag{1.18}$$

The assumption $\Psi_0 = \Psi'_0$ will give a contradiction. Subtracting Eq. (1.18) from (1.17) results in:

$$\left(\hat{v}_{\text{ext}} - \hat{v}'_{\text{ext}}\right) |\Psi_0\rangle = \left(E_0 - E'_0\right) |\Psi_0\rangle \,, \tag{1.19}$$

and, since v_{ext} is multiplicative, we find for the potential differences $\hat{v}_{\text{ext}} - \hat{v}'_{\text{ext}} = E_0 - E'_0$, which is obviously only a constant. This means, two different external potentials will always lead to two different ground states.

Second, to ensure that D is bijective we need to show that from $\Psi_0 \neq \Psi'_0$ follows $n_0 \neq n'_0$. For the two wave functions $\Psi_0 \neq \Psi'_0$ we get the ground-state energies $E_0 = \langle \Psi_0 | \hat{H} | \Psi_0 \rangle$ and $E'_0 = \langle \Psi'_0 | \hat{H}' | \Psi'_0 \rangle$, respectively. Since the ground state Ψ minimizes the expectation value of the corresponding Hamiltonian $\hat{H}$, we get by means of the Ritz principle:

$$\begin{aligned} E_0 < \langle \Psi'_0 | \hat{H} | \Psi'_0 \rangle = & \quad E'_0 - \langle \Psi'_0 | (\hat{v}'_{\text{ext}} - \hat{v}_{\text{ext}}) | \Psi'_0 \rangle \\ = & \quad E'_0 - \int \mathrm{d}\boldsymbol{r}\, n'_0(\boldsymbol{r}) \left[v'_{\text{ext}}(\boldsymbol{r}) - v_{\text{ext}}(\boldsymbol{r})\right] \end{aligned} \tag{1.20}$$

and equally for the primed system:

$$E'_0 < \langle \Psi_0 | \hat{H}' | \Psi_0 \rangle = E_0 - \int \mathrm{d}\boldsymbol{r}\, n_0(\boldsymbol{r}) \left[v_{\text{ext}}(\boldsymbol{r}) - v'_{\text{ext}}(\boldsymbol{r})\right] . \tag{1.21}$$

Adding Eq. (1.17) to Eq. (1.18) and assuming $n_0 = n'_0$ we find the inconsistency:

$$E_0 + E'_0 < E_0 + E'_0.$$

This proves that a map $D^{-1} : n_0 \to |\Psi_0\left[n_0\right]\rangle$ exists, i.e., the wave function can be written as a functional of the ground-state density. Consequently, the expectation value of the Hamiltonian $\hat{H}$ is a unique functional of the ground-state density, too:

$$\begin{aligned} E_{v_{\text{ext}}}[n_0] &= \langle \Psi_0[n_0] | \hat{T} + \hat{W} + \hat{v}_{\text{ext}} | \Psi_0[n_0] \rangle . \\ &= F_{\text{HK}}[n_0] + \int \mathrm{d}\boldsymbol{r}\, n_0(\boldsymbol{r}) v_{\text{ext}}(\boldsymbol{r}), \end{aligned} \tag{1.22}$$

where we defined the Hohenberg-Kohn functional

$$F_{\text{HK}} = \langle \Psi_0[n_0] | \hat{T} + \hat{W} | \Psi_0[n_0] \rangle . \tag{1.23}$$

In the second theorem, Hohenberg and Kohn [20] established the variational character of the functional $E_{v_{\text{ext}}}[n_0]$

Theorem 2 (Hohenberg-Kohn II) *The total-energy functional $E_{v_{ext}}[n]$ is minimized by the ground-state density $n = n_0$ corresponding to v_{ext}.*

To prove this statement we can use arguments similar to the above ones. From the Rayleigh-Ritz principle we get for the external potential v_{ext}:

$$E_0 \leq E_{v_{\text{ext}}}[n] \tag{1.24}$$

From the map $C \circ D$ it obviously follows that equality in Eq. (1.24) only holds for $n = n_0 = C \circ D(v_{\text{ext}})$, i.e., $E_0 = E_{v_{\text{ext}}}[n_0]$. As a consequence the exact ground-state density can be obtained by minimizing the total-energy functional:

$$E_0 = \min_n E_{v_{\text{ext}}}[n] \tag{1.25}$$

with $\int \mathrm{d}\boldsymbol{r}\, n(\boldsymbol{r}) = N$. Interestingly, the functional F_{HK} is independent on the external potential v_{ext}, because the map D^{-1} is defined independently from v_{ext}. This means that the form of F_{HK} is universal and is the same for all different atoms, molecules and solids. Moreover, the HK theorem did not only lay the foundation for DFT. It additionally shows that the three basic variables, i.e., v_{ext}, Ψ_0, and n_0 are equivalent descriptors of the electronic Hamiltonian. Thus, the solution of Eq. (1.15) can be obtained in three different ways: wave-function-based methods (e.g., full configuration interaction), DFT (e.g., orbital-free DFT [23]), and potential-functional theory [24]. However, one of the most successful frameworks is introduced in the next section and the first expression for a practical re-writing of the expectation value Eq. (1.22) in terms of the electron density is given.

1.4.2 The Kohn-Sham scheme

The first practical scheme for DFT was provided by Kohn and Sham [21] only one year later. The authors suggested to use an effective single-particle scheme instead of solving the complex many-particle problem. The main ideas are summarized in the following:

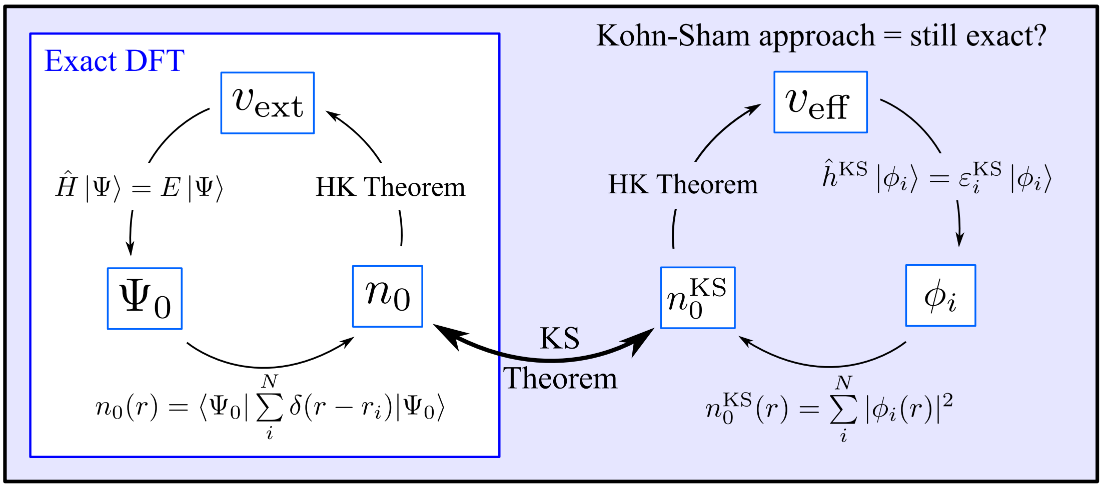

FIGURE 1.1: Illustration of the two important theorems in DFT. The white box presents the importance of the Hohenberg-Kohn I theorem. It ensures the equivalence between the three basic variables of the many-electron problem, namely the external potential v_{ext}, the ground-state wave function Ψ_0 and the ground-state density n_0. The blue box shows the approach suggested by Kohn and Sham (KS) mapping the many-electron on an effective single-electron problem.

Theorem 3 (Kohn-Sham) *The exact ground-state density n_0 can be identified with a ground-state n_0^{KS} of an auxiliary system with non-interacting particles. The single-electron Hamiltonian of the auxiliary system $\hat{h}_{KS}$ is chosen to have the usual kinetic operator and an effective potential v_{eff} acting on an electron at point $\boldsymbol{r}$.*

Let us evaluate the content of these statements and their consequences. Let the ground-state density of the interacting system be n_0 corresponding to the external potential v_{ext}. Then, Kohn and Sham postulate:

$$n_0(\boldsymbol{r}) = n_{\text{KS}}(\boldsymbol{r}) = \sum_{i=1}^{N} |\phi_i(\boldsymbol{r})|^2 \tag{1.26}$$

where the single-electron wave functions are solutions of the equations:

$$\hat{h}_{\text{KS}}\,|\phi_i\rangle = \left(-\frac{\hbar^2}{2m}\nabla^2 + v_{\text{eff}}\right)|\phi\rangle = \epsilon_i\,|\phi_i\rangle\,, \tag{1.27}$$

and where we call:

$$T_{\text{s}}\,[n] = -\frac{\hbar^2}{2m}\sum_i \int \mathrm{d}\boldsymbol{r}\;\phi_i^*(\boldsymbol{r})\nabla^2\phi_i(\boldsymbol{r}) \tag{1.28}$$

the kinetic energy of the non-interacting system. We still have to answer the question how v_{eff} is connected to v_0. Let us re-write the total energy for the interacting system in the following way:

$$E_{v_{\text{ext}}}[n] = T_{\text{s}}[n] + \int \mathrm{d}\boldsymbol{r}\, n(\boldsymbol{r}) v_{\text{ext}}(\boldsymbol{r}) + \int \mathrm{d}\boldsymbol{r}\, n(\boldsymbol{r}) v_{\text{H}}(\boldsymbol{r}) + E_{\text{xc}}[n] \tag{1.29}$$

with the Hartree potential:

$$v_{\text{H}} = \int \mathrm{d}\boldsymbol{r}' \frac{n(\boldsymbol{r})}{|\boldsymbol{r} - \boldsymbol{r}'|} \tag{1.30}$$

and the exchange-correlation (xc) energy:

$$E_{\text{xc}}[n] = F_{\text{HK}}[n] - T_{\text{s}}[n] - \int \mathrm{d}\boldsymbol{r}\, n(\boldsymbol{r}) v_{\text{H}}(\boldsymbol{r}) \tag{1.31}$$

By variation of the total-energy functional $\delta E_{v_{\text{ext}}}[n] = 0$ one finds for the effective potential v_{eff}:

$$v_{\text{eff}} = v_{\text{ext}} + v_{\text{H}} + v_{\text{xc}}, \tag{1.32}$$

with $v_{\text{xc}} = \frac{\delta E_{\text{xc}}[n]}{\delta n}$. Eqs. (1.26), (1.27), and (1.32) form the Kohn-Sham scheme. Since these equations are interlinked, they have to be solved self-consistently in a similar manner as for the HF approximation. However, we have not shown yet, whether the density n_0 of the interacting system can be always represented by a non-interacting potential v_{eff}. Once this is ensured, uniqueness of v_{eff} is guaranteed by Theorem 1.17, again. Besides simple model systems, this has not be proven in general and remains a pure assumption. This is the mathematical Achilles heel of the Kohn-Sham scheme. Nevertheless, the success of the DFT in the framework of the KS scheme demonstrates at least that it is a reasonable approximation. After solving the Kohn-Sham equations self-consistently, the ground-state total energy is calculated as:

$$\begin{aligned} E_{v_{\text{ext}}}[n_0] = \quad & \sum_{i=1}^{N} \epsilon_i - \frac{1}{2} \int \mathrm{d}\boldsymbol{r}\, n_0(\boldsymbol{r}) v_{\text{H}}(\boldsymbol{r}) \\ & + E_{\text{xc}}[n_0] - \int \mathrm{d}\boldsymbol{r}\, n_0(\boldsymbol{r}) v_{\text{xc}}([n_0], \boldsymbol{r}). \end{aligned} \tag{1.33}$$

1.4.3 The physical meaning of the KS orbitals

Hitherto, we have mapped the many-electron problem onto an effective single-particle problem, described by the KS equations eq. (1.27). Although we have shown that the ground-state densities of both problems should be identical, the single-particle KS orbitals and their corresponding eigenvalues lack any physical meaning, since they only represent an auxiliary system. Therefor, effort has been made to get more physical information from the KS orbitals. Janak did a first important step in proving the relation [25]:

$$\left.\frac{\partial E(N)}{\partial n_i}\right|_{\delta+} = \epsilon_i(N) \tag{1.34}$$

with the total energy E, where the N in parenthesis denotes the ground state with N electrons occupying the N lowest states, and the ith KS eigenvalue ϵ_i and occupation number n_i. The derivative is taken from the right (indicated by δ^+). Perdew and co-workers [26] proved for systems with fractional electron number that the chemical potential μ of the electrons is related to the IP and EA as follows:

$$\mu = \frac{\partial E}{\partial n_i} = \begin{cases} -\text{IP, for } N-1 < n_i < N \\ -\text{EA, for } N < n_i < N+1 \end{cases} , \tag{1.35}$$

with the ionization potential IP$= E(N-1) - E(N)$ and the electron affinity EA$=E(N) - E(N+1)$. By comparing Eq. (1.35) with (1.34) we find directly the IP theorem:

$$\epsilon_{ho}(N) = -\text{IP}. \tag{1.36}$$

However, the similar expression for the EA is more difficult to evaluate. There is a constant shift Δv_{XC} of the XC potential leading to:

$$\epsilon_{N+1}(N+1) = \epsilon_{N+1}(N) + \Delta v_{\text{XC}} \tag{1.37}$$

from which follows:

$$\epsilon_{lu}(N) + \Delta v_{\text{XC}} = -\text{EA}, \tag{1.38}$$

with the lowest unoccupied state $\epsilon_{lu}(N) = \epsilon_{N+1}(N)$. Δv_{XC} is known as the XC derivative discontinuity [27, 28]. From this follows for the fundamental gap:

$$E_{\text{gap}}^{\text{fund}} = \text{IP} - \text{EA} = E_{\text{gap}}^{\text{KS}} + \Delta v_{\text{XC}}, \tag{1.39}$$

which means that the KS gap $E_{\text{gap}}^{\text{KS}} = \epsilon_{N_0+1}(N_0) - \epsilon_{N_0}(N_0)$ (for the exact , but unknown XC functional) underestimates the actual fundamental gap by Δv_{XC}. Nonetheless, Eq. (1.36) has the following remarkable implications:

- The total energy is linear in between two integer occupation numbers
- The position of the highest-occupied state is independent on its occupation
- The total density far away from its localization (i.e., $r \to \infty$) decays as $n_0(r) \sim \mathrm{e}^{-2r\sqrt{\epsilon_{\text{ho}} 2m/\hbar^2}}$ [29]

This underlines that it is important to have a consistent description of the total density, total energies, and the ho states.

For any known XC approximation Eq. (1.36) is not satisfied in general in case of localized ho orbitals. Formally, the exact XC functional would cancel the spurious self-interaction in the Hartree term, e.g., as it is the case for the exact exchange introduced later. Yet, there are only a few local approximations that ensure the cancellation for many-electron systems, e.g. the SIC approach [30]. In general for functionals, where the total energy is not piecewise-linear in between integer occupation numbers, we denote the deviation from the straight line as Δ_{XC} leading to the following general

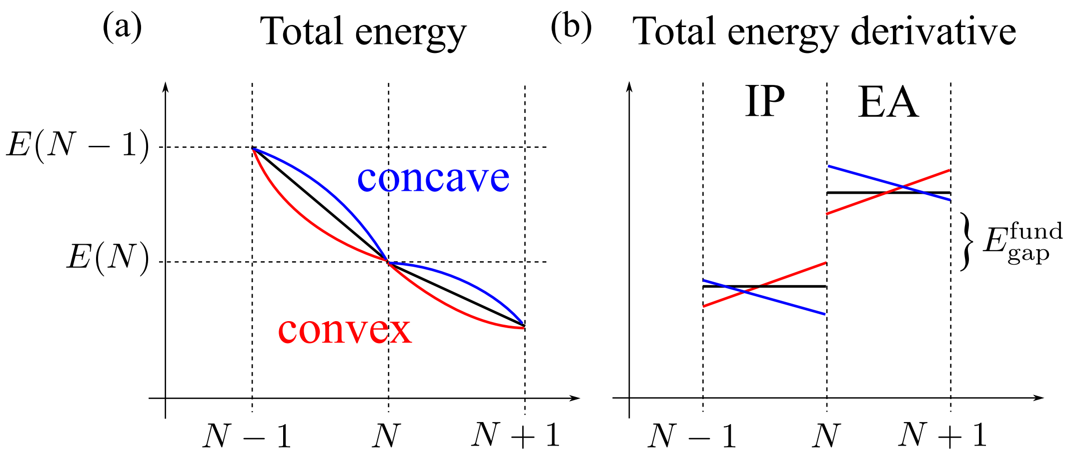

FIGURE 1.2: (a) The deviation of the straight-line behavior (black) for convex (red) and concave (blue) XC-functionals. At integer electron number the total energies $E(N)$ have been aligned to the same value. (b) The total energy derivatives corresponding to the IP for $N-1 < n_i < N$ and the EA for $N < n_i < N+1$. Clearly, the fundamental gap $E_{\text{gap}}^{\text{fund}}$ = IP − EA is underestimated for convex and overestimated for concave functionals.

expression for XC approximations:

$$E(N-1) - E(N) = \epsilon_{\text{ho}}(N) + \Delta_{\text{XC}}. \tag{1.40}$$

Figure 1.2 illustrates this issue. The self-interaction error (SIE) causes a convex curvature with $\Delta_{\text{XC}} > 0$, whereas e.g. for the HF method a concave curvature can be observed with $\Delta_{\text{XC}} < 0$. The main problem of the HF method is the missing electron correlation, which leads to an over-localization of the states in the ionized system, the so-called orbital-relaxation error. There is another weak point which have all known XC approximations in common, that is, they do not show a discontinuity in the XC potential Δv_{XC} at integer electron numbers. A promising concept for "restoring" the derivative discontinuity even for (semi-)local functionals was suggested by Kraisler and Kronik [31], where the system is treated as an ensemble of ionized and neutral system. Unfortunately, this leads to orbital-dependent expressions and, hence, computationally expensive evaluations.

Moreover, the statements Eq. (1.36) and (1.38) have been derived for atoms and molecules, i.e. systems with finite extension, and transferring them to solids has to be done carefully. Guided by the arguments of Williams and von Barth [32], one can observe that for an infinitely large solid (or in general any delocalized wave function) the fundamental and the KS gap become identical:

$$E_{\text{gap}}^{\text{fund}} = E_{\text{gap}}^{\text{KS}} \tag{1.41}$$

The arguments of Williams and von Barth has been extended to the concept of the generalized KS theory [33], which applies for hybrid functionals and exact exchange.

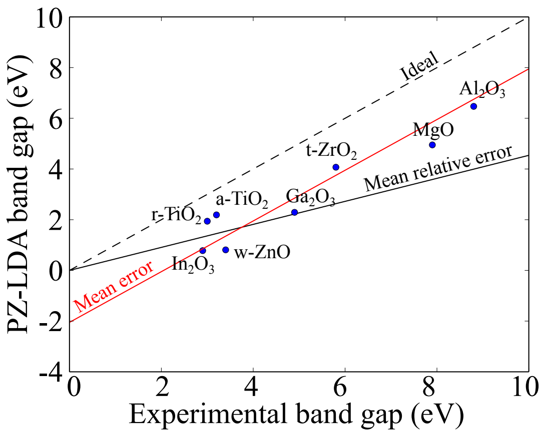

FIGURE 1.3: The PZ-LDA band gap versus the experimental band gap is shown for eight different closed-shell oxides. The lowercase letters in front of the chemical symbols indicate the specific phase (t – tetragonal, r – rutile, a – anatase, w – wurzite). All structures are fully relaxed, i.e., all atom positions and all lattice constants and angles are relaxed.The black dashed line corresponds to the ideal agreement between theory and experiment. The black solid line represents the expectation value of the LDA gap based on the mean relative error, and the red line corresponds to the shift of the experimental values by the mean error (see text for details).

However, Eq. (1.41) does not mean that the band gaps obtained with certain XC approximations are generally in good agreement with experimental measurements, it rather depends on the quality of the approximations that were made. Some of the most famous XC approximations are introduced in the following section.

1.4.4 The exchange-correlation functional

Assuming that the Kohn-Sham theorem is correct (or at least a very good approximation) we now have to face the fact that all difficulties are just shifted into the XC functional. At this point we are going to leave the ground of "exact" *density-functional theory* and start to explore the area of *density-functional approximations* (DFA).

Local-density approximations

Kohn and Sham proposed in 1965 an approximation for the exchange and correlation energy for slowly varying densities. Nowadays approximations of this type are called local density approximation (LDA). The main idea is that for every point $\boldsymbol{r}$ the electron density behaves locally as a homogeneous electron gas (HEG, for detailed expressions c.f. App. A). Consequently, the XC functional becomes only a *function* of the density:

$$E_{\mathrm{xc}}[n] \to E_{\mathrm{xc}}(n(\boldsymbol{r})) = \int \mathrm{d}\boldsymbol{r}\, n(\boldsymbol{r})[e_{\mathrm{x}}(n(\boldsymbol{r})) + e_{\mathrm{c}}(n(\boldsymbol{r}))]. \tag{1.42}$$

The explicit expressions for e_x and e_c are given in the Appendix by Eqs. (A.15) and (A.19), respectively. By the virtue of the approximation the LDA is expected to work well for metals, where the valence-electron density is slowly varying. However, it also works unexpectedly well for atoms, molecules, and solids with an energy gap. Here, we will focus on the investigation of the performance of the LDA functional for several closed-shell oxides shown in Fig. 1.3. The band gaps are obtained from self-consistent calculations using FHI-aims, where all degrees of freedom (atom positions and lattice vectors) have been relaxed. In general, it can be observed that all oxides are predicted to be insulators, but the band gap is clearly underestimated. We find a mean relative error (MRE[4]) of about -48% with respect to the experimentally measured band gaps. If the error in the LDA gap versus experiment depended on the size of the gap, the LDA gaps would be on the gray line in Fig. 1.3. This line corresponds to the expectation value of the LDA band gap $E_{\text{gap,LDA}}$ based on MRE, $\langle E^i_{\text{gap,LDA}}\rangle_{\text{MRE}} = E^i_{\text{gap,exp}}{\cdot}\text{MRE}$. Clearly, this is not the case. Instead, it can be observed that for our small test set of oxides the band gaps are shifted systematically by a constant, where the shift is represented by the mean error (ME). The red line in Fig. 1.3 is obtained by shifting the experimental gaps by ME, $\langle E^i_{\text{gap,LDA}}\rangle_{\text{ME}} = E^i_{\text{gap,exp}}{+}\text{ME}$. We find ME $= -2.0$ eV. Similar systematic trends for the deviation of the LDA band gap from the experimental band gap have been found also for larger test sets [34]. In conclusion, despite the crude approximations the LDA turns out to be a successful starting point for the description of solids. Note that LDA functionals do not always correctly predict a material to be a metal or an insulator. Especially for open-shell systems, LDA is often failing, e.g. CoO is predicted to be metallic, but is measured to have a band gap of about 2.5 eV. Another prominent example for the failure of LDAs is the diamond Ge crystal, which is actually a semiconductor with a band gap of 0.74 eV, whereas LDA predicts Ge to be metallic.

Generalized gradient approximations

To improve the LDA, a first idea was simply to include the gradient of the density $|\nabla n|$ as the next order in the sense of a tailor expansion. Unfortunately, these gradient expansion approximations did not improve the LDA results systematically. The main issue of this ansatz were the large gradients for realistic materials. Hence, a more general approach was used to include gradients of the density. The so-called generalized gradient approximations (GGA) have the following form for the XC energy:

$$E_{\text{xc}}[n] = \int \mathrm{d}\boldsymbol{r}\, n(\boldsymbol{r}) e_{\text{x}}^{\text{HEG}}(n) F_{\text{xc}}(n, |\nabla n|, \dots), \tag{1.43}$$

where F_{xc} is the XC-enhancement factor and $e_{\text{x}}^{\text{HEG}}$ the exchange energy density (Eq. (A.15)) of the HEG. This much more flexible form of E_{xc} allows for the implementation of exact limits from DFT. Throughout this work we are using the GGA proposed

[4]MRE$=1/N \sum_i^N (E^i_{\text{gap,DFT}} - E^i_{\text{gap,exp}})/E^i_{\text{gap,exp}}$, where $E^i_{\text{gap,exp}}$ is the experimentally measured and $E^i_{\text{gap,DFT}}$ the calculated band gap.

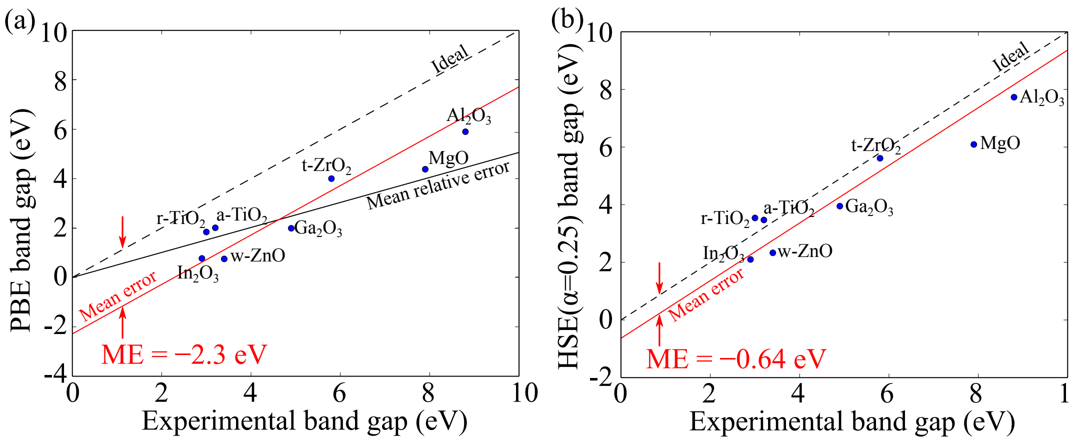

FIGURE 1.4: The (a) PBE and (b) HSE($\alpha = 0.25$) band gap versus the experimental band gap is shown for eight different closed-shell oxides. The lowercase letters in front of the chemical symbols indicate the specific phase (t – tetragonal, r – rutile, a – anatase, w – wurzite). All structures are fully relaxed for the PBE results, i.e., all atom positions and all lattice constants and angles are relaxed. For the HSE results the PBE geometries were used. The solid red and black line are calculated equally as for Fig. 1.3.

by Perdew, Burke, and Ernzerhof in 1996. For the explicit parametrization of the enhancement factors F_{xc} we refer to the original work Ref. [35]. It is important to note that the performance of the PBE functional in terms of computational time is similar to LDA, even though it is a semi-local functional (i.e., not only the density n at point $\boldsymbol{r}$ is regarded, but additionally points in the infinitesimal vicinity). The test for the closed-shell oxides has been repeated for the PBE functional, and the results are shown in Fig. 1.4(a). Surprisingly, the inclusion of the density gradients has not improved the results; in case of our test set they even got worse, as indicated by ME $= -2.3$ eV. However, PBE did improve the atomization energies for a large test set of molecules, and did perform similar to LDA for ionization potentials and electron affinities [36, 37, 38].

The comparison of PBE and LDA band gaps with experiment raises the question: What is still missing in order to describe the electronic structure of insulating solids properly? Or, more generally: Is an accurate prediction of the band gap possible with (semi-)local XC functionals?

Hybrid density functionals

Already Kohn and Sham suggested [21] to use the non-local Fock operator for the exchange functional instead of the exchange term from the HEG, i.e. the effective potential v_{eff} in Eq. 1.27 is not local anymore. However, the first practical solutions to combine (semi-)local XC functionals with exact exchange (EXX) were proposed and numerically tested by Becke [39] (mixing with LDA) and later by Perdew *et al.* [40]

(mixing with PBE). They all share the following kind of mixing:

$$E_{\mathrm{XC}} = \alpha\left(E_{\mathrm{EXX}} - E_{l\mathrm{X}}\right) + E_{\mathrm{lXC}} \tag{1.44}$$

with the mixing parameter α, the EXX energy E_{EXX}, and the exchange (X) and XC energy of the (semi-)local approximation such as LDA or GGA E_{lX} and E_{lXC}, respectively. A question immediately arises: What is the proper value of α? Based on a perturbative expansion of the adiabatic connection formula (cf. [41, 42, 43]) for the XC energy, Becke suggested $\alpha = 0.5$ in order to improve the IPs and EAs of molecules and atoms. For larger molecules and for solids the fraction of $\alpha = 0.25$ turned out to be most successful for improving the IPs and EAs in the simple form of Eq. (1.44), which was proposed by Perdew *et al.* [40] using the same argument as Becke. However, Perdew *et al.* also pointed out that the proper portion of α depends on the system. For example, the inclusion of EXX for metallic system is not expected to improve their description, e.g. the positions of the electron bands, so $\alpha = 0$ is the best choice. For semiconductors and large-band-gap systems, $\alpha = 0.25$ and 0.5 are giving best results for the prediction of band gaps, respectively. Finally, for extreme cases such as Kr^{26+}, $\alpha = 1$ fits best for ionization energies. This analysis shows that the most commonly used fraction $\alpha = 0.25$ is just the one minimizing the MRE for certain properties such as the band gap of non-metallic systems, but might not result in an improvement of the electronic structure prediction for a specific system with either a very small or very large band gap. For this reason, other approaches were suggested to determine the optimal value of α. Here we focus on *ab initio* methods, i.e., without relying on experimental values:

(a) A pure DFT-based solution of the problem proposed by Lany and Zunger [44], where the α-parameter is used to restore Eq. (1.40). This approach only works for localized orbitals, e.g., for defect states in the gap. For delocalized states Δ_{XC} is always zero. The task is to find the optimal fraction α_{opt} leading to $\Delta_{\mathrm{XC}}(\alpha_{\mathrm{opt}}) = 0$.

(b) Minimizing the error with respect to higher-level electronic-structure methods (e.g., GW method) for the ho level [45, 46, 47]. Different to method (a) this approach can be applied to correct the position of extended states such as the valence band maximum (VBM) and conduction band minimum (CBm).

(c) The fraction of exact exchange is chosen as $\alpha = 1/\varepsilon_\infty$, where the high-frequency dielectric constant ε_∞ is calculated from the GGA orbitals [48, 49] or iteratively until $\alpha = 1/\varepsilon_\infty(\alpha)$ [50]. This choice is based on the observation that the difference of GGA and experimental band gaps correlates with ε_∞ and is further motivated with similarities of the COHSEX approximation [51] and the structure of Eq. (1.44). In fact, this approach helps to significantly improve the description of the band gaps.

Usually, these approaches improve the simulation of the electronic structure and in particular the prediction of the band gap in general, but may give different results. For example, in the case of rock salt MgO approach (a) leads to $\alpha = 0.48$ for a hole polaron state (cf. Chapter 2) and approach (c) to $\alpha = 1/\varepsilon_\infty^{\mathrm{PBE}} = 0.33$. In terms of the band gap this results in a discrepancy of 1.1 eV, yet both give a significantly better estimation of the band gap compared to GGA or LDA.

Nowadays, the most widely used hybrid functionals with global mixing parameters are PBE0 [40], HSE (Heyd-Scuseria-Ernzerhof) [52, 53] and B3LYP (Becke, three-parameter, Lee-Yang-Parr) [54]. However, the evaluation of integrals required for the calculation of the exact-exchange energy:

$$E_{\mathrm{EXX}} = -\frac{1}{2}\sum_{i,j}\iint \mathrm{d}\boldsymbol{r}_1\mathrm{d}\boldsymbol{r}_2\, \psi_i^*(\boldsymbol{r}_1)\psi_j^*(\boldsymbol{r}_1)\frac{1}{|\boldsymbol{r}_1-\boldsymbol{r}_2|}\psi_i(\boldsymbol{r}_2)\psi_j(\boldsymbol{r}_2), \tag{1.45}$$

where ψ_i is the ith occupied orbital, or the Fock operator, is computationally expensive for systems with a large number of electrons. The observation that the long-range contribution of the GGA exchange and the EXX in Eq. (1.45) cancel each other motivated the introduction of range-separated Coulomb potentials in Eq. (1.45). The first work of this kind for the EXX was done by Heyd, Scuseria, and Ernzerhof (HSE) [52, 53], by dividing the $1/r$ in the exchange part into a long-range (LR) and short-range (SR) parts:

$$\frac{1}{r} = \underbrace{\frac{\mathrm{erfc}(\omega r)}{r}}_{\mathrm{SR}} + \underbrace{\frac{\mathrm{erf}(\omega r)}{r}}_{\mathrm{LR}}, \tag{1.46}$$

with the error function erf(ωr) and erfc(ωr) $= 1 -$ erf(ωr), and the range-separation parameter ω . For example, for the total XC energy of the HSE functional (mixing PBE and EXX) it follows:

$$E_{\mathrm{XC}}^{\mathrm{HSE}}(\alpha) = \alpha E_{\mathrm{EXX}}^{\mathrm{SR}} + (1-\alpha)E_{\mathrm{PBE\text{-}X}}^{\mathrm{SR}} + E_{\mathrm{PBE\text{-}X}}^{\mathrm{LR}} + E_{\mathrm{PBE\text{-}C}} \tag{1.47}$$

The range-separation parameter ω is numerically tested to give the smallest mean absolute error for a test-set, and $\omega = 0.11$ Bohr^{-1} with $\alpha = 0.25$ was proposed as balanced description that provides a good speed and accuracy for both solids and molecules [53]. Moreover, ω is not only a numerical parameter, it additionally helped to improve the description of metallic systems, since ω incorporates an explicit screening effect. In Fig. 1.4(b) we again tested the prediction of the band gap for the same eight oxides as before with the HSE($\alpha = 0.25$). Indeed, the HSE functional drastically improved the description of the band gap (ME= -0.64 eV, MAE= 0.84 eV, MRE= -0.11, MARE= 0.18). However, in general all PBE band gaps are just shifted by an amount of 1.7 eV with respect to HSE($\alpha = 0.25$). This indicates that already PBE can give meaningful results for properties of closed-shell systems as we have demonstrated here for the band gap and is later shown for the geometry optimization of the polaron. The computationally more expensive HSE functional is only needed for single-point calculations afterwards to obtain electronic KS levels with higher accuracy. Nevertheless, many examples exist where the HSE functional is explicitly needed in order to obtain the proper description of the desired property. An example is the charge-transfer in hybrid inorganic-organic systems [55].

For the sake of completeness we like to mention that the concept of the range-separated Coulomb potential introduced in Eq. (1.46) is utilized for other purposes as well: Baer, Neuhauser, and Livshits [56, 57] used the long-range separation part to cancel the spurious self-repulsion appearing for the long-range LDA XC potential, while short-range contributions of the exact exchange are neglected. To profit from both the proper long-range and short-range behavior of the exact exchange potential Eq. (1.47) has been naturally generalized to:

$$E_{\mathrm{XC}}^{hybrid}(\alpha,\beta,\omega) = \alpha E_{\mathrm{EXX}}^{\mathrm{LR}}(\omega) + (1-\alpha)E_{\mathrm{DFA}}^{\mathrm{LR}}(\omega) + \beta E_{\mathrm{EXX}}^{\mathrm{SR}}(\omega) + (1-\beta)E_{\mathrm{DFA}}^{\mathrm{SR}}(\omega) + E_{\mathrm{DFA}}^{C} \tag{1.48}$$

and its parameter extensively tested on their performance for enthalpies, barrier heights, IPs and EAs [58] of molecules. However, as stated above there are no perfect parameters even for the general case Eq. (1.48), but it rather depends on the property to predict and the regarded system.

1.5 Numeric electronic-structure calculations with FHI-aims

The purpose of this section is to present the main features of the electronic structure software FHI-aims used throughout this work. FHI-aims (Fritz Haber Institute *ab initio* molecular simulations package) [59] is an all-electron, full-potential electronic structure code with numeric atom-centered orbitals (NAOs) used as the basis set. There are other choices for the basis functions present in the field of DFT and quantum-chemistry software packages as well, such as plane waves, Gaussian orbitals, Slater-like orbitals, or even combinations of different types (e.g., the muffin-tin approximation)[5]. The basis functions in FHI-aims have the following form:

$$\varphi_i(\boldsymbol{r}) = \frac{u_i(r)}{r} Y_{lm}(\Omega) \tag{1.49}$$

with the spherical harmonics $Y_{lm}(\Omega)$ and the numerically tabulated radial functions $u_i(r)$. The $u_i(r)$ are obtained by solving the radial Schrödinger-like equation on a logarithmic grid, where an artificial steep potential is added (cut-off potential) to spatially confine the basis functions, which allows for an efficient numerical O(N) integration scheme in the solution of the KS equations [60]. The basis functions are species-dependent, constructed and ordered in a way to give an increasing accuracy with an increasing number of basis functions. The minimal basis consists of the core and valence functions, and is obtained from the spherically symmetric free atoms. This seemingly crude choice already gives a sufficiently good description of the rapidly

[5] An overview of the different choices of basis functions and their implementations in various electronic-structure codes can be found at `https://www.nomad-coe.eu/externals/codes`.

oscillating core functions. On top of the minimal basis additional functions are used, namely hydrogen-like and free-ion radial functions, which are combined with different angular momenta (s, p, d, f, ...) functions (for a detailed discussion of the selection and construction of these functions c.f. Ref. [59]). The additional basis functions are arranged hierarchically in *tiers* according to their contribution to the improvement to the LDA total energy of a dimer for each element.

The basis set is used to expand the KS orbitals ϕ_i^{KS}:

$$\phi_i^{\mathrm{KS}}(\boldsymbol{r}) = \sum_j^{N_{\mathrm{b}}} c_{ij}\varphi_j(\boldsymbol{r}) \tag{1.50}$$

and, with this, to discretize Eq. (1.27) into a generalized eigenvalue problem:

$$\sum_j h_{ij}c_{jl} = \epsilon_l \sum_j s_{ij}c_{jl} \tag{1.51}$$

with the number of basis functions N_{b}, the Hamilton matrix h_{ij} and the overlap matrix s_{ij}:

$$h_{ij} = \int \mathrm{d}\boldsymbol{r}\, \varphi_i(\boldsymbol{r})\hat{h}^{KS}\varphi_j(\boldsymbol{r}) \tag{1.52}$$

$$s_{ij} = \int \mathrm{d}\boldsymbol{r}\, \varphi_i(\boldsymbol{r})\varphi_j(\boldsymbol{r}) \tag{1.53}$$

The complex conjugation is omitted, since only the real-valued real and imaginary part of the of complex spherical harmonics is used for the NAOs in FHI-aims. The integrations in Eqs. (1.52) and (1.53) are evaluated on a logarithmic grid for the radial part and on a Lebedev grid [61] for the angular part. Efficient partitioning of the integration grids as suggested by Becke [62] or Delley [63] takes advantage of the localized nature of the orbitals and allows for tightly converged calculations even for small grid sizes.

Energy derivatives, i.e., forces play a central role in this thesis for the relaxation of the atomic positions, the optimization of the lattice, and the calculation of the phonon spectra. In FHI-aims forces are calculated analytically. For NAOs, additional terms appear beside the Hellmann-Feynman forces Eq. (1.14). Namely, these are the Pulay forces [64], which appear due to the "movement" (i.e. the derivatives w.r.t the nuclei positions) of the incomplete set of numeric atom-centered basis functions, and the electrostatic multipole derivatives [65], which occur due to the truncation of the electrostatic potential beyond a certain multipole moment.

The initial density for a self-consistent KS calculation is constructed from the superposition of the free-atom densities. At the first step, the Hartree and XC potentials are calculated with the resulting density. In order to calculate the Hartree potential accurately, it is interpolated with cubic splines on a dense logarithmic grid. For large molecules and periodic boundary conditions (PBC) the Ewald method [66, 67] is used to account for the long-range contributions of distant atoms. The generalized eigenvalue problem Eq. (1.51) is solved with the aid of the "eigenvalue solvers for petascale applications" (ELPA) library [68], which is based on the standard libraries of linear algebra such as Lapack and ScaLapack. The structure of the FHI-aims code is optimized to allow for massively parallel computing, scaling almost linearly up to tens of thousands of CPUs. The obtained KS orbitals are used to update the density, and the procedure is repeated up to self-consistency, until the so-called self-consistent field (SCF) cycle is converged. During the SCF the Hartree potential and the XC potential are only updated based on the corresponding differences of the density from the previous and the current SCF cycle.

The linear scaling for parallel computing of the exact exchange energy is not directly achievable due to the non-local character of the two-electron Coulomb repulsion integrals appearing in Eq. (1.45). However, this can be obtained by using the resolution of identity technique (cf. Ref. [69] for details on this scheme in connection with the NAOs), which has been implemented for periodic systems recently [70].

The convergence of the numerical solution (total energies, eigenvalues, and densities) with respect to various criteria can be checked with the pre-defined default settings *light*, *tight*, and *really tight*. This includes not only the number of basis functions (the basis set tier), but also the integration grids, the accuracy of the Hartree potential, and the radius of the cut-off potential. In this work, the system size (up to 1,000 atoms) does not allow to easily go beyond *light* settings. However, we do test the convergence for smaller unit cells, cf. App. E, and find that the *light* settings are sufficiently accurate for the polaron binding energy and polaron energy level. Convergence parameters for the numerical self-consistency have to be set and tested explicitly. The same applies to the convergence of the number of k-points.

1.6 The harmonic approximation and phonons

With the approximations introduced in Sec. 1.4 we now have efficient methods at hand to calculate points on the PES even for large systems including many nuclei and electrons. Yet, we have treated the electrons separately from the dynamics of the nuclei. To account for the vibrational dynamics, we can explore the PES $E_{\text{el}}(\boldsymbol{R})$ in the vicinity of a minimum $\boldsymbol{R} = \{\boldsymbol{\tau}^0_{\kappa\boldsymbol{p}}\}$ with the vector of the equilibrium positions $\{\boldsymbol{\tau}^0_{\kappa\boldsymbol{p}}\}$, where κ numbers the atoms in the basis of the unit cell and $\boldsymbol{p}$ denotes the index of the lattice vector as it was introduced in Eq. (1.1). The total energy is expanded in terms of small displacements $\Delta\boldsymbol{\tau}_{\kappa\boldsymbol{p}}$ from $\boldsymbol{\tau}^0_{\kappa\boldsymbol{p}}$:

$$\begin{aligned} E_{\text{el}}(\boldsymbol{R}) &= E_{\text{el}}(\{\boldsymbol{\tau}^0_{\kappa\boldsymbol{p}}\}) \\ &+\frac{1}{2}\sum_{\substack{\kappa,\alpha,\boldsymbol{p}\\ \kappa',\alpha',\boldsymbol{p}'}} \left.\frac{\partial^2 E_{\text{el}}(\boldsymbol{R})}{\partial\tau_{\kappa\alpha\boldsymbol{p}}\partial\tau_{\kappa'\alpha'\boldsymbol{p}'}}\right|_{\{\boldsymbol{\tau}^0_{\kappa\boldsymbol{p}}\}} \Delta\tau_{\kappa\alpha\boldsymbol{p}}\Delta\tau_{\kappa'\alpha'\boldsymbol{p}'} + \mathcal{O}(\Delta\tau^3), \end{aligned} \tag{1.54}$$

The Greek indices denote the Cartesian coordinates of the displacement. The first-order term of the expansion in Eq. (1.54) vanishes, since $\{\boldsymbol{\tau}^0_{\kappa\boldsymbol{p}}\}$ is a minimum on the PES. The second-order term contains the *interatomic force constants* defined as:

$$C_{\kappa\alpha\boldsymbol{p},\kappa'\alpha'\boldsymbol{p}'} = \left.\frac{\partial^2 E_{\text{el}}(\boldsymbol{R})}{\partial\tau_{\kappa\alpha\boldsymbol{p}}\partial\tau_{\kappa'\alpha'\boldsymbol{p}'}}\right|_{\{\boldsymbol{\tau}^0_{\kappa\boldsymbol{p}}\}} = \frac{\partial\,\boldsymbol{F}_{\kappa'\alpha'\boldsymbol{p}'}}{\partial\tau_{\kappa\alpha\boldsymbol{p}}}, \tag{1.55}$$

where we have introduced the force

$$\boldsymbol{F}_{\kappa\alpha\boldsymbol{p}} = \frac{\partial\,E_{\text{el}}(\boldsymbol{R})}{\partial\tau_{\kappa\alpha\boldsymbol{p}}}. \tag{1.56}$$

If the expansion is truncated after the quadratic term, Eq. (1.54) is called the *harmonic approximation*. By Fourier transforming Eq. (1.55) we obtain the *dynamical matrix*:

$$D_{\kappa\alpha,\kappa'\alpha'}(\boldsymbol{q}) = (M_\kappa M'_\kappa)^{-1/2}\sum_{\boldsymbol{p}} C_{\kappa\alpha 0,\kappa'\alpha'\boldsymbol{p}'}\exp(i\boldsymbol{q}\boldsymbol{\tau}_{\boldsymbol{p}}), \tag{1.57}$$

where the dynamical matrix has been weighted with the nuclei masses to simplify the equations of motion $M_\kappa\frac{\partial^2}{\partial t^2}\Delta\boldsymbol{\tau}_{\kappa\boldsymbol{p}} = \sum_{\kappa'\boldsymbol{p}'} C_{\kappa\boldsymbol{p}\kappa'\boldsymbol{p}'}\Delta\boldsymbol{\tau}_{\kappa'\boldsymbol{p}'}$. The eigenvectors $e_{\kappa\alpha,\nu}(\boldsymbol{q})$ of D are called phonon modes and the corresponding eigenvalues $\omega_{\boldsymbol{q}\nu}$ are phonon frequencies. A phonon is a collective vibration of atoms expanded in plane waves. As can be seen from the solution of the eigenvalue problem:

$$\sum_{\kappa'\alpha'} D_{\kappa\alpha,\kappa'\alpha'}(\boldsymbol{q})e_{\kappa'\alpha',\nu}(\boldsymbol{q}) = \omega^2_{\boldsymbol{q}\nu}e_{\kappa\alpha,\nu}(\boldsymbol{q}) \tag{1.58}$$

the phonons decouple and, thus, each phonon mode represents an independent harmonic oscillator. The $3N_{\text{nuc}}$ eigenvectors, where N_{nuc} is the number of nuclei in the unit cell, form a complete orthonormal basis for the nuclear coordinates:

$$\sum_{\nu} e^*_{\kappa'\alpha',\nu}(\boldsymbol{q}) e_{\kappa\alpha,\nu}(\boldsymbol{q}) = \delta_{\kappa\kappa'}\delta_{\alpha\alpha'} \tag{1.59}$$

$$\sum_{\kappa,\alpha} e^*_{\kappa'\alpha',\nu}(\boldsymbol{q}) e_{\kappa\alpha,\nu}(\boldsymbol{q}) = \delta_{\nu\nu'}. \tag{1.60}$$

We have just obtained the solution for the classical dynamics of the nuclei. Formally, the dynamics can be quantized using the Hamiltonian for the phonons:

$$\hat{H}_{\text{ph}} = \frac{1}{2} \sum_{\substack{\kappa,\alpha,\boldsymbol{p} \\ \kappa',\alpha',\boldsymbol{p}'}} C_{\kappa\alpha\boldsymbol{p},\kappa'\alpha'\boldsymbol{p}'} \Delta\tau_{\kappa\alpha\boldsymbol{p}} \Delta\tau_{\kappa'\alpha'\boldsymbol{p}'} - \sum_{\kappa,\alpha,\boldsymbol{p}} \frac{\hbar^2}{2M_\kappa} \frac{\partial^2}{\partial\tau^2_{\kappa,\alpha,\boldsymbol{p}}}. \tag{1.61}$$

The ground-state energy has been omitted, since the solutions of Eq. (1.61) do not change, when the energy is shifted by an arbitrary constant. Eq. (1.61) can be expressed via phonon creation and annihilation operators $a^+_{\boldsymbol{q}\nu}$ and $a_{\boldsymbol{q}\nu}$ with the commutation relations for bosons $[a_{\boldsymbol{q}\nu}, a^+_{\boldsymbol{q}\nu}] = \delta_{\nu\nu'}\delta_{\boldsymbol{q}\boldsymbol{q}'}$ and $[a_{\boldsymbol{q}\nu}, a_{\boldsymbol{q}\nu}] = [a^+_{\boldsymbol{q}\nu}, a^+_{\boldsymbol{q}\nu}] = 0$. With this, the form of the phonon Hamiltonian simplifies to:

$$\hat{H}_{\text{ph}} = \sum_{\boldsymbol{q}\nu} \hbar\omega_{\boldsymbol{q}\nu} \left[a^+_{\boldsymbol{q}\nu} a_{\boldsymbol{q}\nu} + 1/2\right]. \tag{1.62}$$

The formal derivation can be found, e.g., in Ref. [71]. The Hamiltonian in Eq. (1.62) has the spectrum of eigenvalues identical to the classical solution of Eq. (1.58). However, the total energy of the phonons differs by the *zero-point energy* $\frac{1}{2}\sum_{\boldsymbol{q}\nu} \hbar\omega_{\boldsymbol{q}\nu}$, which accounts for the *uncertainty principle* for quantum objects. The particle number operator $a^+_{\boldsymbol{q}\nu} a_{\boldsymbol{q}\nu}$ gives the number of phonons $N_{\boldsymbol{q}\nu}$ in the ν-th mode at $\boldsymbol{q}$. A formal relation between $N_{\boldsymbol{q}\nu}$ (also known as occupation number) and the amplitude of the classical vibration for the same mode can be derived by requiring that the classical and quantum-mechanical oscillator have the same energy:

$$\underbrace{\omega^2_{\boldsymbol{q}\nu} M_0 A^2_{\boldsymbol{q}\nu}/2}_{\text{classical}} = \underbrace{\hbar\omega_{\boldsymbol{q}\nu} N_{\boldsymbol{q}\nu}}_{\text{quantum mechanical}}$$

$$\rightarrow A_{\boldsymbol{q}\nu} = \sqrt{\frac{2\hbar N_{\boldsymbol{q}\nu}}{M_0 \omega_{\boldsymbol{q}\nu}}} = \sqrt{2\left\langle \hat{Q}^2_{\boldsymbol{q}\nu} \right\rangle}, \tag{1.63}$$

where we have omitted the zero-point contribution to make comparison with the classical amplitudes $A_{\boldsymbol{q}\nu}$. Eq. (1.63) outlines another difference between the classical and quantum mechanical case: The classical amplitude is $\sqrt{2}$times larger than the standard deviation of the phonon probability amplitude $\sqrt{\langle \hat{Q}^2_{\boldsymbol{q}\nu} \rangle}$ for the same energy.

Usually, the classical description of the nuclei, i.e., Eq. (1.55), is used for the numerical computation of phonon properties. A rather straightforward strategy is the frozen-phonon approach, where the atoms are explicitly displaced by $\Delta\tau_{\kappa\alpha\boldsymbol{p}}$, and the forces are computed from SCF DFT calculations (here with FHI-aims). The number of different displacements that have to be considered depends on the crystal symmetry, and is typically small for systems with a high symmetry. Based on the forces obtained from the different configurations, the interatomic force constants Eq. (1.55) are approximated as:

$$C_{\kappa\alpha\boldsymbol{p},\kappa'\alpha'\boldsymbol{p}'} \approx \frac{F_{\kappa'\alpha'\boldsymbol{p}'}(\Delta\tau_{\kappa\alpha\boldsymbol{p}}) - F_{\kappa'\alpha'\boldsymbol{p}'}(0)}{\Delta\tau_{\kappa\alpha\boldsymbol{p}}}. \tag{1.64}$$

In phonopy [72], the python package employed in this work for calculation of the phonon properties, a modified Parlinski-Li-Kawazoe method is used to fit the force constants from the forces and displacements. The calculated phonon properties are usually insensitive to the displacement amplitude $|\Delta\tau_{\kappa\alpha\boldsymbol{p}}|$ within a reasonable range, and is set by default to 0.01Å. Yet, too small values of $|\Delta\tau_{\kappa\alpha\boldsymbol{p}}|$ imply small energy differences and, thus, leads to inaccuracies in the force evaluation and should be avoided. A more severe problem of the frozen-phonon approach is the convergence with the supercell size. The forces are calculated in a $N \times N \times N$ supercell, while the interatomic force constants are transformed to the reciprocal unit cell on a $N \times N \times N$ $\boldsymbol{q}$-point grid. The dynamical matrix is then Fourier-interpolated on a much denser $\boldsymbol{q}$-point grid in order to get a better estimation for integrated quantities, e.g., the density of states, or the phonon band structure. However, for a very sparse initial grid this interpolation might still give bad or even incorrect results. Therefor, a test for the supercell convergence is always recommended. Note that the interatomic force constants can be also obtained from density-functional perturbation theory (DFPT), where the energy gradients are expanded in terms of perturbations of the density. For a detailed discussion of this approach we refer to Ref. [73] or for the explicit implementation in the FHI-aims code Ref. [74].

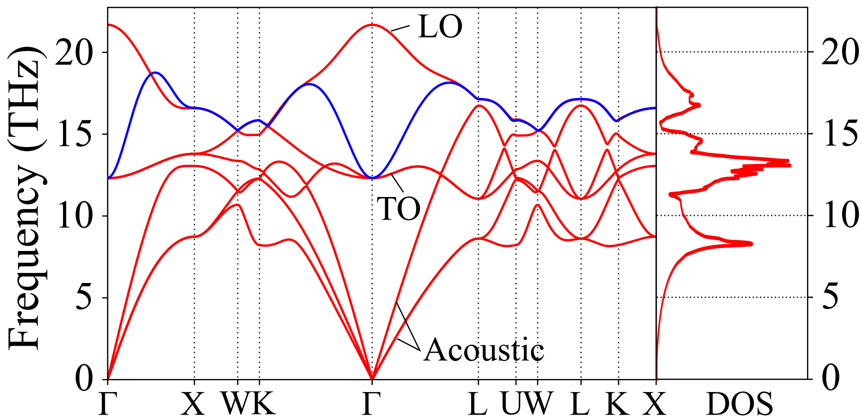

FIGURE 1.5: The phonon band structure along the high-symmetry directions of the bcc BZ for rock salt MgO calculated for a $2 \times 2 \times 2$ cubic supercell. The blue line indicates the wrong behavior of the LO mode without the non-analytic term correction at Γ (cf. [75] and see text for details), where the topmost red line shows the proper LO/TO splitting.

A prototypical phonon structure of a polar material is shown for rock salt MgO in Fig. 1.5. Around the Γ-point, the three acoustical branches with linear dispersion and the $3N_{\text{nuc}} - 3$ optical branches can be observed. However, special care has to be taken for the optical branches at small wave vectors. For $\boldsymbol{q} \to 0$ the distortion introduced by the longitudinal modes is accompanied by a macroscopic electric field, which is not lattice-periodic and therefore can only be simulated in the limit of an infinitely large supercell. Within the finite-differences approach the distortions at the Γ-point are calculated in the unit cell, and the macroscopic field is canceled. Consequently, the longitudinal optical (LO) and transversal optical (TO) modes appear degenerate at Γ. To account for the proper LO/TO splitting, non-analytic corrections (cf. [75]) are used in order to avoid very large supercell calculations. The non-analytic correction can be calculated using the Born effective charges and the high-frequency dielectric constant. A problem of a similar kind is encountered in the simulations of polarons in finite supercells, where the scattering of excess electrons or holes with the LO modes is an important mechanism for the formation of polarons.

1.7 The electron-phonon interaction and polarons

The decoupling of the electron and nuclei dynamics can only be regarded as a first step for the estimation of the solid's properties. It cannot entirely explain the behavior of charge carriers in solids and associated temperature effects. For some scenarios the interaction of phonons and electrons creates entities with unique properties strongly dependent on the temperature. The electron-phonon (el-ph) coupling is responsible for a number of exotic phenomena, for example superconductivity, but also explains seemingly trivial effects on a quantum-mechanical level, e.g., the temperature dependence of optical spectra (e.g. optical absorption edge or excitonic peaks) of semiconductors and insulators, or the resistivity of metals.

The following section gives an introductory overview of the electron-phonon interaction in order to explain the main challenges and to introduce the notations. In this work, the el-ph contributions to the KS eigenvalues are not evaluated explicitly, but rather implicitly by exploring the potential-energy surface due to the distortion of the nuclei. This has the advantage of including anharmonic effects, which are hard to access with DFPT techniques.

1.7.1 The electron-phonon interaction

In the framework of KS DFT the effect of phonons on the single-electron KS states are given as the change of the effective potential V^{KS}:

$$V^{\mathrm{KS}}(\boldsymbol{r},\{\tau_{\kappa\alpha\boldsymbol{p}}\}) = V^{\mathrm{KS}}(\boldsymbol{r},\{0\}) + \Delta V^{\mathrm{KS}}(\boldsymbol{r},\{\Delta\tau_{\kappa\alpha\boldsymbol{p}}\})\,, \tag{1.65}$$

where V^{KS} depends parametrically on the atomic displacements $\{\Delta\tau_{\kappa\alpha\boldsymbol{p}}\}$, and $\Delta V^{\mathrm{KS}}(\boldsymbol{r},\{\tau_{\kappa\alpha\boldsymbol{p}}\}) = V^{\mathrm{KS}}(\boldsymbol{r},\{\Delta\tau_{\kappa\alpha\boldsymbol{p}}\}) - V^{\mathrm{KS}}(\boldsymbol{r},\{0\})$. For small displacements the change of ΔV^{KS} can be treated in a lower-oder power expansion of the nuclear displacements:

$$\begin{aligned}\Delta V^{\mathrm{KS}}(\boldsymbol{r},\{\tau_{\kappa\alpha\boldsymbol{p}}\}) = \quad & \sum_{\kappa\alpha\boldsymbol{p}} \frac{\partial V^{\mathrm{KS}}}{\partial \tau_{\kappa\alpha\boldsymbol{p}}}\Delta\tau_{\kappa\alpha\boldsymbol{p}} + \\ & \sum_{\substack{\kappa,\alpha,\boldsymbol{p}\\ \kappa',\alpha',\boldsymbol{p}'}} \frac{\partial V^{\mathrm{KS}}}{\partial \tau_{\kappa\alpha\boldsymbol{p}}\partial\tau_{\kappa',\alpha',\boldsymbol{p}'}}\Delta\tau_{\kappa\alpha\boldsymbol{p}}\Delta\tau'_{\kappa\alpha\boldsymbol{p}} + \dots\end{aligned} \tag{1.66}$$

As for the PES, including only terms up to the second order is often refered to as the *harmonic approximation* of the electron-phonon coupling. In the theory proposed by Allen, Heyne, and Cardona [76, 77] this includes the Fan and the Debye-Waller terms, which are commonly evaluated in the framework of DFPT [78]. Using $v_{\mathrm{eff}} = V^{\mathrm{KS}}(\boldsymbol{r},\{\tau_{\kappa\alpha\boldsymbol{p}}\})$ in Eq. (1.27) and averaging over the phonon coordinates, the change of the KS energy levels due to the el-ph coupling in the harmonic approximation is

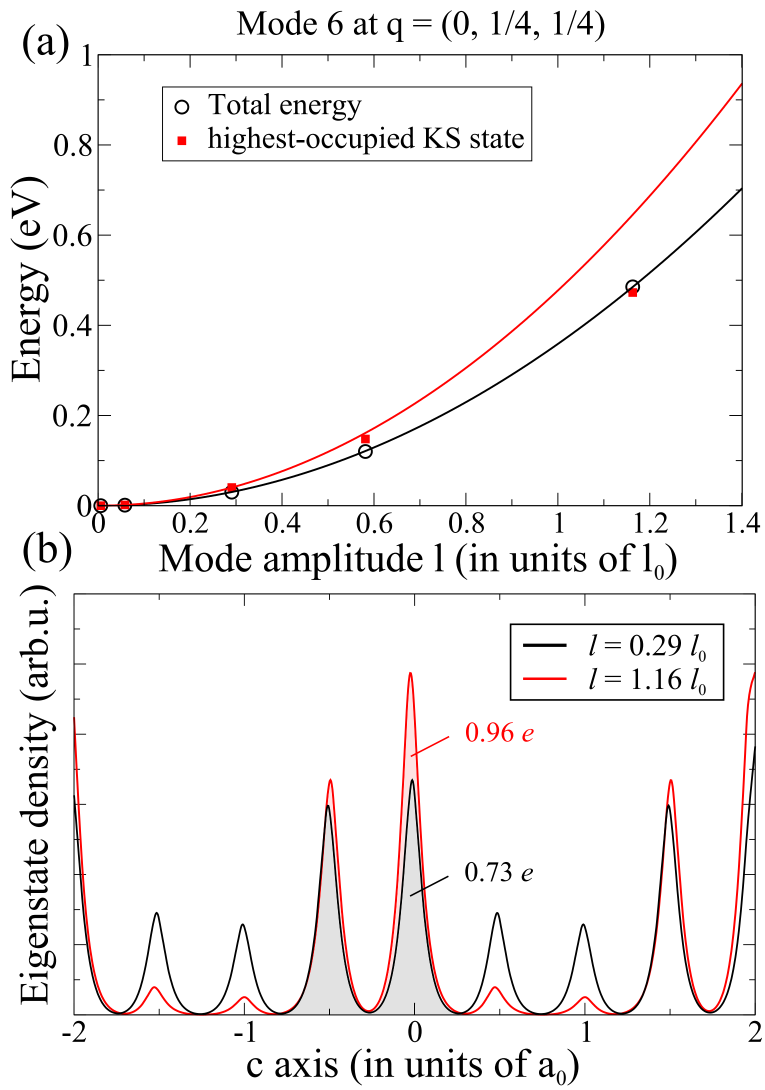

FIGURE 1.6: (a) The dependence of the total energy and the highest-occupied state on the displacement along the LO mode at $\boldsymbol{q}$-point (0, 1/4, 1/4) of the irreducible BZ for rock salt MgO. The displacement (mode amplitude) is given in units of the zero-point amplitude $l_0 = (\hbar/2M_0\omega_\nu)^{1/2} = 0.17$ Å. The solid lines are parabolic fits for the two smallest displacements. The deviation of the actual red squares from the red parabola demonstrate the misconception of the harmonic approximation for the el-ph coupling of the KS energy levels. (b) The ho KS eigenstate density averaged in the plane perpendicular to the c axis of the cubic unit cell, as a function of the coordinate along the c axis (in units of the in-plane lattice constant a_0 = 4.211 Å), calculated for atomic positions corresponding to two different displacements l along the same mode at the same q-point as in (a). The gray- and red-shaded areas under the two highest peaks contain 0.73 and 0.96 of the electron charge in this state, respectively. The $1 \times 1 \times 2$ supercell of the conventional cell for the simulated mode is ranging from -1 to 1 in the graph.

obtained as:

$$\left\langle \varepsilon_i^{\mathrm{KS}}\left(\left\{U_{\nu q}\right\}, z\right)\right\rangle_{\mathrm{ph}} = \varepsilon_i^{\mathrm{KS}}(0) + \sum_{\nu \boldsymbol{q}} \frac{1}{2} z^2 \frac{\partial^2}{\partial z^2} \varepsilon_i^{\mathrm{KS}}\left(z U_{\nu q}\right)\Big|_{z=0}, \tag{1.67}$$

where $U_{\nu \boldsymbol{q}}$ is the normalized real-space displacement corresponding to the phonon eigenvector $\boldsymbol{e}_{\nu \boldsymbol{q}}$. Similar to the phonon problem, this expression can be evaluated using the linear-response technique DFPT (again cf. Ref [74] for the explicit implementation in FHI-aims) or with the frozen-phonon approach. A problem already pointed out by Antonius *et al.* [79] and demonstrated in Fig. 1.6, panel a, is that often the harmonic approximation used in Eq. (1.67) is not sufficient for an appropriate description of the change of KS eigenvalues, even for small phonon amplitudes (this is in particular critical for the evaluation of the zero-point renormalization of the KS energy levels, where often only second-order terms are considered). Instead, large anharmonic contributions[6] can be observed. To demonstrate this, the atoms in MgO were displaced along the mode $\nu = 6$ at $q = (0, 1/4, 1/4)$, and the change in energies has been explicitly evaluated for several amplitudes of the displacement. The quadratic fit for the highest occupied KS state based on the smallest displacements deviates significantly from the actual values for larger amplitudes, although the total energy shows an almost perfect harmonic behavior. To explain this strong anharmonicity, we plotted the ho KS eigenstate density for two different amplitudes $l = 1.16 l_0$ and $l = 0.26 l_0$ of this LO mode. It can be seen that the density of the state increases its localization with increasing the distortion along the mode. This means that the phonon mode carries a localized charged along its direction, which in turn causes (macroscopic) polarization effects. Yet, they are not (or at most only partly) present for small displacements, where the charge is in fact still delocalized (see black curve in Fig. 1.6, panel b). This strong el-ph coupling for the KS states makes the use of linear-response techniques not applicable for strongly distorted lattice configurations, as in the case of small-polaron formation.

1.7.2 The polaron and model systems

The concept of a polaron is now almost 90 years old. The pioneering work was done by Landau [6], Pekar [7], and Fröhlich [8]. It is an extension of the single-electron picture in solids to include the electron-phonon (el-ph) interaction leading to a renormalization of the charge-carrier mass, localization, and mobility. This has extensive consequences on how materials can be used, e.g., in solar cells, photocatalysts, or electric devices. Thus, predicting polaronic behavior is crucial for designing new functional materials.

Despite the aim of this chapter to introduce *ab initio* concepts, this section deals only with model Hamiltonians for the polaron. However, the models are useful for introducing the essential physics of the polaron. An *ab initio* approach for calculating

[6]By anharmonic contributions we denote terms higher than second order in the Taylor expansion of the KS eigenvalues as a function of phonon displacements.

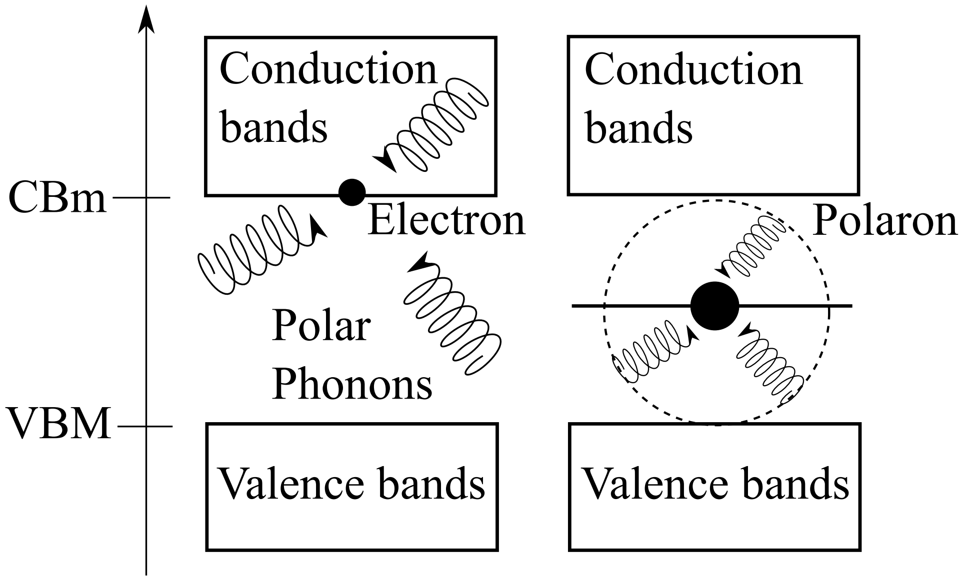

FIGURE 1.7: Formation of a polaron: A slow electron (or hole) is dressed by a cloud of polar phonon modes leading to a renormalization of the charge carrier mass (indicated by the larger circle), localization, and as a consequence its mobility. Due to the el-ph interaction a separate level appears in the gap – the polaron level.

polaron properties is then presented and is the main object of this work. At the end of this section we will summarize the deficiencies of the polaron models introduced here.

Since the theory of polarons and in particular bi-polarons is discussed by several authors as a potential theory for high-temperature superconductivity [80, 81], an extensive analytical and numerical work on (simplified) model systems can be found in the literature. Moreover, a variety of mathematical tools were tested on this playground as a representative scalar fermion-boson field interaction, e.g. Feynman's path integral method [82, 83], (diagrammatic quantum) Monte Carlo simulations [84, 85], or the Green's function approach [86]. For a detailed review of the early polaron theory we refer to Ref. [87], and for the most recent results to Ref. [88]. Although, these models are not based on *first principles*, they give a helpful insight into the polaron behavior. Later it will be shown that these models can be used for correcting the *ab initio* simulations *a posteriori* in order to account for long-range effects with a reduced computational effort.

Overview of semi-empirical theories of the continuum polaron

Schematically, the polaron is described by the following scenario depicted in Fig. 1.7: if an excess electron is put at the conduction-band minimum (CBm), the dipole of polar phonon modes start to interact with the electron. As a consequence, on average over time the electron appears to be dressed with the polar phonon modes. If the

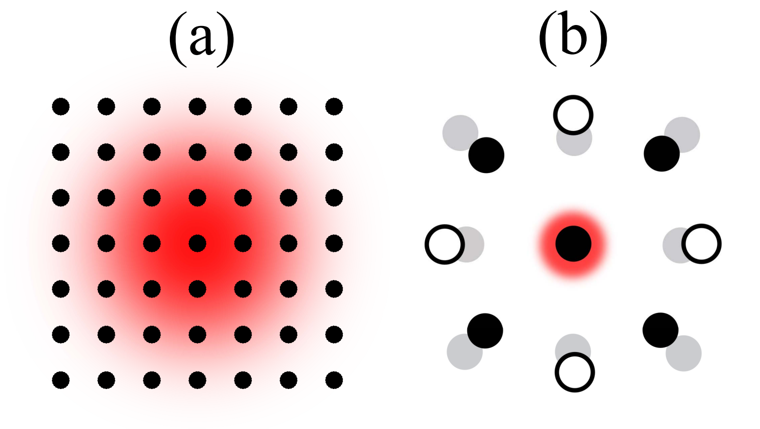

FIGURE 1.8: Localization of the electron wave function for different coupling strength: (a) In the case of weak coupling large polarons form and the wave function is delocalized over several hundreds (or more) atoms. (b) Strong el-ph coupling leads to small-polaron formation, and the charge carrier is usually strongly localized around a single atomic site and the geometry next to the central atoms is noticeably distorted.

electron moves (slowly) through the crystal, the cloud of phonons will accompany it. This quasiparticle is named polaron – a portmanteau of polar and electron first used by Solomon Pekar. The actual change of the electron properties depend on the strength of the coupling. A rough but quick estimation is given by the Fröhlich coupling constant:

$$\alpha_{\mathrm{F}} = e^2 \sqrt{\frac{m_{\mathrm{b}}}{2\hbar^3 \omega_{\mathrm{LO}}}} \left(\frac{1}{\epsilon_\infty} - \frac{1}{\epsilon_0} \right) \tag{1.68}$$

with the band mass m_{b}, the frequency of the LO mode at the Γ-point, the macroscopic high-frequency dielectric constant ϵ_∞ and the static dielectric constant ϵ_0. The range $\alpha_{\mathrm{F}} < 1$ is associated with the weak-coupling region. For this region the number of phonons N_{ph} coupling to the charge carrier is $N_{\mathrm{ph}} = \alpha_{\mathrm{F}}/2$ (i.e., smaller than one). Values of $\alpha_{\mathrm{F}} > 5$ correspond to the strong-coupling regime, and the range $1 < \alpha_{\mathrm{F}} < 5$ is referred to as the intermediate-coupling regime. However, the limits for the different coupling regimes are not strict. Especially for the case of strong el-ph coupling, the actual consequences for the charge carrier depend strongly on the microscopic properties of the system, which are not taken into account by the descriptor α_{F}. This issue is investigated in detail in Ch. 3.

This classification into different strengths is based on the solutions of the Hamiltonian proposed by Herbert Fröhlich [8] in 1954[7]. For his model Fröhlich made the following assumptions:

1. The regarded system has two different kinds of atoms in the basis with a single LO mode only. This implies that the model is applicable only to simple crystal

[7]Historically, the first Hamiltonian for the polaron in the strong-coupling regime was derived by Pekar. However, Fröhlich's Hamiltonian includes all coupling limits correctly, and Pekar's Hamiltonian can be obtained by a canonical transformation as will be shown later.

structures.

2. The radius of the polaron (i.e., the extent of the lattice distortion and of the excess charge) is large compared to the size of the unit cell. As a consequence, the host system is treated as a continuous polarizable medium, where microscopic properties are neglected.

3. Only the interaction with the LO modes close to the Γ-point is taken into account and, thus, the dispersion of the mode is neglected.

4. The excess charge carrier (hole or electron) is placed at the top or bottom of the band extremum at k_0.

Based on these assumptions Fröhlich derived the effective (single-electron) Hamiltonian through quantization of macroscopic expressions of the induced polarization field as follows:

$$\begin{aligned}\hat{H}_{\text{polaron}} = & \quad \hat{H}_{\text{kin,eff}} + \hat{H}_{\text{ph}} + \hat{H}_{\text{el-ph}} \\ = & \quad -\frac{\hbar^2}{2m_{\text{b}}}\nabla^2 + \sum_{\boldsymbol{q}} \hbar\omega_{\text{LO}} a_{\boldsymbol{q}}^{+} a_{\boldsymbol{q}} + \sum_{\boldsymbol{q}} \left(V_{\boldsymbol{q}} a_{\boldsymbol{q}} \mathrm{e}^{i\boldsymbol{q}\boldsymbol{r}} + h.c. \right). \end{aligned} \tag{1.69}$$

The first term $\hat{H}_{\text{kin,eff}}$ represents the effective kinetic energy of the excess charge. The second term $\hat{H}_{\text{ph}}$ is the total energy of the LO modes with frequency ω_{LO} and momentum $\boldsymbol{q}$, where the zero-point energy has been neglected, and the last term $\hat{H}_{\text{el-ph}}$ is the el-ph interaction term with the Fourier components of the electron-nuclei potential $V_{\boldsymbol{q}}$:

$$V_{\boldsymbol{q}} = -i\frac{\hbar\omega_{\text{LO}}}{|\boldsymbol{q}|}\left(\frac{4\pi\alpha_{\text{F}}}{\Omega}\right)^{1/2}\left(\frac{\hbar}{2m_{\text{b}}\omega_{\text{LO}}}\right)^{1/4} \tag{1.70}$$

The linear el-ph interaction term $\hat{H}_{\text{el-ph}}$ is responsible for the excitation of a LO phonon mode with momentum $\boldsymbol{q}$ due to the scattering of an electron plane wave with momentum $\boldsymbol{k}$. In bra-ket notation the initial wave function $|\boldsymbol{k}, 0\rangle = \mathrm{e}^{i\boldsymbol{k}\boldsymbol{r}}\,|0\rangle$ changes to $|\boldsymbol{k}-\boldsymbol{q}, 1_{\boldsymbol{q}}\rangle$, where $|0\rangle$ corresponds to the phonon vacuum, which illustrates the meaning of the el-ph matrix elements:

$$\langle \boldsymbol{k}-\boldsymbol{q}, 1_{\boldsymbol{q}}|\, \hat{H}_{\text{el-ph}}\, |\boldsymbol{k}, 0\rangle = V_{\boldsymbol{q}}^{*}. \tag{1.71}$$

Despite the simple form of the polaron Hamiltonian Eq. (1.69), it is not analytically solvable. However, Fröhlich obtained some physical insights with the aid of perturbation theory regarding $\hat{H}_{\text{el-ph}}$ as a small perturbation of the electron-phonon system. Obviously, the matrix elements yield no diagonal elements, and the second-order perturbation energy reads as:

$$E_{\boldsymbol{k}} = \frac{\hbar^2 k^2}{2m_{\text{b}}} - \sum_{\boldsymbol{q}} \frac{|V_{\boldsymbol{q}}|^2}{\hbar^2(\boldsymbol{k}-\boldsymbol{q})^2/2m_{\text{b}} + \omega_{\text{LO}} + \hbar^2 k^2/2m_{\text{b}}}. \tag{1.72}$$

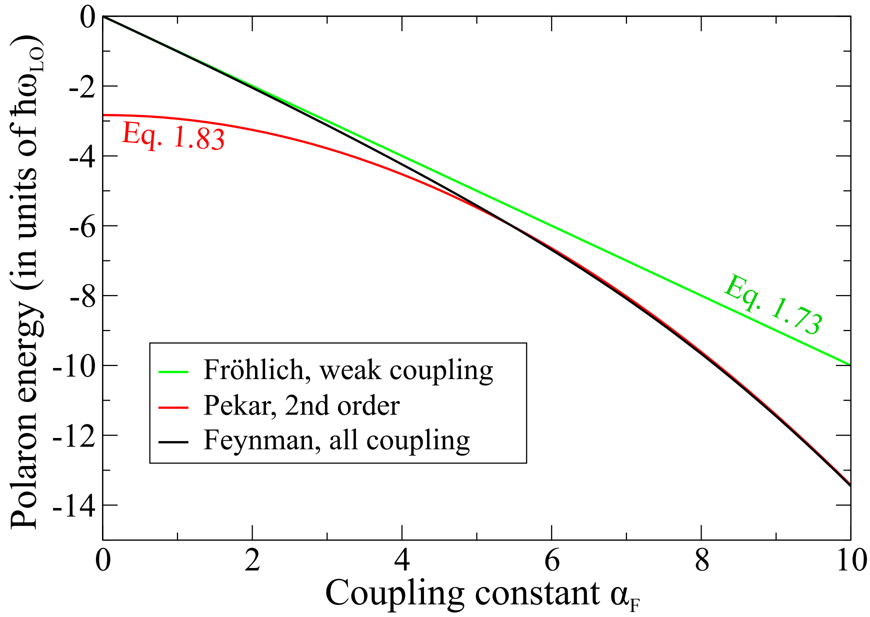

FIGURE 1.9: The polaron binding energy for the Fröhlich Hamiltonian Eq. (1.69) as a function of the el-ph coupling strength α_{F} for different approximations.

For small electron momenta $\boldsymbol{k}$ (we assume here that $\boldsymbol{k}$ is close to the top or bottom of the band extremum at the Γ point $k_0 = 0$) Fröhlich derived for the total energy of the polaron $\langle \hat{H}_{\text{polaron}} \rangle$:

$$E_k = \frac{\hbar^2 k^2}{2m_{\mathrm{p}}} - \hbar\omega_{\mathrm{LO}}\alpha_{\mathrm{F}}, \tag{1.73}$$

where we refer to the second term as binding energy of the polaron E_{bind}(i.e., the rest energy of the polaron). For the polaron mass m_{p} Fröhlich derived:

$$m_{\mathrm{p}} = m^*(1 + \alpha_{\mathrm{F}}/6). \tag{1.74}$$

Even in the weak-coupling regime the el-ph interaction is attractive and increases the mass of charge carriers. However, for larger values of α_{F} the el-ph interaction cannot be considered as a small perturbation and Eq. (1.73) will break down.

Based on the analysis by Landau [6] of electron self-trapping, Pekar [7] calculated the properties of the polaron in the strong-coupling regime. However, the Landau and Pekar expressions were just derived from properties of a classical polarizable continuous medium. The derivation presented in the remaining part of this section starts from the (semi-empirical) quantum-mechanical Fröhlich Hamiltonian and is demonstrating the consistencies among the approximate solutions – from weak- to strong-coupling – of the Fröhlich Hamiltonian. We follow strictly the derivation given in Ref. [89]. For large values of α_{F} an adiabatic approach for the total wave function is plausible: if the coupling is strong, the charge carrier will follow the ion movement adiabatically.

Accordingly, we make the ansatz:

$$|\Phi\rangle = |\varphi\rangle \, |\chi\rangle \, , \tag{1.75}$$

where φ and χ are the electronic and nuclear wave functions, respectively. This leads for the expectation value of Eq. (1.69) to:

$$\begin{aligned}\langle \hat{H}_{\text{polaron}} \rangle = \quad & -\langle \varphi | \frac{\hbar^2}{2m^*} \nabla^2 | \varphi \rangle \\ & + \langle \chi | \sum_{\boldsymbol{q}} \hbar\omega_{\text{LO}} a_{\boldsymbol{q}}^{+} a_{\boldsymbol{q}} + \sum_{\boldsymbol{q}} \left(V_{\boldsymbol{q}} a_{\boldsymbol{q}} \rho_{\boldsymbol{q}} + h.c. \right) | \chi \rangle \, ,\end{aligned} \tag{1.76}$$

where the Fourier transform of the excess-charge distribution is given by $\rho_{\boldsymbol{q}} = \langle \varphi | \mathrm{e}^{i\boldsymbol{q}\boldsymbol{r}} | \varphi \rangle$. With the canonical transformation for the phonon operators:

$$S = \exp \left[\sum_{\boldsymbol{q}} \left(\frac{V_{\boldsymbol{q}} \rho_{\boldsymbol{q}}}{\hbar\omega_{\text{LO}}} a_{\boldsymbol{q}} - \frac{V_{\boldsymbol{q}}^{*} \rho_{\boldsymbol{q}}^{*}}{\hbar\omega_{\text{LO}}} a_{\boldsymbol{q}}^{*} \right) \right] \tag{1.77}$$

the phonon vacuum provides a minimum for the last two terms in Eq. (1.76) resulting in:

$$\langle 0 | S^{-1} \left(\sum_{\boldsymbol{q}} \hbar\omega_{\text{LO}} a_{\boldsymbol{q}}^{+} a_{\boldsymbol{q}} + \sum_{\boldsymbol{q}} \left(V_{\boldsymbol{q}} a_{\boldsymbol{q}} \rho_{\boldsymbol{q}} + h.c. \right) \right) S | 0 \rangle = -\sum_{\boldsymbol{q}} \frac{|V_{\boldsymbol{q}}|^2 |\rho_{\boldsymbol{q}}|^2}{\hbar\omega_{\text{LO}}} . \tag{1.78}$$

For a detail derivation we refer to Ref. [89]. Consequently, the polaron binding energy in the strong-coupling limit is given by:

$$E_{\text{bind}} = -\langle \varphi | \frac{\hbar^2}{2m^*} \nabla^2 | \varphi \rangle - \sum_{\boldsymbol{q}} \frac{|V_{\boldsymbol{q}}|^2 |\rho_{\boldsymbol{q}}|^2}{\hbar\omega_{\text{LO}}} \tag{1.79}$$

still depending on the electronic degrees of freedom. This result was first derived by Pekar[8], which is why we refer to it in this work as the Pekar polaron or Pekar model. To find φ maximizing the absolute value of the binding energy, Pekar chose different trial functions. Here, we choose a simple exponentially decaying function for the minimization:

$$\varphi(\boldsymbol{r}) = N \mathrm{e}^{-|\boldsymbol{r}|/r_{\text{P}}}, \tag{1.80}$$

with the normalization constant $N = 1/\sqrt{\pi r_{\text{p}}^3}$ and the polaron radius r_{p}. Note that the anisotropy of the function in Eq. (1.80) does not exclude the overall anisotropy of the polaron. As explained in App. C, this function is just an envelope to a state in the valence or conduction bands (in case of a hole or electron polaron, respectively) describing its localization, cf. Eq. (C.4).

[8]The actual equations from Pekar were derived in real space. However, the real-space and the reciprocal-space derivations are simply related by the Fourier transformation of Eq. (1.79).

Using Eq. (1.80), for the binding energy one finds approximately:

$$E_{\text{bind}} = -0.1\alpha^2\hbar\omega_{\text{LO}}, \tag{1.81}$$

where the energy is minimized with the polaron radius:

$$r_{\text{p}} = 3.2\frac{1}{\alpha}\sqrt{\frac{\hbar}{2m^*\omega_{\text{LO}}}}. \tag{1.82}$$

This is consistent with physical intuition that the polaron radius should decrease with increasing el-ph coupling strength. But this also shows the limitations of the semi-empirical theory of Landau and Pekar. For MgO we obtain $r_{\text{p}} = 1.9$ Å, i.e., the radius of the polaron becomes comparable with the unit cell size and, thus, microscopic properties of the host crystal become important. Interestingly, the functional Eq. (1.79) gives a lower energy if a Gaussian trial function is used instead. However, as it is shown later by our DFT calculations this strong localization is physically incorrect if microscopic effects are considered, but the exponential decay of Eq. (1.80) turns out to be the proper long-range behavior [90, 29]. The polaron level E_0, i.e. the vertical transition energy of the charge carrier, can be obtained by solving just the "electronic part" of the Hamiltonian in Eq. (1.69) $\hat{H}_{\text{el}} = \hat{H}_{\text{kin,eff}} + \hat{H}_{\text{el-ph}}$. Then, the polaron level is an important quantity for optical effects in the solids, which can be related to luminescence and absorption bands.

Despite the inconsistencies between assumptions and the result in the strong-coupling limit, it can be used to explain substantial differences in the behavior of small and large polarons (cf. Fig. 1.8). While large polarons in case of weak el-ph coupling are delocalized over hundreds of atoms and floating like an effective-mass charge carrier, the small polarons are mainly localized around a certain atomic site, and their transport is characterized as hopping from one atomic site to another. This has consequences for the temperature dependence of the mobility and conductivity for the different polaron types as well: the large polaron's mobility is decreasing with increasing temperature, whereas for the small polaron it is the other way around.

Figure 1.9 shows a compilation of the polaron binding energies for different approximate solutions to the Fröhlich Hamiltonian. For Pekar's strong coupling limit, the second-order term

$$E_{\text{bind}}^{\text{Pekar}} = \left[-0.1\alpha_{\text{F}}^2 - 3\log 2 - 0.75\right]\hbar\omega_{\text{LO}}, \tag{1.83}$$

has been added, which is calculated, e.g., in Ref. [91] numerically. This second-order term is a constant and accounts for fluctuations of the polaron and non-adiabatic effects as it was discussed by several authors [87]. Also Feynman's all-coupling solution to the Fröhlich Hamiltonian [82] is shown in Fig. 1.9, in which the Hamiltonian is reformulated using path integrals to obtain approximate solutions as a function of α_{F}. For large values of α_{F} Pekar's and Feynman's solution coincide, underlining the consistency within the made approximations in the strong-coupling limit.

The solutions discussed above do not obey the symmetry of the host crystal due to our choice of the trial function Eq. (1.80). However, this can be easily fixed by summing over all equivalent sites with the following ansatz:

$$\Phi'_{\boldsymbol{k}}(\boldsymbol{r}, \boldsymbol{R}) = 1/N \sum_i \varphi(\boldsymbol{r} - \boldsymbol{R}_i)\chi(\boldsymbol{R} - \boldsymbol{R}_i)\mathrm{e}^{i\boldsymbol{k}\boldsymbol{R}_i} \tag{1.84}$$

with the number of equivalent sites in the Born-von Karman cell N. This form of the wave function allows the calculation of a polaron band and therefore the estimation of additional polaron properties such as the polaron mass and its band width. The procedure has been discussed by Tiablikov in 1952 and was used for KCl by Nettel [92] in a tight-binding framework. The detailed equations can be found in the review by Appel [87]. The resulting finite width of the polaron band due to the ansatz of Eq. (1.84) leads to ordinary band transport (coherent transport) for low temperatures. However, if the localization is rather strong, i.e., in the order of the nearest-neighbor distance, the overlap matrix elements become small and the band narrows. As a result, above a certain critical temperature the energy due to interactions with phonons is sufficient to activate the hopping and to break the symmetry – the narrower the polaron band, the lower the temperature is where hopping starts to get a noticeable conduction mechanism. Please follow Ref. [9] for a qualitative discussion. For the strong-coupling regime, which is considered in this work, the properties derived from the original ansatz Eq. (1.76) is sufficient to characterize the polaron physics and we will not discuss the polaron-band properties.

From polaron models to *ab initio* simulations

One of the important limitations of the discussed models is the macroscopic treatment of the lattice polarization. In the adiabatic approximation, this can be remedied by simulating the involved electrons quantum-mechanically, with the nuclei remaining classical point charges. In terms of a DFT calculation the polaron is a point defect in the host crystal, and for this task several approaches exist. First, the embedded-cluster approach is noteworthy, where a small cluster is embedded in (finite but huge) lattice of point charges representing the ions of the crystal. Due to the localized nature of the defect another embedding scheme [93, 94] can be used, where the atoms are divided into two sub-regions, A and B. Region A contains atoms close to the “defect” center and is treated self-consistently with a high-level quantum-mechanical method. Region B contains atoms far away from the center and is treated with lower-level methods, e.g. semi-empirical or force-field methods. Both regions are coupled using Green’s functions formalism. A great advantages of the method in Ref. [93] is that the energy contribution from geometry relaxations can be included from both regions, simulating the proper elastic response of the host crystal and the quantum-mechanical behavior close to the “defect” center. However, in this work we are using a much simpler approach, that is, the supercell approach.

In the supercell approach, a cluster is repeated periodically in each spatial direction in order to cover the entire space. Because of the periodic arrangements of the simulated defect, the calculated energies are not just that of an isolated defect, but

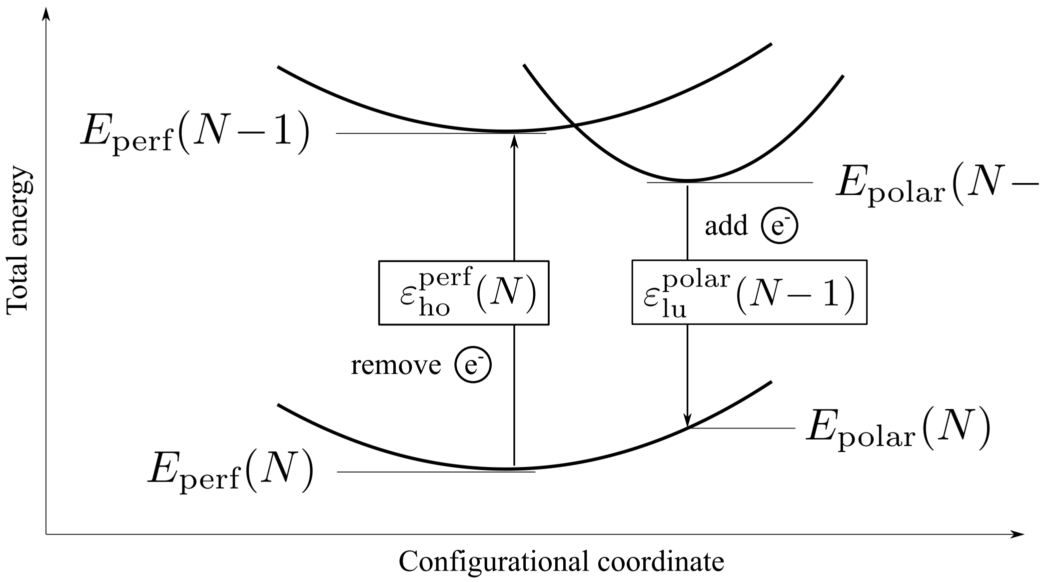

FIGURE 1.10: The PES of the perfect lattice configuration (left side) and the polaron configuration (right side) in different charge states. The PES is schematically indicated by parabolas.

that of an interacting defect lattice. For neutral system the interaction of neighboring defects decays quickly, and well-localized defects can be simulated nearly interaction-free in a moderately sized supercell. However, a charged defect such as a polaron leads to Coulomb interactions between neighboring defects and between defects and the compensating charge (necessary to avoid the divergence of the energy for an infinite periodic system with a charged unit cell). Consequently, the calculated total energies and forces become sensitive to the supercell size. Solving this problem is one of the main objectives of the second part of this work.

Using density functionals as implemented in the FHI-aims code in combination with the supercell approach allows s to simulate all electrons at the same (quantum-mechanical) level. In order to relate the polaron level and binding energy derived from the previously discussed models to DFT quantities (total energy differences and Kohn-Sham levels), we sketch the PES along the configurational coordinate towards the polaron geometry in Fig. 1.10. The total energy of the perfect neutral system $E_{\mathrm{perf}}(N)$ is obtained from the relaxed geometry of the pristine unit cell. Creating a supercell, keeping the perfect lattice geometry, and removing an electron (in case of the formation of a hole polaron; otherwise an electron has to be added) leads to the total energy of the perfect charged system with no localized distortions $E_{\mathrm{perf}}(N-1)$. According to the IP theorem Eq. (1.36), $E_{\mathrm{perf}}(N-1) - E_{\mathrm{perf}}(N) = -\varepsilon_{\mathrm{ho}}^{\mathrm{perf}}(N)$, where $\varepsilon_{\mathrm{ho}}^{\mathrm{perf}}(N)$ is the highest-occupied Kohn-Sham energy level for the neutral perfect-crystal geometry. The total energies and Kohn-Sham states at the polaron (distorted) geometry are labeled with "polar". With the equality $\varepsilon_{\mathrm{ho}}^{\mathrm{polar}}(N) = \varepsilon_{\mathrm{lu}}^{\mathrm{polar}}(N-1)$ (in general only valid for functionals, which are at least one-electron self-interaction free) the polaron level is given by:

$$E_0 = \varepsilon_{\text{ho}}^{\text{polar}}(N) - \varepsilon_{\text{ho}}^{\text{perf}}(N) \tag{1.85}$$

and the binding energy of the polaron is given as:

$$E_{\text{bind}}^{+} = E_{\text{polar}}(N-1) - E_{\text{perf}}(N-1). \tag{1.86}$$

This corresponds to electron removal (hole polaron). The analog for the electron addition (electron polaron) should be obvious:

$$E_{\text{bind}}^{-} = E_{\text{polar}}(N+1) - E_{\text{perf}}(N+1). \tag{1.87}$$

E_{polar} is the total energy of the distorted system (polaron geometry). The number of electrons in the system is given in parenthesis, with N corresponding always to the neutral system. A negative $E_{\text{bind}}^{\pm}$ indicates an energy gain and a stable (self-trapped) polaron. The above given derivation demonstrates how the polaron properties such as the binding energy and the level of the polaron can be calculated using DFT.

Chapter 2

Polarons and the DFT supercell approach

At the end of the previous chapter we discussed relevant polaron models for polar materials. However, the approximations made in these models are severe, especially for the small-polaron formation in case of strong el-ph coupling, when phonon modes of the entire BZ are contributing to the polaron binding energy, since a strong localization in real-space translates into delocalization in the k-space. The *ab initio* simulation of polarons in a supercell or in embedded cluster models using DFT provides a way to a parameter-free modeling in the adiabatic limit – an *ab initio* analogue of the Pekar's model, including accurate microscopic properties of the host crystal. A first attempt to simulate small polarons with an atomistic model was the study of Shluger *et al.* [95] using the semi-empirical quantum chemistry method INDO and applying it to a cluster of MgO embedded in an array of point charges. They found that the hole is not stable in bulk, but at the surface. However, considering the weak dispersion of oxygen bands (cf. App. E.3), the strong el-ph coupling with $\alpha_{\mathrm{F}} = 4.4$ in MgO, and the fact that the long-range medium response was not included, it can be expected that small polarons in the bulk are stable. Below we show that small hole polarons are indeed strongly bound and stable in MgO. The first-principles studies of small polarons are scarce due to the high required accuracy and the associated large computational cost. Only recently [96, 97] it became possible to compute sufficiently large supercells to correctly predict self-trapping in an otherwise pristine host crystal using more accurate but costly hybrid density functionals such as HSE06 [52, 53] or B3LYP [39, 54]. However, unsolved challenges remain associated with the DFT supercell approach, namely the dependence of polaron properties on the size of the supercell (i.e. the long-range screening by electrons and nuclei) and on the XC approximation. The following chapter investigates in detail and provides solutions to these issues.

2.1 Elastic long-range behavior

DFT in combination with the supercell approach has become the method of choice for the *ab inito* calculation of point defects in solids. However, the supercell approach suffers from finite-size effects, especially for charged defects. These finite-size effects include the interaction of the excess charge with its periodic images, with the compensating constant background charge introduced to keep the unit cell neutral, and with the periodic constraint on the atomic relaxation. To overcome these finite-size limitations, two strategies are commonly used: (a) extending the supercell and extrapolating to the dilute limit based on a scaling law, or (b) applying an *a posteriori* correction. For (a) only general knowledge about the size dependence is necessary. For example, the formation energy of a charged defect in the bulk as a function of the supercell size L ($L = \Omega^{1/3}$, where Ω is the supercell volume) can be written as an inverse powerlaw:

$$E(L) = E(\infty) + a_1 \frac{1}{L} + a_3 \frac{1}{L^3}, \tag{2.1}$$

where $E(\infty)$ is the formation energy in the dilute limit. This scaling law was derived by Makov and Payne [98], and the prefactors are given by:

$$a_1 = \frac{q^2 \alpha_{\mathrm{M}}}{2\varepsilon}, \tag{2.2}$$

$$a_3 = \frac{2\pi q}{3\varepsilon} \int_{\Omega} \mathrm{d}\boldsymbol{r} \rho_d(\boldsymbol{r}) r^2, \tag{2.3}$$

where q is the charge of the localized point defect, α_{M} the Madelung constant depending on the crystal structure, and ε is the linear response of the medium to an external electric field. If only the polarization of the electrons is considered, the response ε corresponds to the high-frequency dielectric constant ε_∞, or, if the response of both the electrons and ions is considered, it corresponds to the static dielectric constant ε_0. The latter is often referred to as the elastic response and is of great importance for our discussion on the long-range behavior of the polarons. Usually the terms a_1 and a_3 are not evaluated explicitly, but determined by fitting the energies of different supercell sizes. The disadvantage of this procedure is that at least three supercell calculations of increasing size are needed to estimate $E(\infty)$ in Eq. (2.1), which is computationally very demanding, especially if atomic relaxations are included.

Conversely, approach (b) requires an appropriate physical model for the long-range interactions in the solid. If only the electronic response to the excess charge is considered, its long-range contribution to the energy is described by a term proportional to $1/\varepsilon_\infty r$ (e.g. Ref. [99]). However, if the ionic response cannot be neglected, the problem becomes challenging, and so far this case has not been solved. It has been suggested that the long-range elastic contribution is similar to the electronic one, but with the high-frequency dielectric constant ε_∞ replaced by the static one ε_0, i.e., the long-range potential behaves classically like $1/\varepsilon_0 r$. However, corrections based on this assumption generally overestimate $E(\infty)$, in particular for vacancies [100]. This overestimation has two reasons. First, the aforementioned long-range behavior is a crude approximation, neglecting all details of the underlying phonon structure. Second, short-range screening can be much more efficient due to the strong coupling of the excess charge to localized phonon modes close to the defect and, thus, short-range screening will be different from $1/\varepsilon_0 r$. In the following we analyze the screening effects in detail and show that only in the strong-coupling limit of the el-ph interaction the substitution of ε_∞ with ε_0 is a good approximation.

We start by splitting the long-range elastic potential V^{lr} into the electron-phonon interaction $V^{\text{lr}}_{\text{el-ph}}$ and electrostatic potential $V^{\text{lr}}_{\text{el-st}}$:

$$V^{\text{lr}} = V^{\text{lr}}_{\text{el-st}} + V^{\text{lr}}_{\text{el-ph}} \,. \tag{2.4}$$

$V^{\text{lr}}_{\text{el-st}}$ is generated by the charge density $\rho_d(\boldsymbol{r})$ of the localized excess charge. The Fourier transform of $V^{\text{lr}}_{\text{el-st}}$ is then given by:

$$V^{\text{lr}}_{\text{el-st}}(\boldsymbol{k}) = 2\pi \frac{\rho_d(\boldsymbol{k})}{\boldsymbol{k}^T \boldsymbol{\varepsilon}_\infty \boldsymbol{k}} \,, \tag{2.5}$$

where $\rho_d(\boldsymbol{k})$ is the Fourier transform of $\rho_d(\boldsymbol{r})$.

To obtain a corresponding expression for $V^{\text{el-ph}}$ we first have to introduce additional assumptions. First, we will focus on polar crystals. Second, we only consider the interaction of an electron with a single phonon at a time, neglecting higher-order contributions[1]. Third, we assume that the adiabatic approximation (factorization of the electron and phonon wave functions) is applicable[2]. With these assumptions the long-range part of $V^{\text{el-ph}}$ reduces to [89]:

$$V^{\text{lr}}_{\text{el-ph}}(\boldsymbol{k}) = -\sum_\nu \frac{1}{\hbar\omega_{\boldsymbol{k}\nu}} \left| g^{\text{lr}}_{\text{el-ph}}(\boldsymbol{k}\nu) \right|^2 \rho_d(\boldsymbol{k}) \,, \tag{2.6}$$

which was derived earlier in this thesis, cf. Eqs. (1.76) – (1.78), but for now considering the general long-range el-ph matrix elements $g^{\text{lr}}_{\text{el-ph}}$. The potential in Eq. (2.6) is attractive, lending further stabilization to the polaron. An analytic expression for $g^{\text{lr}}_{\text{el-ph}}$ was recently derived by Verdi and Guistino [101]:

$$g^{\text{lr}}_{\text{el-ph}}(\boldsymbol{k}\nu) = i4\pi e \sum_\kappa \left(\frac{\hbar}{2NM_\kappa \omega_{\boldsymbol{k}\nu}} \right)^{1/2} \frac{\boldsymbol{k}^T \boldsymbol{Z}^*_\kappa \boldsymbol{e}_{\kappa\nu}(\boldsymbol{k})}{\boldsymbol{k}^T \boldsymbol{\varepsilon}_\infty \boldsymbol{k}} \tag{2.7}$$

where ν labels the phonon mode, $\omega_{\boldsymbol{k}\nu}$ is the corresponding phonon frequency of ion κ with mass M_κ. $\boldsymbol{Z}^*_\kappa$ is the Born effective charge tensor and $\boldsymbol{e}_{\kappa\nu}(\boldsymbol{k})$ are the phonon eigenvectors of the dynamical matrix.

[1] With this assumption we essentially limit the el-ph interactions to include only linear terms as for Eq. (1.76). This is in line with our goal to model the long-range part of the el-ph interactions, for which the displacements are small. The displacements can be large close to the center of the small polaron, but these short-range effects are simulated explicitly in the supercell.

[2] In the framework of classical DFT (i.e., the nuclei are considered as external potential) this is always fulfilled. However, non-adiabatic effects could alter the DFT results significantly.

Equations (2.6) and (2.7) describe the scattering of all phonon modes with ρ_d. Thus, the long-range behavior of the el-ph interaction depends on the phonon structure across the entire phonon Brillouin zone, and the elastic behavior is not captured by the classical $1/\varepsilon_0 r$ limit. If we only consider the interaction of ρ_d with a single dispersion-less longitudinal optical mode ω_{LO}, we recover the limit of the Fröhlich electron-phonon interaction in the strong-coupling limit, which was first investigated by Pekar [7]. With the Fröhlich matrix element (for the general case of an anisotropic medium [102]):

$$g^F(k) = ie\left[2\pi\hbar\omega_{LO}\left(\frac{1}{\boldsymbol{k}^T\boldsymbol{\varepsilon}_\infty\boldsymbol{k}} - \frac{1}{\boldsymbol{k}^T\boldsymbol{\varepsilon}_0\boldsymbol{k}}\right)\right]^{1/2} \tag{2.8}$$

we obtain the potential:

$$V^{\text{lr}}_{\text{el-ph}}(\boldsymbol{k}) = -2\pi\frac{\rho_d(\boldsymbol{k})}{\boldsymbol{k}^T\boldsymbol{\varepsilon}_\infty\boldsymbol{k}} + 2\pi\frac{\rho_d(\boldsymbol{k})}{\boldsymbol{k}^T\boldsymbol{\varepsilon}_0\boldsymbol{k}}\,, \tag{2.9}$$

where $\boldsymbol{\varepsilon}_\infty$ and $\boldsymbol{\varepsilon}_0$ are high-frequency and static dielectric tensors, respectively. Upon substituting Eq. (2.9) and Eq. (2.5) into Eq. (2.4), we finally arrive at the classical limit of a screened potential for a localized charge distribution in an anisotropic medium:

$$V^{\text{lr}}(\boldsymbol{k}) = 2\pi\frac{\rho_d(\boldsymbol{k})}{\boldsymbol{k}^T\boldsymbol{\varepsilon}_0\boldsymbol{k}}\,. \tag{2.10}$$

The el-ph potential given by Eq. (2.9) is an upper bound and, consequently, Eq. (2.10) is also an upper bound. This explains why any correction based on Eq. (2.10) overestimates the actual limit. We find that, despite the approximations we made, $V^{\text{lr}}(\boldsymbol{k})$ in Eq. (2.10) is still appropriate for polarons in the intermediate coupling regime ($1 \lesssim \alpha_{\text{F}} \lesssim 5$). Vice versa, our derivation can be used to improve the long-range model for polarons and charged point defects, if needed, since all assumptions are clearly defined.

Based on the knowledge of the long-range behavior, the errors due to finite size of the supercell can be corrected using *a posteriori* methods, such as the method of Freysoldt *et al.* [99, 103]. Generalizing the Freysoldt method to an arbitrary interaction potential $V(\boldsymbol{r})$ and anisotropic media (in the standard approach of Freysoldt *et al.*, $V(\boldsymbol{r}) \sim 1/\varepsilon_\infty r$), the correction for the interaction energy is obtained as the difference between the energy of the artificial lattice of charged defects, E_{latt}, and the energy of an isolated defect, E_{iso}:

$$\begin{aligned} E_{\text{corr}}(\Omega) \quad &= E_{\text{latt}}(\Omega) - E_{\text{iso}} \\ &= \frac{1}{\Omega}\sum_{\mathbf{G}\neq\mathbf{0}} V(\boldsymbol{G})q_d(\boldsymbol{G}) - \frac{1}{(2\pi)^3}\int V(\boldsymbol{k})q_d(\boldsymbol{k})\mathrm{d}\boldsymbol{k}\;, \end{aligned} \tag{2.11}$$

where V can be $V^{\text{lr}}_{\text{el-ph}}$, $V^{\text{lr}}_{\text{el-st}}$ or the sum of both, and $q_d(\boldsymbol{k})$ is the Fourier transform of the excess charge distribution, Σ is the volume of the supercell. The first term $E_{\text{latt}}(\Omega)$ is a sum over all reciprocal lattice vectors $\boldsymbol{G}$ omitting the divergent contribution at $\boldsymbol{G} = 0$. Taking into account the alignment term $q\Delta V$ [99, 103], where q is the total charge per supercell, the corrected energy $E(\infty)$ is obtained as:

$$E(\infty) = E(\Omega) - E_{\text{corr}}(\Omega) + q\Delta V \tag{2.12}$$

for the energy $E(\Omega)$ calculated in the supercell with volume Ω. A summary of the Freysoldt *et al.* correction scheme including the meaning of the alignment term can be found in the App. B. Having derived the correction for the elastic contribution, we can apply it to the polaron problem and investigate the effects of the two parts in Eq. (2.4) separately.

2.2 The polaron in a supercell

In the following subsections, two ways of obtaining optimized polaron geometry, the polaron binding energy, and the polaron level are presented. The conventional way is presented first, i.e., where the polaron geometry and ensuing properties are simulated in an explicitly charged supercell. In the second approach only the neutral supercell is needed. In this approach, the atomic positions are allowed to relax according to the polaron charge distribution, but without having introduced a charge explicitly. The forces needed for the optimization are obtained by calculating gradients of a modified potential-energy surface. At the end of this chapter we formulate our approach to calculating polarons, which minimizes the influence of the errors due to the XC functional approximations and the finite-size effects.

2.2.1 The charged supercell

An important property of a polaron is its binding energy as we have introduced in Eq. (1.86) with

$$E^{\pm}_{\text{bind}} = E^{\text{polaron}}(N \mp 1) - E^{\text{perf}}(N \mp 1)$$

where the energies have not been corrected for finite-size effects, yet. The simplest way to calculate the polaron binding energy is straightforward: in Eq. (1.86) $E^{\text{polaron}}(N \mp 1)$ is computed with DFT and full structure relaxation in the charged supercell. To ease the system out of possible high symmetry configurations, an initial symmetry-breaking distortion have to be applied. Finite-size effects are expected to be small, since the elastic long-range interaction falls off with $1/\varepsilon_0 r$ and the static dielectric constant ε_0 is usually large ($\gtrsim$10) for ionic crystals (however, as demonstrated and explained below, the dependence of the polaron binding energy defined by Eq. (1.86) on the approximations in the exchange-correlation functional is strong).

In the following, we focus on the hole polaron for brevity, since only small adjustments of the formalism are needed for the electron polaron case. The supercell dependence of E^{+}_{bind} for MgO is shown in Fig. 2.1, panel a, where we used HSE06 hybrid functional [52, 53] with the fraction of exact exchange $\alpha = 1$ [denoted HSE($\alpha = 1$); see Section 2.2.2 for more computational details]. We find a small hole polaron mainly localized at the central oxygen atom. The displacements of the nearest neighbors are of the order of 0.1 Å and decaying fast away from the center[3]; cf. App. E.3 for further details of the behavior of the displacements and their dependence on the supercell size. The shape of the excess charge density distribution is p-like (cf. Fig. 2.4). For sufficiently large supercells in Fig. 2.1, when the long-range regime is valid, the dependence of the binding energy on the supercell size L becomes $1/\varepsilon_0 L$. From the slope of $E^{+}_{\text{bind}}(1/L)$ at $1/L = 0$ we obtain $\varepsilon_0 = 10.32$, in good agreement with the experimental static dielectric constant for MgO $\varepsilon_0 = 9.8$.

[3]However, the contribution of the displacements to the polaron energy is not decaying fast as it is demonstrated below.

Next, we calculate the correction for the artificial electrostatic interaction due to the periodic arrangement of the holes and their interaction with the constant background, using Eq. (2.11) with the potential Eq. (2.5) (that is $\sim 1/\varepsilon_\infty r$). To model the excess charge density $\rho_d(\boldsymbol{r})$ needed here and for following finite-size corrections, we fit the envelope of the KS eigenstate density (decays exponentially for a localized state) with an exponential function:

$$\rho_{\text{model}} = A \exp(-|r - r_0|/\gamma), \tag{2.13}$$

where A is a normalization constant, r_0 is the center of the polaron, and γ the fitting parameter corresponding to the polaron radius (cf. Sec. C for more details). Additionally, we calculated the alignment term ΔV in Eq. (2.12) between the charged, neutral, and model (i.e., including the model excess charge density compensated by a constant background charge) systems following the approach outlined in Ref. [103]. After this correction, according to Eq. (2.4) the remaining contribution is due to the long-range electron-phonon interaction. This contribution is shown by the blue line in Fig. 2.1, panel a. The line is almost perfectly straight, and the slope is equal to $(\varepsilon_\infty^{-1} - \varepsilon_0^{-1})q^2\alpha_{\text{M}}/2$, where $\varepsilon_0 = 10.32$ is taken from the fit of E^{+}_{bind} introduced above, and $\varepsilon_\infty = 2.4$ is obtained from an independent calculation[4]. This analysis reveals the role of different long-range interactions in Eq. (2.4) in the supercell dependence of polaron properties.

Thus, the approximations in Eq. (2.9) work well for MgO, which is expected since it has only one longitudinal optical phonon mode, strong el-ph coupling, and is an isotropic material. However, we find that the polaron binding energy defined by Eq. (1.86) is extremely sensitive to the approximations in the exchange-correlation functional. Figure 2.1, panel b, shows the dependence of the binding energy on the fraction of exact exchange α in the HSE06 functional. Within a small range ± 0.05 of α around the standard value (0.25) the binding energy changes by about 0.5 eV, which is in the order of the change of the band gap (6.1 eV for α=0.2 and 6.8 eV for α=0.3, cf. Fig. 2.5). This leads to a qualitative change in small polaron stability, from a stable self-trapped polaron (negative binding energy) to an unstable small polaron (positive binding energy). This strong functional dependence makes even a qualitative assessment of the existence of self-trapped polarons impossible. Several approaches have been suggested in the literature for determining the correct or at least optimal value of α [45, 46, 104, 50, 105, 106, 107]. Here we focus on *restoring the IP theorem* [104] as a consistent *DFT-based* solution of the problem.

In (exact) DFT within the scope of Kohn-Sham (KS) scheme the vertical ionization potential IP should be equal to the negative of the highest occupied KS state energy ϵ_{ho} in the system:

$$IP = E(N-1) - E(N) = -\epsilon_{\text{ho}}(N)\,, \tag{2.14}$$

[4]The dielectric constant ε_∞ was obtained by fitting unrelaxed singly positively charged oxygen vacancy's formation energy for MgO as a function of the supercell size, using the Eq. (2.1). See App. D.2 for details. This approach of calculating the dielectric constant with non-local functionals implicitly includes local field effects, as is also shown in App. D.2.

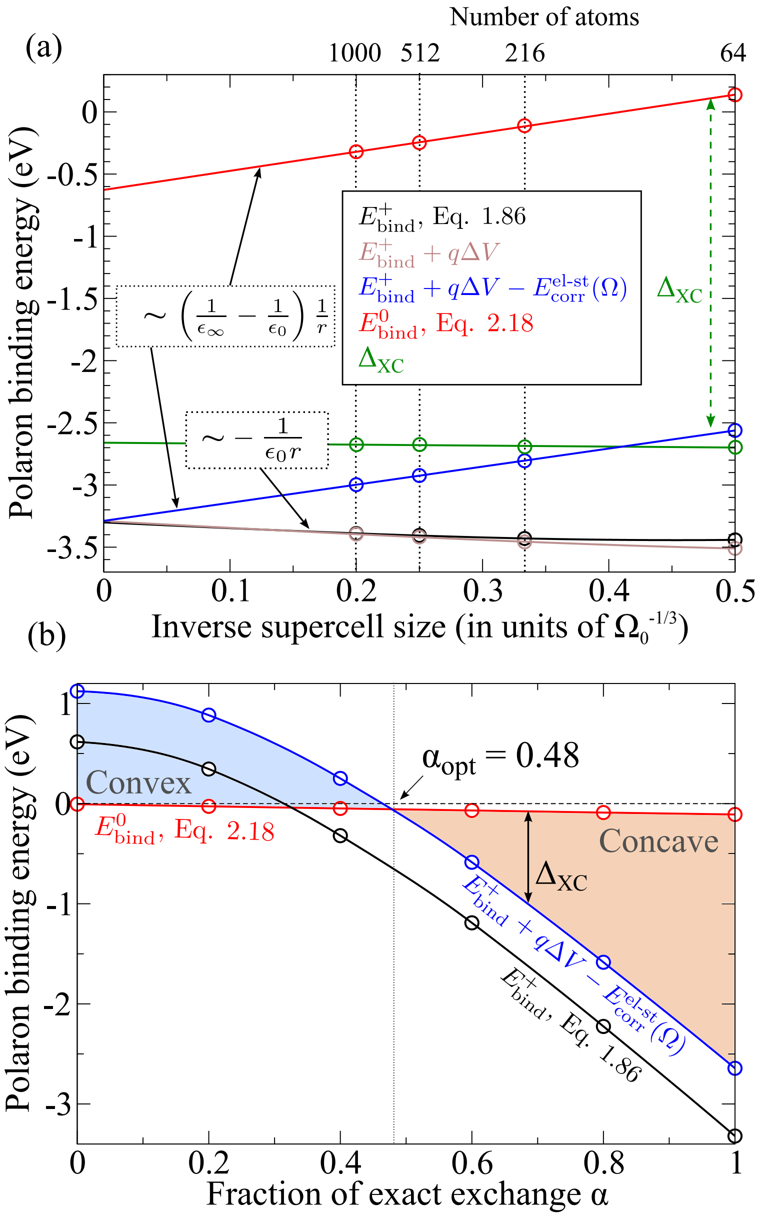

FIGURE 2.1: (a) The supercell dependence of the hole polaron binding energy including different corrections and definitions, calculated for MgO with HSE06(α=1). The black and red lines are the binding energies as defined by Eqs. (1.86) and (2.18), respectively. The term $q\Delta V$ corresponds to the potential alignment explained for Eq. (2.12). The blue line includes the correction for the polarization of the electrons $E^{\mathrm{el\text{-}st}}_{\mathrm{corr}}(\Omega)$ and the potential alignment term. The difference between the red and blue lines corresponds to the green line, the XC error due to the deviation from the straight-line behavior Δ_{XC}. The atomic positions are fully relaxed for each supercell size. (b) Dependence of the polaron binding energies on the fraction of exact exchange. The fixed geometry of the $3 \times 3 \times 3$ supercell from panel (a) is used and binding energies for different fractions of exact exchange are calculated.

where $E(N-1)$ and $E(N)$ are total energies of the ionized and neutral system, respectively. In this work we refer to this relation as IP-theorem, but it is also known as HOMO-I condition [45] or generalized Koopmans' theorem [104], and is directly related to the straight-line dependence of the total energy on occupation of the highest-occupied state [26] or the fact that the position of ϵ_{ho} is independent on its occupation. Equation (2.14) is always correct for any extended (delocalized) state, as was already pointed out by Janak (1978) and extended to the case of the generalized KS scheme by Perdew *et al.* [33]. However, for a given density-functional approximation (DFA), Eq. (2.14) does not necessarily hold if the orbital is localized, unless the satisfaction of the straight-line condition is explicitly included in the design of the functional. The deviation from the straight line $\Delta_{\mathrm{XC}}(\alpha)$:

$$E(N-1) - E(N) = -\epsilon_{\mathrm{ho}}(N) + \Delta_{\mathrm{XC}}(\alpha) \tag{2.15}$$

is described by two contributions to Eq. 2.14, $\Delta_{\mathrm{XC}} = \Pi + \Sigma$, with the self-interaction error Π causing a convex curvature of the total energy as a function of occupation, and the orbital relaxation Σ a concave curvature. The optimal $\alpha = \alpha_{\mathrm{opt}}$ minimizing the XC error [46, 44] is then determined from the condition $\Delta_{\mathrm{XC}}(\alpha_{\mathrm{opt}}) = 0$.

The straight-line theorem (Eq. (2.14)) was originally proven for finite systems, and transferring it to a solid with periodic boundary conditions needs special care. For any finite supercell with volume Ω, the energy of the artificial electrostatic interactions due to the periodic arrangement [$E^{\text{el-st}}_{\mathrm{corr}}(\Omega)$, obtained using Eq. (2.11) with potential from Eq. (2.5)], has to be removed from $E(N-1)$:

$$E(N-1) - E^{\text{el-st}}_{\mathrm{corr}}(\Omega) - E(N) = -\epsilon_{\mathrm{ho}}(N) + \Delta_{\mathrm{XC}}(\alpha)\,, \tag{2.16}$$

since it would only vanish in the limit of an infinite supercell. Combining Eq. (2.16) and Eq. (1.86), we get:

$$E^{+}_{\mathrm{bind}} = E^{0}_{\mathrm{bind}} + E^{\text{el-st}}_{\mathrm{corr}} + \Delta_{\mathrm{XC}}(\alpha)\,, \tag{2.17}$$

where $E^{\text{el-st}}_{\mathrm{corr}}$ stands for the artificial electrostatic interaction energy for the distorted geometry (since for the perfect geometry this contribution vanishes) and the quantity

$$E^{0}_{\mathrm{bind}} = \Delta E^{\mathrm{polaron}} - E_0 \tag{2.18}$$

is calculated using only *neutral* unit cells, with the energy of distortion from perfect to polaronic geometry $\Delta E^{\mathrm{polaron}} = E^{\mathrm{polaron}}(N) - E^{\mathrm{perf}}(N)$ and the polaron level energy with respect to the VBM $E_0 = \epsilon^{\mathrm{polaron}}_{\mathrm{ho}}(N) - \epsilon^{\mathrm{perf}}_{\mathrm{VBM}}(N)$. According to Eq. (2.17), when $\Delta_{\mathrm{XC}}(\alpha)$ is zero, E^{0}_{bind} represents the polaron binding energy corrected for the artificial electrostatic interaction.

E^{0}_{bind} is shown in Fig. 2.1, panel a, as red line (top-most line), where the optimized polaron geometry of the charged supercell is used. Note that, despite including only quantities calculated using neutral unit cells, E^{0}_{bind} has a strong dependence on the supercell size. As discussed below, this dependence is due to the interaction of the ionic relaxations in different unit cells. According to Eq. (2.17), the difference between

E^0_{bind} and E^+_{bind} corrected for the electrostatic supercell interactions (the blue line in Fig. 2.1, panel a) is the XC error for a given supercell size. We find that the XC error Δ_{XC} is practically independent on the unit cell size (green line in Fig. 2.1, panel a), starting from the smallest supercell with 64 atoms we have considered. This implies that $\Delta_{\text{XC}}(\alpha)$ could be calculated even in the smallest supercell and then removed in any larger supercell. In order to obtain the optimized $\alpha = \alpha_{\text{opt}}$ we have to remove $E_{\text{el-st}}(\Omega)$ from the binding energy E^+_{bind} and determine the intersection with E^0_{bind}. The result is shown in Fig. 2.1, panel b, and we obtain $\alpha_{\text{opt}} = 0.48$. Since the dependence on α is not linear, at least three different values of α have to be calculated to estimate α_{opt}. Additionally for each value of α the dielectric constant ε_∞ has to be calculated. Thus, the simulation of the polaron in a charged supercell is computationally demanding, since it is extremely sensitive to the underlying functional. In the next subsection we demonstrate an approach to overcome this problem.

2.2.2 The neutral supercell

As mentioned above, E^0_{bind} in Eq. (2.17) is equal to the polaron binding energy corrected for the artificial electrostatic interaction, only when $\Delta_{\text{XC}}(\alpha)$ vanishes. However, similar to previous work [108, 109], we find that E^0_{bind} is far less sensitive to the underlying functional than E^+_{bind}, as can be seen for MgO in Fig. 2.1, panel b. The same is true for TiO_2, but the remainig dependence is larger than for MgO (see Fig. 2.3). This has an interesting implication: E^0_{bind} is the polaron binding energy with most of the exchange-correlation error removed (because for an exact functional E^0_{bind} is equal to the polaron binding energy). The reason for the insensitivity of E^0_{bind} on the functional remains unclear, but might benefit from the closed-shell character of the system [108].

As a consequence, even with PBE we find a stable self-trapped hole polaron in MgO, which is not the case when charged supercells are used. Also, we find that the polaron level with respect to the band edge (E_0), calculated using a neutral supercell, is insensitive to the functional, as can be seen in Fig. 2.5. A stronger functional dependence of E_0 is expected when the character of the polaronic state or states of the band edges are sensitive to the functional.

Polaron geometry optimization in the neutral cell (approach by Sadigh *et al.*)

Using E^0_{bind} for calculating polaron binidng energies has been first implicitly introduced by Zawadski *et al.* [109]. The independence of E^0_{bind} on the functional has been discussed by Sadigh *et al.* [108]. In their work, Sadigh *et al.* have also suggested a way to obtain forces for a polaronic distortion directly using E^0_{bind} PES. This facilitates the calculation of accurate elastic response to the excess charge at the level of a hybrid functional, but at the cost of a PBE calculation. Their approach to calculate the forces from the neutral PES is shortly introduced in this paragraph.

In general, the force on the *i*th atom is given by the gradient of the energy with respect to its position:

$$F_i(N-1) = \nabla_i \left(E(N) - \epsilon_{ho}(N)\right), \tag{2.19}$$

where we already have substituted $E(N-1)$ with $E(N) - \epsilon_{ho}(N)$ from Eq. (1.36). The first term is just the force obtained from the neutral PES. For the second term we apply Janak's theorem $\epsilon_{ho} = dE(N)/dN$ (cf. Fig. 2.2 for the following numerical approximations):

$$\begin{aligned} F_i(N-1) =& F_i(N) - \nabla_i \left(\frac{dE(N)}{dN}\right) && (2.20)\\ =& F_i(N) - \frac{d}{dN}(\nabla_i E(N)) = F_i(N) - \frac{dF_i(N)}{dN} && (2.21)\\ \approx& F_i(N) - \Delta_\delta \left[F\right](N), && (2.22) \end{aligned}$$

where $\Delta_\delta [F](N)$ is the backward finite difference approximation of the derivative, e.g. in first order:

$$\Delta_\delta [F](N) = \frac{F(N) - F(N-\delta)}{\delta} \tag{2.23}$$

With this approximation, we can calculate the forces $F_i(N-1)$ from the forces $F_i(N)$ in the neutral cell and the forces $F_i(N-\delta)$ in a slightly charged cell (with a fraction δ of an electron removed). Since δ is small, the error due to the artificial charged supercell interactions is also small. For our calculations, we used a second-order approximation of the backward finite differences, analogous to the approach suggested by Sadigh *et al.* [108]. The forces are calculated directly with FHI-aims, whereas the geometry optimization is performed using the *Atomic Simulation Environment* package [110] to calculate $\Delta_\delta [F](N)$ in Eq.(2.23). The parameter h is set to 0.0025 (as proposed in [108]) giving a deviation to true $\epsilon_{ho/lu}$ smaller than 0.01 eV. Forces have been considered converged as soon as they were smaller than 0.001 eV/Å. For all our geometry relaxations we see a stable but slow convergence below this limit. Furthermore, for this geometry optimization we used the PBE functional, which is sufficient to get the right atomic positions as we show in the App. E comparing the different functionals and methods. Applying this optimization method to MgO, we find a self-trapped hole polaron in MgO on the E^0_{bind} PES with PBE as before on the E^+_{bind} PES with HSE(α=1). However, a stronger dependence of the polaron properties on the supercell size is observed, which can be corrected by the approach presented next.

A posteriori finite-size correction in the neutral cell

Using the E^0_{bind} PES instead of charged supercells allows us to significantly reduce the functional dependence. Naively, one may expect that the supercell dependence is also reduced, since only neutral supercell calculations are performed. However, this is not

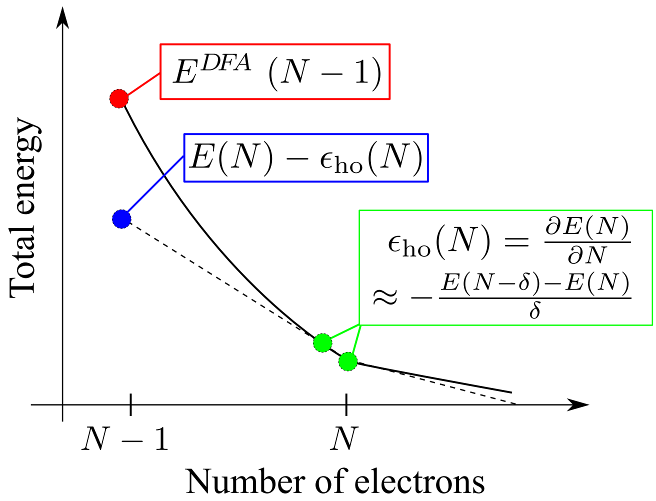

FIGURE 2.2: The numerical evaluation of the ho KS state using Janak's theorem. The red point indicates the total energy of a SCF calculation of the charged system, the blue point represents the same energy estimated by using the IP theorem. The difference appears due to the violation of the IP theorem. The green points and the corresponding text box represent the finite difference approximation of the energy derivative.

the case. As can be seen from Fig. 2.1, panel a, the dependence of E^0_{bind} on the supercell size is much stronger than in the case of charged suercells. This dependence is due to the artificial interaction between ionic relaxation fields in different supercells. Indeed, the $E^+_{\text{bind}} - E^{\text{el-st}}_{\text{corr}}$ and E^0_{bind} supercell dependence are practically identical and correspond to the long-range part of the electron-phonon interaction potential given by Eq. (2.9) in the strong el-ph coupling limit. This understanding allows us to introduce an *a posteriori* correction $E^{\text{el-ph}}_{\text{corr}}$ calculated using Eq. (2.11) with $V = V^{\text{lr}}_{\text{el-ph}}$ of Eq. (2.9), which removes the dependence of E^0_{bind} on the supercell size. To remove the artificial interaction terms, we use the approach of Freysoldt *et al.* [99, 103] Eq. (2.11), but for a different long-range potential, namely the one given by Eq. (2.9). Note that the original approach by Freysoldt *et al.* was developed for electronic response effects, while we use the general scheme to treat nuclear distortions as well. This new correction scheme relies on the adiabatic approach, which is usually applicable for strong el-ph coupling, but, as will be demonstrated below, works reasonably well also for intermediate coupling regimes.

The polaron level E_0 also depends on the supercell size. Because of special properties of the small polaron in the adiabatic strong-coupling limit, it is possible to relate the polaron binding energy to the polaron level, in accordance with Pekar's 1:2:3:4 theorem [111] . It follows from the theorem that (see details in App. C.1):

$$E_0(\infty) = E_0(\Omega) + 2 \cdot E^{\text{el-ph}}_{\text{corr}}(\Omega)\,, \tag{2.24}$$

where $E_0(\Omega)$ denotes the polaron level calculated in a supercell with volume Ω. Thus, the correction to $E_0(\Omega)$ in a finite supercell is expected to be about twice as large as for the polaron binding energy calculated using neutral supercells. Indeed, this is what we observe for MgO (see Fig. 2.3, panel a), where the absolute value of the E_0 slope as a function of $L = \Omega^{-1/3}$ is almost exactly twice of the absolute value of the E^0_{bind} slope. For TiO_2, the relation between the E_0 and E^0_{bind} dependencies deviates from the one derived from Pekar's 1:2:3:4 theorem (see Fig. 2.3, panel b) due to a weaker electron-phonon coupling, as discussed in detail in the next Section 2.2.2.

The new approach for simulating small polarons using DFT

In summary, we find that the dependence on the exchange-correlation approximation is drastically reduced by transforming the treatment from a charged to a neutral supercell. However, the finite-size effects are significantly more pronounced. These effects, caused by the electron-phonon long-range potential (eq. (2.9)), can be corrected using the general scheme of Freysoldt *et al.*, but with the potential $V^{\text{lr}}_{\text{el-ph}}$ derived in the previous chapter of this thesis. This makes possible using moderately sized supercells and semi-local functionals to predict polaron properties as it will be demonstrated more clearly in the remaining part of this chapter (especially cf. Fig. 2.3). Building on the findings and understanding obtained in the previous sections, we formulate an approach for a reliable calculation of polaron properties in the adiabatic approximation:

1. We obtain the atomic structure of the polaron using the PBE functional [corresponding to HSE06(α=0)], where the forces for the atomic relaxation are evaluated according to the approach of Sadigh *et al.* [108], namely the evaluation of Eq. (2.20).

2. HSE06(α=1) calculations (as a limiting case) are performed for the fixed geometries obtained with PBE. This allows the estimation of the results on the XC functional.

3. The polaron binding energies are calculated using Eq. (2.17). The finite-size correction for the binding energy is calculated using Eq. (2.11) with the potential from Eq. (2.9). The correction for the polaron level is calculated as twice the correction for the binding energy. The polaron radius needed for the finite size correction is estimated by fitting the envelop of the excess-charge density as described in App. C.

The different sign of the correction for the hole polaron versus the electron polaron (compare panels a and b in Fig. 2.3) is explained by the fact that the equation for the electron affinity has to be used for the electron instead of the ionization potential for the hole.

The approach described above is applied for the simulation of a hole polaron in MgO and an electron polaron in rutile TiO_2. The results are shown in Fig. 2.3. We use the hybrid-functional implementation [70] in the all-electron full-potential electronic-structure package FHI-aims [59, 60, 69]. The evaluation of forces and total energies are computed with FHI-aims using the default *light* settings, to obtain consistent results for all unit cell sizes. As is shown in the App. E, using default *tight* settings, which

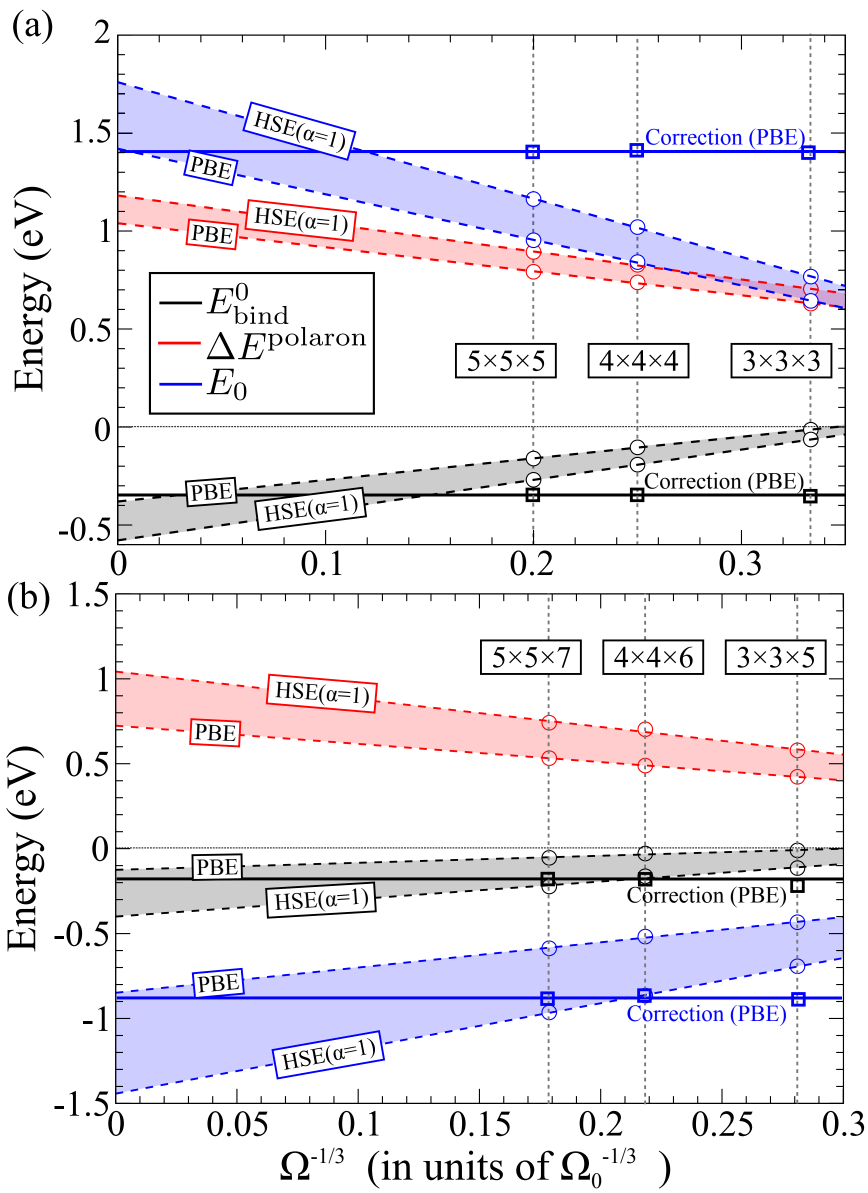

FIGURE 2.3: The polaron binding energy $E^0_{\rm bind}$ (Eq. 2.18), the polaron KS level E_0 with respect to band edge, and the relaxation energy $\Delta E^{\rm polaron}$ for (a) MgO and (b) rutile TiO_2 as a function of the inverse supercell size $\Omega^{-1/3}$. The x axis is given in units of the cubic root of the unit cell volume Ω_0. The PBE polaron binding energies corrected for the finite-size effects are shown by square symbols. The solid lines show linear least-squares fit for different energy components and DFT approximations. For all supercells the atoms are relaxed according to the approach described in the text.

are the recommended settings for well-converged calculations, does not change the results for the smallest supercell. For the cubic 8-atom MgO unit cell we use a lattice constant of $a = 4.211$ Å obtained with HSE06 (α=0.25), and a Γ-centered $8\times8\times8$ k-grid. The number of k-points for each direction is scaled down linearly for larger supercell sizes. For the tetragonal 6-atom TiO_2 unit cell we use $a = 4.64$ Å and $c = 2.97$ Å obtained with the PBE functional and a $9 \times 9 \times 15$ k-grid. Due to one more degree of freedom the positions of the atoms are optimized, too, using the PBE functional (for details see Sec. 3.1). For every supercell size we allow all atoms to relax to obtain the full elastic contribution within the cell. The corrected E^0_{bind} values for each supercell are shown for PBE.

Clearly, the supercell-size dependence of E^0_{bind} for both MgO and TiO_2 agrees very well with the behavior corresponding to the electron-phonon long-range contribution described by Eq. (2.9). As mentioned above, the Fröhlich coupling constant α_{F} is equal to 4.4 for MgO and 2.2 for TiO_2. Thus, MgO is better described with Pekar's long-range el-ph potential Eq. (2.9), and the size-corrected binding energy practically coincides with the binding energy obtained from a linear extrapolation to the dilute limit. The polaron radii of MgO and TiO_2 needed for our finite-size correction are shown in Fig. 2.4. The sensitivity of the polaron radius to the XC approximations has been investigated for MgO for different fractions of exact exchange, too, and we find only a weak XC functional dependence (cf. Fig. E.2). For TiO_2, the corrected energy deviates (surprisingly only slightly) from the extrapolated one (within 0.05 eV), reflecting approximations in Pekar's long-range el-ph potential, since four LO modes exist in rutile TiO_2 and can interact with the excess charges. Also, the dependence of the binding energy and polaron level on the XC functional is stronger for TiO_2 and additionally, we observe that the atomic structure of the pristine unit cell is sensitive to the XC functional as well (cf. F.1 for details) demonstrating limitations of obtaining polaron properties with only the PBE functional. However, the changes in the geometry as a function of α are still small, and we use the configurations of the systems obtained with PBE. We find final polaron binding energies in the dilute limit -0.38. . . -0.58 eV for MgO and -0.14. . . -0.41 eV for TiO_2, where the range indicates changes in α from 0 to 1. For the polaron level with respect to the band edge we find 1.42. . . 1.74 eV for MgO and -0.86. . . -1.44 eV for TiO_2. These results remain both qualitatively and quantitatively consistent across a broad range of functionals generated by varying the fraction of exact exchange. This consistency is remarkable when compared to previous theoretical studies, especially for TiO_2, since it was either shown that the small polaron formation is expected only for a certain range of a parameter, e.g. for DFT+U [112, 113] or HSE(α) [114], or it was demonstrated only for a specific value of a parameter, e.g. for HSE(α=0.25) [115].

To make a connection to experimentally accessible quantities, in particular photoluminescence (PL) measurements, an accurate prediction of polaron level is important. Since the quantities obtained with the neutral PES E^0_{bind} are weakly dependent on the underlying functional, the fraction of exact exchange α can be used to tune the gap E_{gap} to recover the experimental band gap, which ensures a good estimation of the absolute position of the polaron level w.r.t. band edges. Then, the main PL peak due

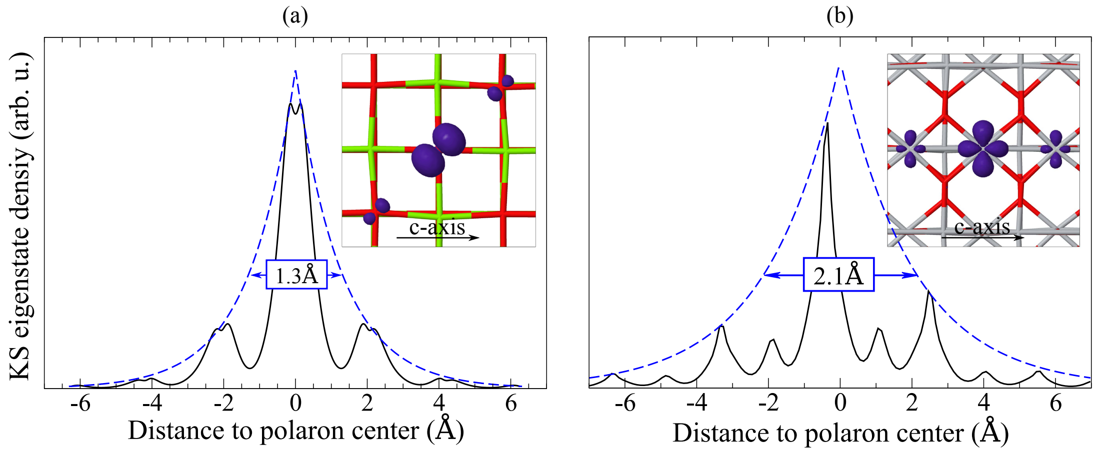

FIGURE 2.4: The Kohn-Sham eigenstate densities (black solid lines) along the c-axis for (a) the hole polaron in MgO and (b) the electron polaron in TiO_2. The blue dashed lines represent the envelope $\rho_d(\boldsymbol{r})$ of the densities. The obtained polaron radius is 1.3 Å and 2.1 Å for MgO and TiO_2, respectively. For details see C. The isosurfaces shown in the insets encompass 0.95% of the polaron density. Red nodes represent oxygen, green – magnesium, and silver – titanium atoms. The geometries are optimized with the Sadigh *et al.* approach [108] using the PBE functional. The center of the polaron emerges automatically from the fitting of Eq. (2.13).

to the small polaron formation can be expected at:

$$PL = E_{\mathrm{gap}} - |E_0| \,. \tag{2.25}$$

For MgO, the experimental band gap was measured as 7.8-7.9 eV [10], which is obtainedin our DFT-HSE calculation for $\alpha = 0.4$. Based on our HSE06($\alpha = 0.4$) calculations, the PL peak should be at 6.3 ± 0.1eV. Unfortunately, we could not find any experimental reference for this region of PL. There are PL bands at 7.65 for 6.9 eV assigned to free and self-trapped excitons, respectively [116]. The high intensity of the PL suggests that it is an intrinsic property of MgO. The difference to our theoretical prediction could have many reasons: we are not explicitly considering an exciton in our simulation, nor do we include any temperature or non-adiabatic effects. Additionally, we have not used the optimized lattice constant for HSE(α=0.4). For rutile TiO_2 a fraction $\alpha = 0.2$ is needed in order to reproduce the experimental band gap of 3.1 eV [117], and the corresponding photoluminescence peak is predicted by our calculation to be at 2.1 ± 0.1 eV. This is in good agreement with experimental findings of $PL = 2.34$ eV for rutile powders [118] and direct measurements of the polaron level $E_0 = 0.7 \pm 0.1$ eV corresponding to $PL = 2.4$ eV with scanning tunneling spectroscopy [112]. We note that the results provided here only represent an upper limit for the polaron level or lower limit for the PL peak, since neither finite-temperature nor non-adiabatic effects are taken into account.

In summary we could demonstrate that our approach leads to a robust qualitative prediction and description of small polarons and allows an estimation of the influence

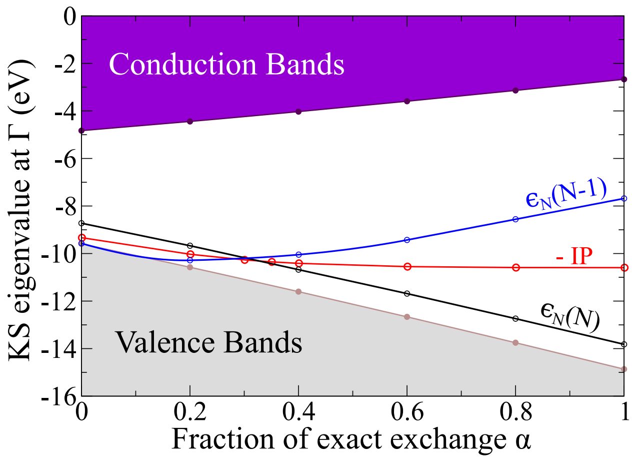

FIGURE 2.5: The dependence of the hole-polaron level calculated in the charged (blue line) and in the neutral (black line) $3 \times 3 \times 3$ supercell of MgO. The negative $IP = E(N-1) - E(N)$ of the systems is given by the red line. N corresponds to the number of electrons in the neutral system. Clearly, the black line tracks the VBM for the entire range of α, and therefore gives a better description of the polaron level than in the explicitly charged system. The energies are calculated for a fixed geometry, where the geometry has been optimized with the approach by Sadigh *et al.* and the PBE functional.

of the XC approximation. The quantitative values of the polaron binding energies is drastically reduced by our approach compared to the previous, conventional approach (cf. Fig. 2.1, panel b (black line)), where charged supercells are used. However, at this point we have to admit that the actual reasons for this advantageous behavior is not fully understood. One might argue that the neutral supercell is a closed-shell system, i.e., all states are doubly occupied, and the empirically established rule is that the KS potentials of closed-shell systems are sufficiently accurate for many properties, as we have demonstrated for the band gap of several oxides (cf. Fig. 1.4). This is confirmed by the analysis of the dependence of the polaron level on the fraction of exact exchange α calculated in either the charged or the neutral supercell and shown in Fig. 2.5. The position of the level calculated in a charged supercell changes from deep in the gap for α=1 to delocalized at the VBM for α<0.2. Moreover, compared to the IP = $E(N-1) - E(N)$ at the polaron geometry, $\epsilon_N(N-1)$ is twice as strongly affected by the XC functional. On the other hand, as shown in Fig. 2.5, we find that the polaron state in the neutral system $\epsilon_N(N)$ perfectly tracks the VBM of the pristine system. This explains why the dependence on the XC approximations is weaker for the binding energy calculated using the Eq. (2.17). Clearly, the character of the polaron is bound to the character of the VBM state. This explains the similar changes of their levels as a function of α (Fig. 2.5) in the neutral system.

2.3 The adiabatic PES of the polaron

The optimized polaron geometry represents a single point on the adiabatic PES of the charged system, and hence provides little information about the dynamics of the polaron. Therefore, it is of great interest to explore the PES in the vicinity of the undistorted and the minimum-energy polaron configurations, and paths connecting them. For a rough estimate (and an upper bound) of the barriers along those paths we interpolate linearly between different configurations, as described below. There are several paths of particular importance for understanding the formation and migration of polarons: (1) the transition from the pristine to the polaron configuration, (2) transfer to nearest-neighbor atoms, and (3) on-site transitions, when the polaron flips its orientation, but remains on the same site. Below we present and discuss calculations of these three paths on the E^0_{bind} PES.

The existence of a barrier along the path connecting the pristine and polaron configurations indicates the possibility for the co-existence of a delocalized *and* a localized charge carrier. In our simulations we find such a barrier in MgO, as shown in Fig. 2.6, but the height of the barrier is strongly supercell-dependent. Removing the finite-size effects by applying our correction scheme results in a barrierless transition. This is surprising, but is qualitatively in agreement with the semi-classical picture of the Pekar model, which predicts a parabola shown in Fig. 2.6 (b). In the adiabatic picture described by our polaron simulations, no stable free (delocalized) hole in MgO exists. However, due to different time-scales of the nuclear and electronic response, non-adiabatic effects can alter this conclusion. Note that the finite-size correction gives nearly the same result for all calculated points on the PES for the three different supercell sizes, confirming the validity of our polaron model in the long range. Deviations from the Pekar model (see Fig. 2.6 (b)) are due to the more accurate short-range description of the polaron, which is the advantage of our atomistic model in contrast to the continuum model of Pekar. However, we still rely on the adiabatic approximation. This approximation is likely to break in systems with quasi-degenerate states at the band edges.

The PES along the paths connecting polaron configurations localized at nearest-neighbor atoms and the on-site transformations in MgO are evaluated in a similar manner. The geometries are interpolated linearly between the initial and final polaron configurations to estimate the upper limit of the barriers. The finite-size effects on the barrier (concentration dependence) for these scenarios were found to be weaker, since the polaron state remained localized along the whole path. Let us first discuss the movement of the polaron along a path to a nearest-neighbor O atom. We focus on the path along the long axis of the p-orbital (the [110] direction) as shown in the inset of Fig. 2.7(a). Due to the large overlap with the O atoms in [110] direction, the barrier calculated with PBE is very low (0.045 eV) compared to the binding energy (-0.324 eV). The PBE barrier for the on-site rotation is 0.061 eV. Based on these results, we conclude that any in-plane motion of the polaron in MgO would combine a hindered on-site rotation and hopping to nearest-neighbor O atoms. Despite its high binding energy, the polaron hopping activation energy is rather small, indicating a high mobility. Yet, to

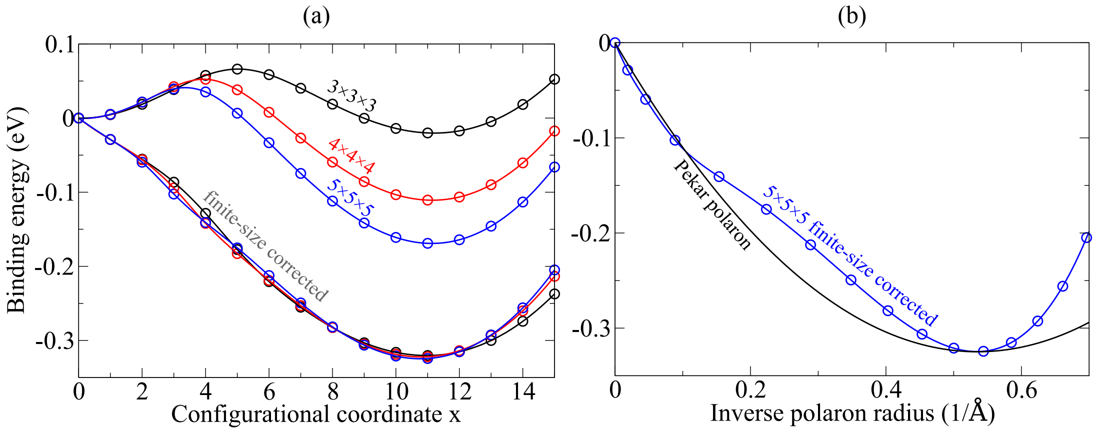

FIGURE 2.6: (a) PES of the polaron in MgO along a straight line starting from the perfect geometry (configurational coordinate value 0) to the optimized polaron geometry (configurational coordinate value 11) for three different supercell sizes. The configurational coordinate x is related to the displacements of atoms with respect to the perfect geometry as $x \cdot \Delta\mathbf{R}/11$, where $\Delta\mathbf{R}$ corresponds to the minimum-energy polaron geometry. The three topmost curves are the PES directly obtained from the PBE calculations, and the three remaining curves are the corresponding finite-size corrected ones for the $3 \times 3 \times 3$, $4\times4\times4$, and $5\times5\times5$ MgO supercells. (b) The PES as a function of the polaron radius. The polaron radius on the x axis was obtained by fitting Eq. (2.13) for each integer value of the configurational coordinate. The parabola corresponding to Pekar model was shifted to give the same binding energy as obtained in our simulation. The energy zero is set to the potential energy of the configurational coordinate 0. All calculations are carried out with the PBE functional on the E^0_{bind} PES.

our best knowledge charge carriers with such high mobility have never been observed in MgO (according to Arrhenius plots, charge carriers with activation energies around 1.1 eV lowest have been observed in the region of temperatures below 1300°C [119]). Thus, from our results it follows that the hole polarons are most likely trapped at deep donors such as the O vacancy, and the electrical conductivity is determined by the defects.

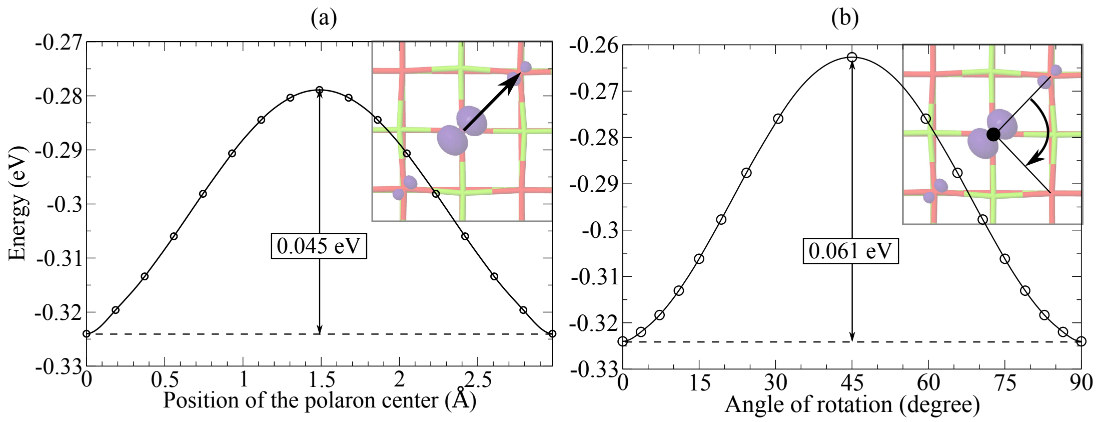

FIGURE 2.7: (a) The polaron PES along the line in [110] direction connecting nearest-neighbor O atoms. The direction is indicated by the arrow shown in the inset in the upper right corner. The change of the energy is given as a function of the position of the polaron center r_0 as defined in Eq. (2.13). (b) The binding energy as a function of the angle of rotation. The inset in the upper right corner shows the clockwise rotation in the (001) plane of the cell, as well as the start and end orientation of the polaron density indicated by the black lines. The energies in both figures are finite-size corrected, with the energy zero referring to the pristine configuration. All calculations are carried out in the $3 \times 3 \times 3$ neutral MgO supercell with the PBE functional on the E^0_{bind} PES.

Chapter 3

Small polarons in polymorphs of TiO_2 and Ga_2O_3

The developed approach presented in the previous chapter has been tested for a hole and electron polaron in different materials and the validity of our assumptions in our model could be confirmed. It could predict with sufficient accuracy the polaron binding energy and polaron level. As an interesting application of the approach, we investigate the structural dependence of the polarons for different polymorphs, i.e., materials with the same chemical composition, but different crystal structure. For each system, we first study the pristine crystal structure and its electron and phonon band structure. Based on the obtained parameters for the band mass, LO phonon frequency, and dielectric constants, we test the predictive power of the Fröhlich coupling strength as a descriptor of the small hole and/or electron polaron stability. Our results demonstrate that the Fröhlich constant is not uniquely defined in materials with complex crystal structure. Thus, its value as a descriptor of the polaron stability is limited. This emphasizes the value of the *ab initio* simulations of small polarons, which are presented at the end of the discussion for each material investigated in this chapter.

3.1 Rutile and anatase TiO_2

Titanium dioxide TiO_2 can appear in various polymorphs, where the most common are rutile, anatase, and brookite in descending thermodynamic stability order at ambient conditions. In addition, different high-pressure polymorphs were discovered over the past years. Yet, rutile and anatase are the most commonly used polymorphs for industrial applications, in particular in the area of hydrolysis [3] – the splitting of water into its elemental components. More breakthrough developments in the field of photochemistry followed, e.g. the Grätzel solar cell [120], or self-cleaning surfaces due to UV irradiation [121]. Although, the surface properties of the materials play a very important role for the applications, bulk properties have a significant impact as well, since the surface chemistry can be activated by the absorption of UV light happening

	Rutile		Anatase	
	This work	Exp. [123]	This work	Exp. [123]
O–O1	2.56	2.778	2.49	2.465
O–O2	2.96	2.959	2.81	2.793
Ti–Ti	2.96	2.959	3.06	3.039

TABLE 3.1: Nearest-neighbor distances for the rutile and anatase structure optimized with the PBE functional. The parameters of this work refer to distances at T=0 K and without zero-point motions, where the experimental values of Ref. [123] were measured at room temperature. All values are given in Å.

most likely not at the surface, but in the bulk. An important question for the photochemistry of heterogeneous catalysts is which kind of charge carriers are available in the bulk and how fast these carriers can reach the surface. This is determined primarily by the physical processes of the bulk, in particular by the competition between recombination, trapping, and propagation of the UV-generated electrons and holes. The following section presents a study of the self-trapping of the charge carriers in the otherwise pristine anatase and rutile crystals. Obviously, trapping hinders charge-carrier propagation. Despite the identical chemical composition, the self-trapping can explain in parts the different properties of anatase and rutile. Before evaluating this, we introduce the basic electron and phonon properties of the polymorphs to find out the alterations for the particular crystal phases.

Crystal structure. The tetragonal rutile phase of TiO_2 has six atoms in the unit cell and corresponds to the space group $P4_2/mnm$ (No. 136). The Ti atoms are sixfold-coordinated, where the O atoms have threefold planar coordination (cf. Fig. 3.1). The corresponding nearest-neighbor distances are summarized in the Tab. 3.1 and compared to experimental findings.

The optimization of the rutile structure using the PBE functional and adding small distortions to the atoms leads to a structure with slightly lower symmetry (changing from space group number 136 to 102) even in the unit cell. The coordination of the Ti atom remains slightly asymmetric as shown in Fig. 3.2. Subsequent calculations with different fractions of exact exchange α in the HSE06 functional confirmed this effect in the unit cell, but the distortion decreases with α (cf. the extended analysis in App. F.1). However, even for PBE the difference in energy to the perfect rutile structure is rather small (15 meV). The degree of the symmetry breaking in the pristine cell depends on the size of the supercell. An optimized structure of the $3 \times 3 \times 5$ supercell is shown in Fig. 3.2(b). The failure of the PBE functional in predicting the proper crystal structure for rutile TiO_2 has been reported earlier [122]. The crystal structure is predicted correctly with the PW-LDA functional. Thus, the problem is in the PBE functional.

Anatase has a tetragonal structure belonging to the space group *I4*$_1$*/amd* (No. 141). Although it has 12 atoms in the conventional unit cell, the nearest-neighbor coordination of the Ti and O atoms is similar to rutile, which can be seen by comparing Fig. 3.3

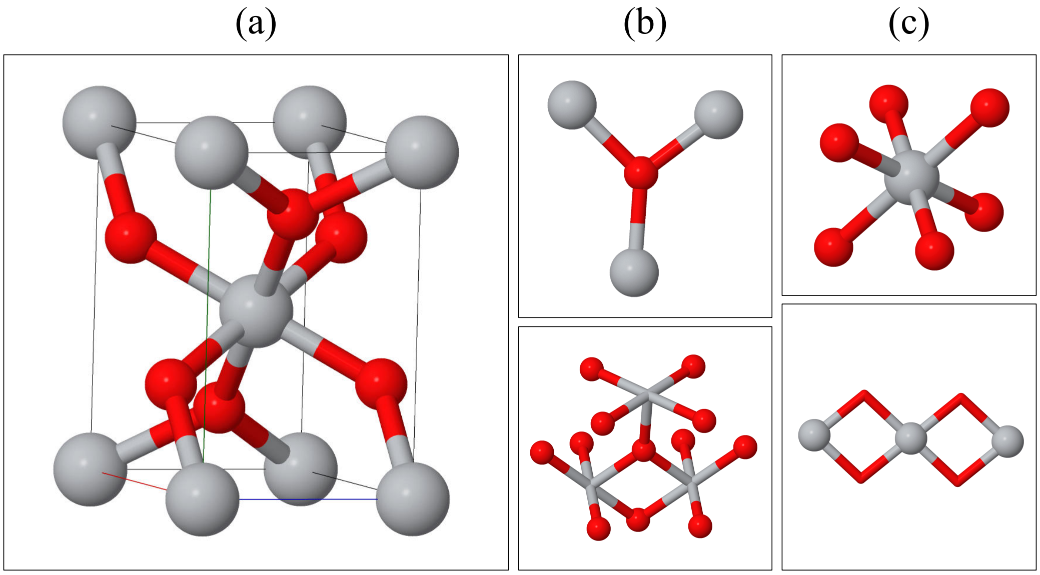

FIGURE 3.1: (a) The unit cell of the pristine rutile TiO_2 structure (without symmetry breaking). (b) The coordinations of the oxygen atoms (red spheres) (upper panel) and the nearest oxygen neighbors (lower panel), where the O atoms are represented as balls and for clarity Ti atoms as nodes. (c) The same as in (b) shown for the titanium atoms (gray balls).

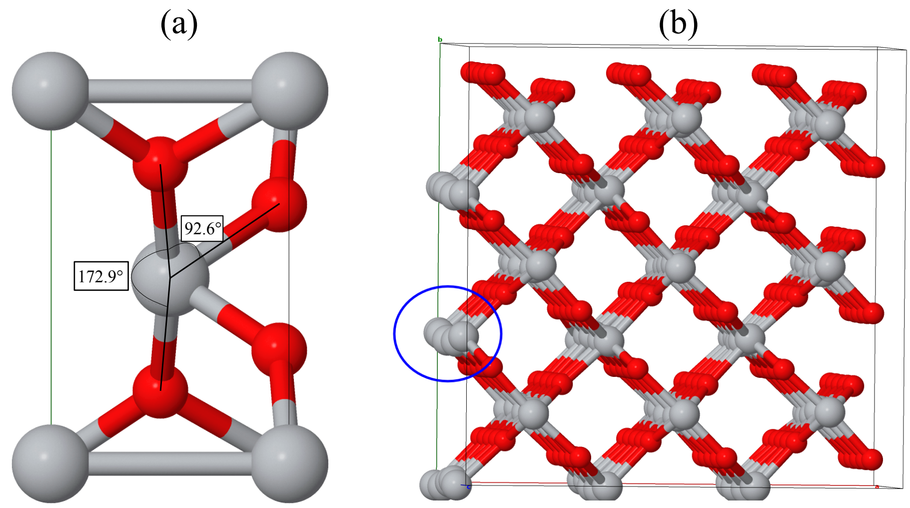

FIGURE 3.2: (a) Breaking the symmetry lowers the total energy of the rutile geometry. The angles of the central Ti are given to demonstrate the distortion (the angles in the perfect structure are 180° and 90°). (b) The optimized $3 \times 3 \times 5$ supercell. The blue circle points the strong symmetry breaking along soft modes.

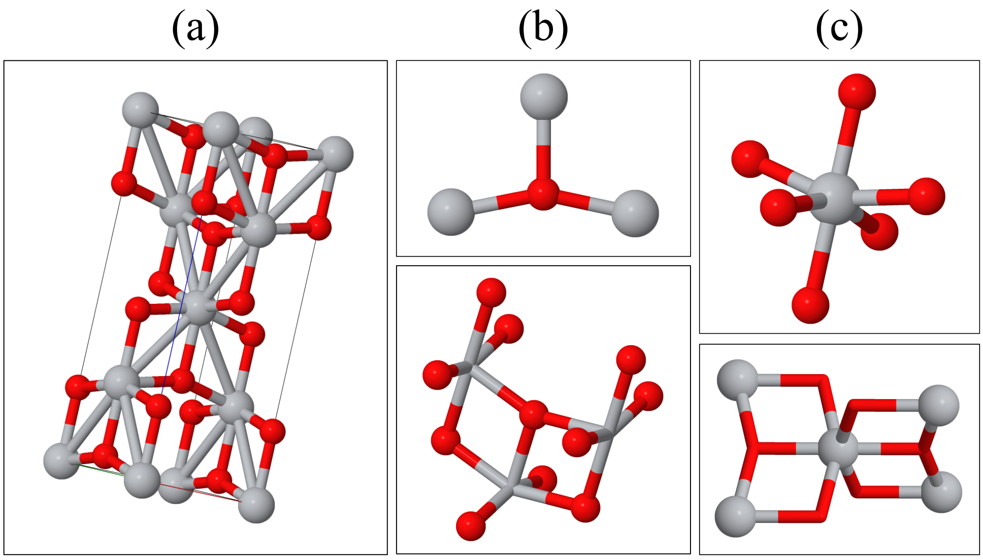

FIGURE 3.3: The unit cell of the anatase TiO_2 structure and the coordination of the corresponding oxygen (red spheres) and titanium (gray spheres) atoms.

with 3.1, top of panels (b) and (c). Differences become visible farther away from the central atom. For comparison, the distances between equivalent sites are listed in Tab. 3.1. For details of the crystal structure cf. App. F.2. There is also a slight difference in the number of nearest neighbors. The oxygen atom has eleven nearest oxygen neighbors in rutile, while the number for anatase is only ten. In contrast, the Ti atom is coordinated by two nearest Ti neighbors in rutile and four in anatase. As is shown below, this difference has important consequences for the small-polaron formation in these two polymorphs.

Electronic structure. As a consequence of the difference in the structure of rutile and anatase, there are differences in the electronic structure between the two TiO_2 polymorphs. The occupied and unoccupied KS bands in rutile and anatase TiO_2 are shown in Fig. 3.5 along a path connecting the high symmetry points in the Brillouin zone of tetragonal structure. For the estimation of the el-ph coupling based on the Fröhlich constant the proper evaluation of the band masses is crucial but ambiguous for a complex electronic structure as the one we find in TiO_2. First, we discuss the valence and conduction bands in rutile [Fig. 3.5(a)]. The valence bands have a pronounced maximum at the Γ point, with a rather small curvature. Yet, the situation is more complex for the conduction bands, where we find the minimum at the R point, with a higher curvature and, consequently, a lower band mass. However, close to the minimum there are flat bands along Γ–X–M–Γ, which tend to couple stronger to the LO modes, contributing to the stabilization of the polaron. The band mass along this part of the path is more than twice as high as for the VBM and, consequently, according to Eq. (1) to a higher coupling constant. Thus, it is unclear what value of the band mass is to be used for the estimation of the polaron properties for rutile. This emphasizes the need for *ab initio* calculations of polaron properties. Considering the range of masses for the conduction band, we find the range of $\alpha_{\mathrm{F}} = 2.2 \ldots 3.8$ for excess electrons in rutile. For the excess holes we find $\alpha_{\mathrm{F}} = 2.6$. Based on this estimation we can only conclude that for both types of charge carriers the formation of small polarons is similarly likely. The situation in anatase is more clear. We find a pronounced VBM at the M point and CBm at the Γ point (an indirect band gap). In Fig. 3.5(b) the CBm has clearly a higher curvature than the VBM, i.e., hole masses are higher than the electron masses. Based on the Fröhlich coupling constant with $\alpha_{\mathrm{F}} = 2.6$ and 1.2 for the excess holes and electrons, respectively, we can conclude that the hole polaron is much stronger localized and, probably, can be simulated with our supercell approach. Here we neglect the anisotropy of the band extrema, i.e., the fact that the effective masses are in general tensors.

The comparison of the density of states (DOS) clearly shows the differences between rutile and anatase electronic structure (see Fig. 3.4). The DOS at the conduction band edge (dominated by Ti d states) increases much sharper in rutile than in anatase, indicating flat bands with high electron masses, while for the valence band edge the situation is opposite. Summarizing the analysis of the electronic structure, we deduce that self-trapped electron polarons in rutile should be much more stable than in anatase, whereas the behavior of hole polarons in anatase and rutile is not clear from the discussion using only the Fröhlich constant. However, this is clarified by our *ab initio* approach discussed below. Due to the symmetry breaking described above rutile does not exhibit a direct band gap as reported in the literature (cf. e.g. Ref. [124]), due to changes in the conduction band. However, the difference between the Γ- to the R-point for the conduction band is less than 0.1 eV.

Phonon properties. The calculated phonon band structure (see Fig. 3.6) unveils again a complex picture – an anisotropic material with four LO modes at the Γ point. The two LO modes with the highest frequencies are marked by the blue shaded area in Fig. 3.6 representing the most important contribution to the polaron binding energy according to the Fröhlich model. The LO bands are not narrow and exhibit a significant dispersion. Thus, the assumptions in the Fröhlich model are not entirely fulfilled. However, since for $\boldsymbol{q} \to 0$ only the LO modes are contributing to the stabilization of the polaron (since $\boldsymbol{q}^T \boldsymbol{Z}^*_\kappa \boldsymbol{e}_{\kappa\nu}(\boldsymbol{q})$ vanishes for TO modes, cf. Eq. (2.7)), the finite-size correction based on Pekar's long-range el-ph potential leads to reasonable results for sufficiently large supercells (cf. Fig. 2.3(b)), which are close to the actual dilute limit as is shown in the next paragraph. For the frequency of the highest LO modes ω_{LO} we find 25.3 THz and 25.8 THz for rutile and anatase, respectively. The anisotropy of the crystal leads to a splitting of the LO modes at the Γ-point for different directions of the wave vector. The main contribution to the phonon DOS above 17 THz is from the LO modes for both rutile and anatase. In rutile the LO modes even separate from the remaining optical modes (as indicated by the blue shaded area in Fig. 3.6(a)). The dielectric tensors and the Born effective charges have been taken from Ref. [125] in order to evaluate the LO/TO splitting at the Γ-point.

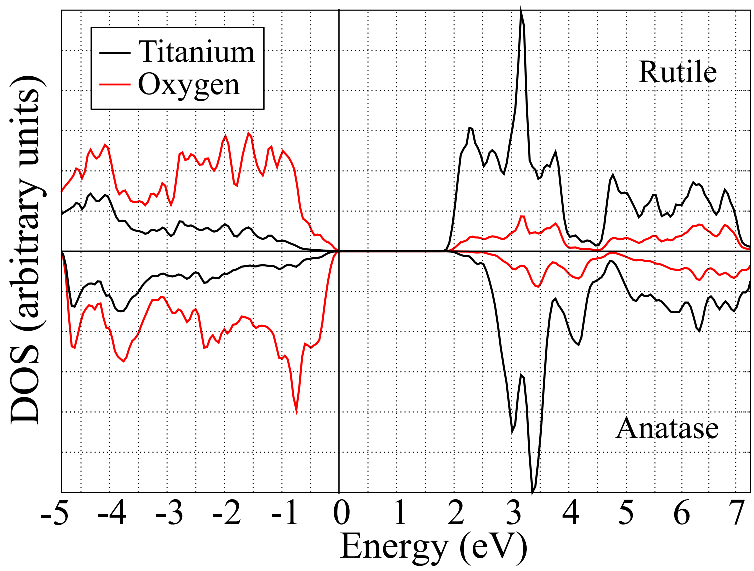

FIGURE 3.4: The electronic density of states for rutile (upper part) and anatase (lower part). To characterize the band edges the DOS has been projected onto the Ti (black line) and O atoms (red line). The zero of the energy corresponds to the VBM.

Small polaron formation. In the last paragraphs we have outlined the differences in geometry and electronic structure for anatase and rutile TiO_2. The subtle variations may appear negligible, but they have a significant impact on the small polaron formation. From the electron and phonon band structures we can estimate the Fröhlich coupling constant α_F. For the holes we obtain $\alpha_F = 2.6$ for both rutile and anatase, and for the electrons we obtain 2.2-3.8 and 1.2 in rutile and anatase, respectively. The estimates indicate that in rutile both electrons and holes could form small polarons, whereas in anatase only small holes could form. Below we show that these expectations are not exactly fulfilled, emphasizing the importance of more accurate polaron modeling.

Proceeding with the approach described in the Sec. 2.2.2, we start the atomic relaxation from ten initially distorted geometries for both an electron and a hole polaron in anatase and rutile. The atoms around the expected localization center are displaced randomly according to a Gaussian distribution. For the electron polaron the localization center is the Ti atom and for the hole polaron the O atom. The results for the electron polaron in rutile have already been presented in Fig. 2.3(b). For the hole polaron we could not find any stable self-trapped configuration (i.e., a localized hole with a negative binding energy) within the largest supercell considered ($4 \times 4 \times 6$ including 576 atoms). This is in agreement with the expectations: the VBM has a much weaker coupling to the phonon modes than the electrons. A much larger supercell may be needed in order to directly obtain the self-trapped polaron. On the contrary, we could only find a stable hole polaron in anatase, but no stable electron polaron in a supercell with a size up to $6 \times 6 \times 2$. The shape of the electron polaron in rutile is that of a d-orbital confirming the notion that the character of the polaron wave function is

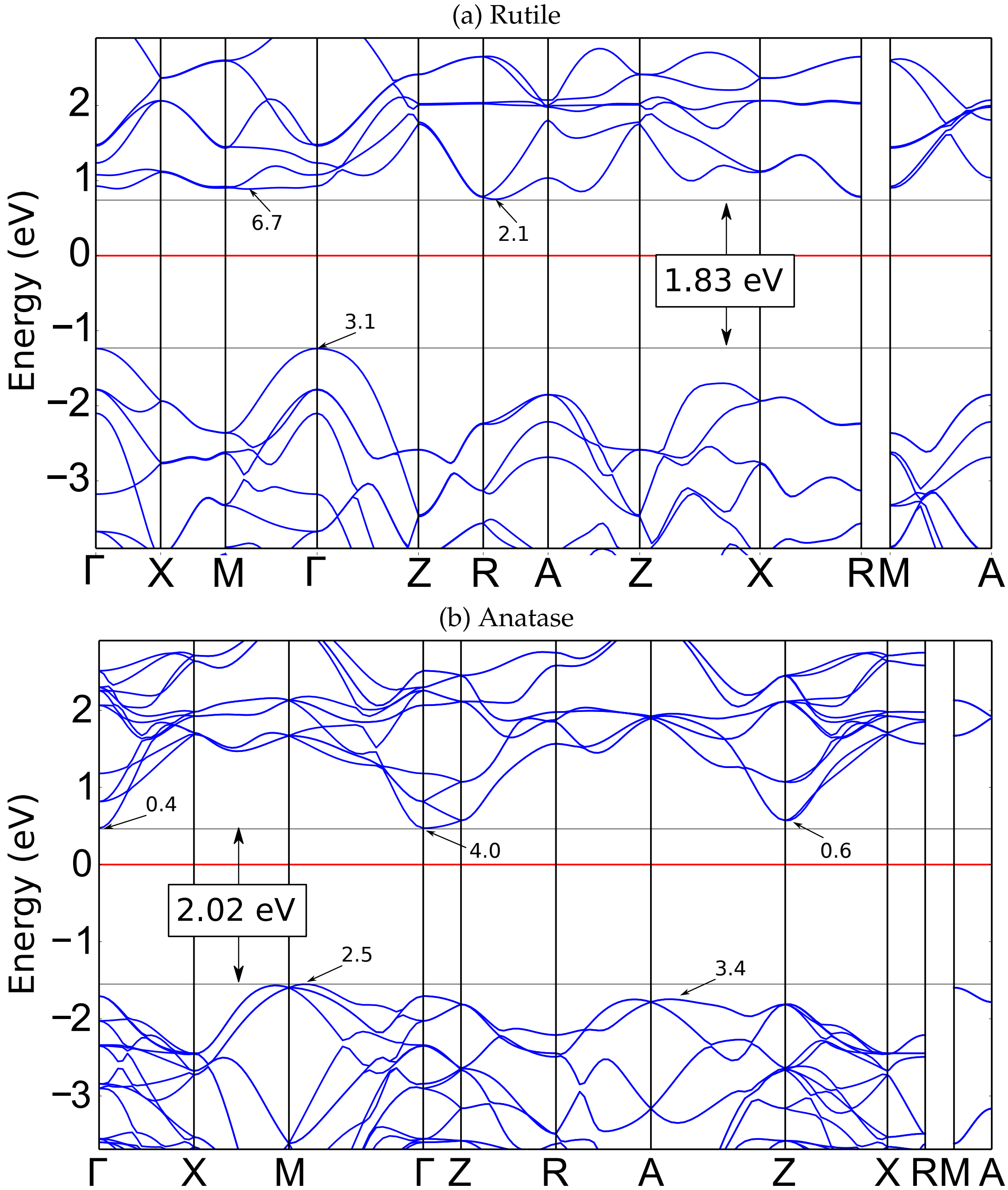

FIGURE 3.5: The electronic band structure of (a) rutile and (b) anatase calculated with the PBE functional. The numbers in the box indicate the band gap, and the small numbers with arrows show the calculated band masses.

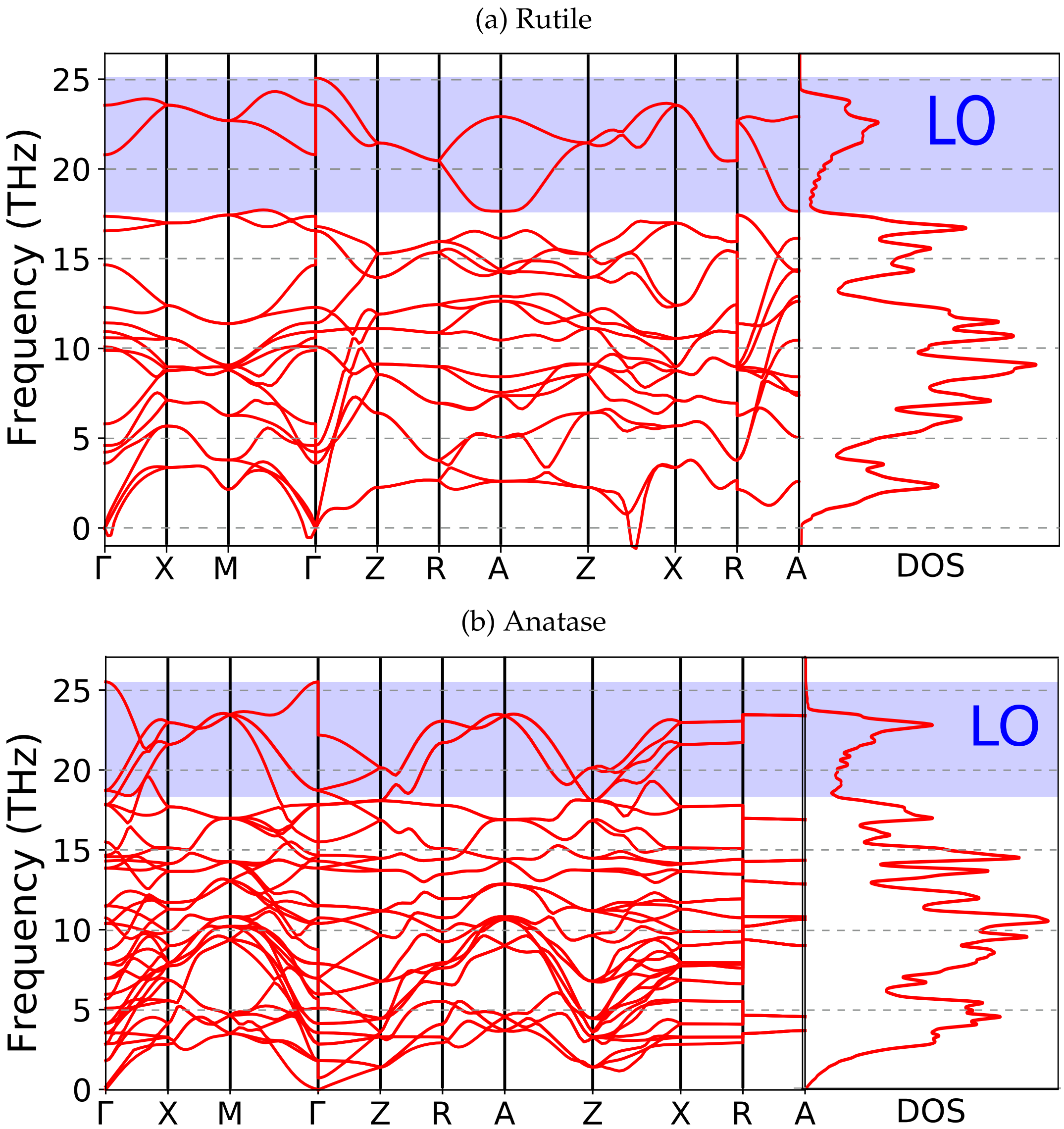

FIGURE 3.6: Phonon band structure and DOS (right panel) for (a) the slightly distorted rutile TiO_2 structure shown in Fig. 3.2, and (b) anatase. The blue shaded area indicates the contribution of the highest LO modes to the DOS. Despite reduced symmetry the rutile structure still exhibits soft modes.

derived from the character of the corresponding band edge. The electron is mainly localized at the three nearest neighbors shown in Fig. 3.1(c). The hole polaron in anatase is p-shaped and strongly localized at the oxygen atom.

In order to make a quantitative prediction we adjust the fraction of exact exchange α in HSE06 to reproduce the experimental band gap. As explained previously, our approach is much less sensitive to the underlying XC functional than the standard approach, and the polaron properties do not change qualitatively for the whole range of α, but there is still some quantitative dependence remaining. The dielectric tensors used for the finite-size correction can be found in the App. F.1 and F.2. We use $\alpha = 0.2$, which gives band gaps of 3.1 eV[1] and 3.3 eV[2] for rutile and anatase, respectively, in good agreement with the experiments. The level of the electron polaron in rutile is 1.0 eV below the CBm with a corresponding binding energy of -0.2 eV. Similar results for the polaron level were predicted by Janotti *et al.* [115]: 0.77 eV for the polaron level and a binding energy of -0.15 eV, using the conventional approach and HSE(α=0.25). It is noteworthy that despite the higher fraction of exact exchange Janotti *et al.* predicted a less stable electron polaron indicating that we might have found a more stable polaron configuration. Additionally, we find that the HSE(α=0.25) is still a convex functional for the polaron level by checking the condition EA=-$\epsilon_{\mathrm{lu}}(N)$. Consequently, the convex behavior leads to a smaller polaron level in the charged supercell.

Some of the observed spectroscopic features of TiO_2 have been attributed to an electron polaron [127, 112]. In TiO_2 the oxygen vacancy serves as an electron donor. The formal oxidation state of Ti atoms in TiO_2 is +4, while the electron-polaron self-trapping results in the change of the oxidation state to +3. An absorption peak near our simulated polaron level 1 eV could be assigned to a transition of the electron from a free (effective-mass like) to self-trapped state. Our (and others' [115]) work suggests that this reduction appears even in the absence of oxygen vacancies. The absorption maximum in the sub-gap region occurs at 0.75 eV at room temperature [128] in rutile TiO_2. Recent scanning tunneling spectroscopy (STS) experiments measured an electronic level at 0.7 eV below the band edge at 78 K [112], with the spectra being similar when taken near an oxygen vacancy or further away. It was concluded that the electrons can localize at any Ti atom and not only close to the oxygen atoms. The discrepancy between our result and the experimental values could be related to non-adiabatic and temperature effects, as well as the presence of oxygen vacancies in the sub-surface region, which were not taken into account in our calculations.

According to our simulations with the HSE(α0.2) functional and after removing the finite-size effects the hole polaron in anatase forms a level 1.2 eV above the VBM and has a binding energy of -0.52 eV (see Fig. 3.7). Thus, it is more stable than the electron polaron in rutile TiO_2. The available experimental results [129] are in good agreement with our predictions: the photoluminescence spectra of UV-irradiated (3.4 eV) anatase shows a peak at 2.3 eV, which corresponds to a level of 1.0 eV with respect to the VBM, stable up to room temperature. In the study of Setvin *et al.* [112] the STS

[1]The experimental optical band gap of rutile at 0K with zero-point renormalization removed is 3.04 eV, cf. [117].

[2]The experimental optical band gap of anatase at 0K with zero-point renormalization removed is 3.44 eV, cf. [126].

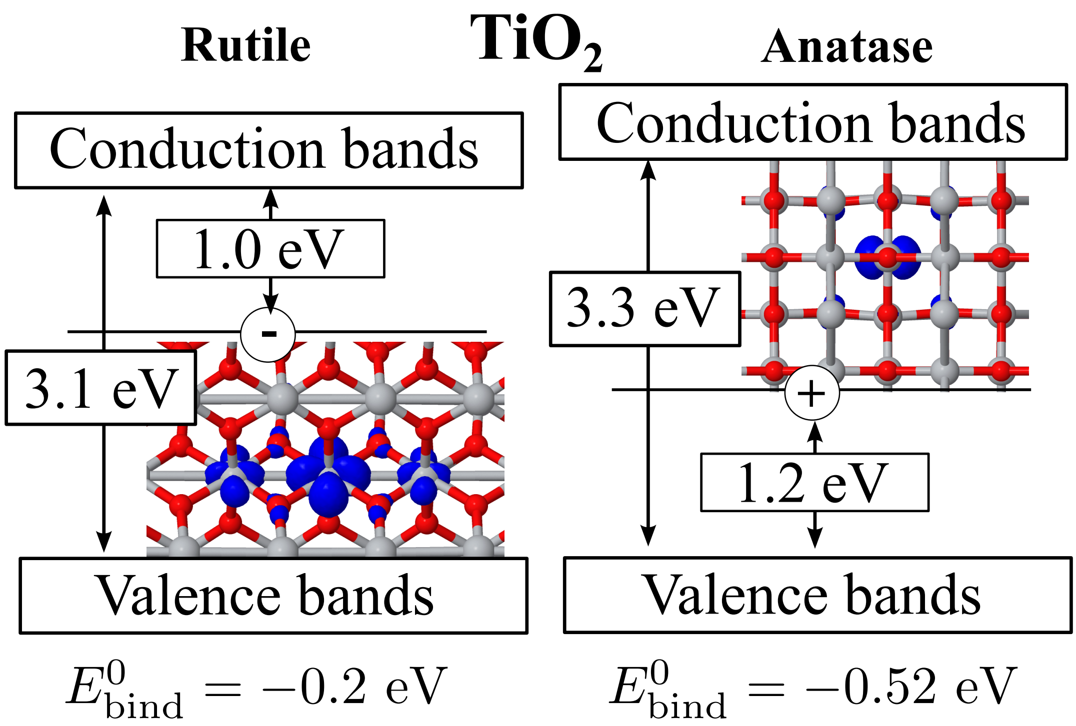

FIGURE 3.7: The electron polaron and hole polaron in rutile and anatase, respectively. The numbers are calculated with the HSE(α=0.2) functional and are finite-size corrected (i.e., correspond to the dilute limit). The KS eigenstate densities of the corresponding polaron are shown as insets, where the isosurfaces encompass 95% of the eigenstate density.

spectra were similar for the pristine and reduced materials (where oxygen vacancies were found). It was therefore concluded that free electrons can move quickly to the oxygen vacancies and do not self-trap at the Ti sites, confirming our result of no stable electron polaron in anatase. The high mobility of electrons in anatase has been already reported by Forro *et al.* [130].

In summary we find that, despite the identical chemical composition, the two polymorphs of TiO_2 show opposite self-trapping behavior for different types of excess charges. This difference is traced back to the different coordination environments of the Ti and O atoms. However, to get a more realistic picture of the behavior of the charge carriers in anatase and rutile, defects such as oxygen vacancies and/or the trapping at surface states have to be taken into account. Nevertheless, our study helps to understand why rutile has been successfully used as a photocatalyst for oxidation: Due to its light mass the photo-generated hole propagates easily to the surface. However, it has been argued that anatase should be the better photocatalyst, since the lifetime of the charge carriers should be higher due to the indirect band gap [131]. This illustrates how the actual application of a material depends on multiple properties. The polaron formation is one of these important properties.

	crystal system (SG)	ΔE/FU (eV)	band gap (eV)
α	trigonal (167)	0.145	2.40 (indirect)
β	monoclinic (12)	0.0	1.99 (direct)
δ	cubic (206)	0.151	2.25 (indirect)
κ	orthorhombic (33)	0.102	2.08 (indirect)
γ	defected spinel (227)	0.207	1.33 (direct)

TABLE 3.2: Five different phases of Ga_2O_3. The geometries have been optimized and the electronic structure has been calculated with the PBE functional. The energy difference per formula unit ΔE/FU is given with respect to the β-phase, which is the most stable out of the five phases at T=0K and standard pressure. The number of the space group (SG) is given in parenthesis in the column of the crystal system. As a general trend, the stability of the phases decreases with increasing symmetry of the crystal.

3.2 The β– and κ–phase of Ga_2O_3

Gallium oxide is anticipated to be a promising material for several applications in the field of transparent conducting oxides (TCO) and high voltage devices. Although, the interest in this material has only started a few years ago as in a potential successor of the more expensive indium oxide, its applicability has been already proved in several devices: field-effect transistors [132, 133], UV photodetectors [134, 135], and UV transparent electrodes [136]. The soaring demand of Ga_2O_3 is originated in its unique combination of properties, such as its high band gap of about 4.8-4.9 eV [137, 138], a high breakdown electric field of about 8MV/cm [133], and a high n-conductivity with electron concentrations (due to doping) of about 10^{19} cm^{-3} [139, 136]. Throughout all the applications only the monoclinic β-phase of Ga_2O_3 is used, which is the thermodynamically stable polymorph (cf. Ref. [140], Fig. 14, for an overview of the stability conditions and the duration of existence for several polymoprhs of Ga_2O_3). However, other phases have been already discovered long time ago [141] and are named analogous to the phases of the related sesquioxide Al_2O_3. A list of the different phases and basic information about them are given in Tab. 3.2. For the investigation of the small-polaron formation we only focus on two configurations – the β- and κ-phase.

Geometry. The structure of the Ga_2O_3 β-phase is well-understood and characterized. The monoclinic crystal has 20 atoms in its conventional unit cell containing four formula units. The crystallographic properties calculated with the PBE functional are summarized in Tab. 3.2. All atoms of one formula unit of the β- (and κ-)phase occupy different Wyckoff-positions and, with this, have (slightly) different coordinations. Therefore, we only focus on important differences in our analysis. The β- and κ-structures used here and in the following have been optimized with the PBE XC functional and with *tight* FHI-aims settings. The complete structural information for the β and κ phases is given in the Appendix G and the unit cells are visualized in Fig. 3.8, panel a.

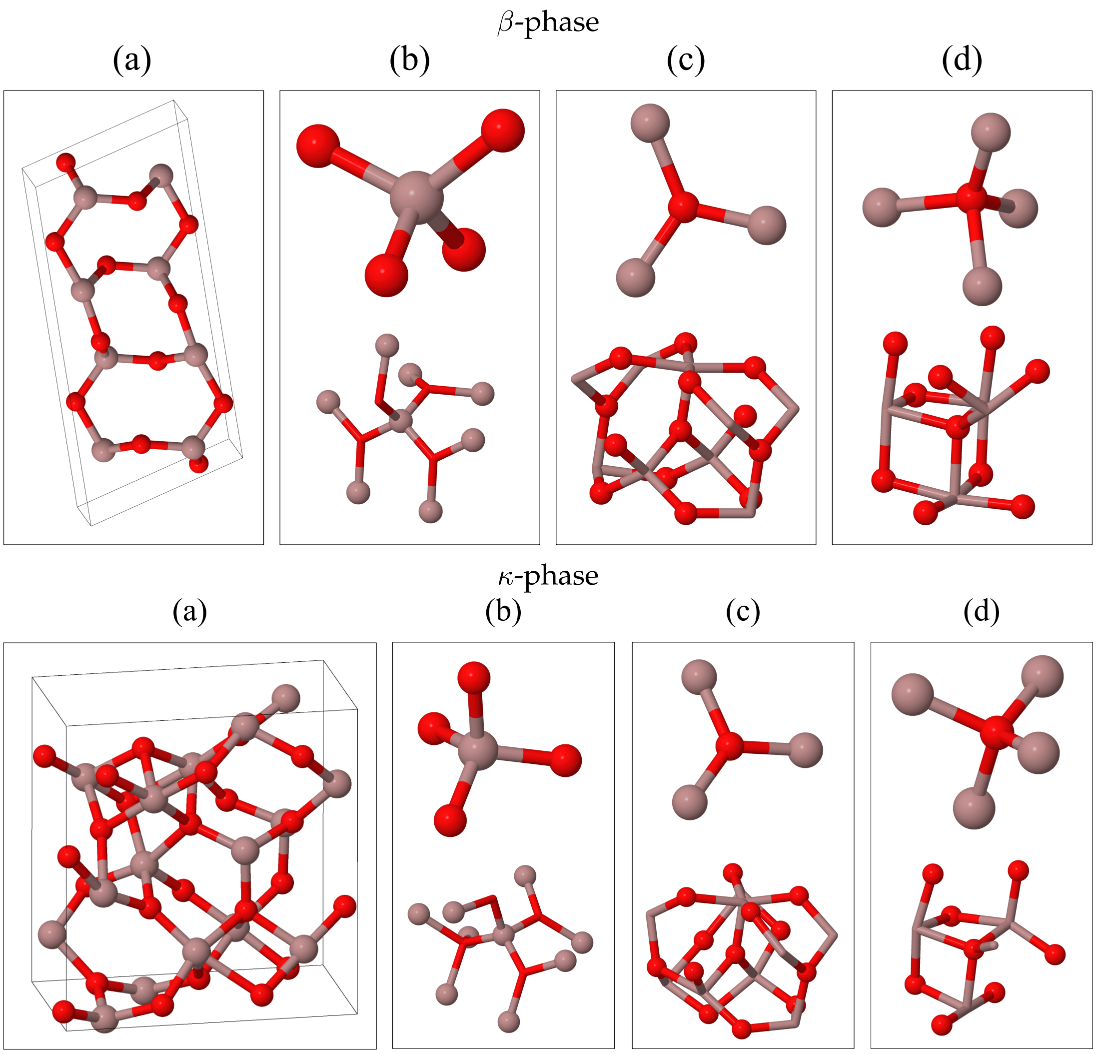

FIGURE 3.8: The conventional unit cells of the β- (upper panels) and κ-phase (lower panels). A selection of characteristic atom coordinations and nearest-neighbor structures are shown in panels (b)-(d). Red and gray spheres represent O and Ga atoms, respectively. The atom positions and lattice parameters are given in Appendix G.

For the less studied κ phase inconsistent naming can be found in the literature. Roy *et al.* discovered a fifth phase naming it ϵ according to the position in the Greek alphabet. However, they could not identify a crystal structure of this phase. Today, it is believed that this fifth phase from Roy *et al.* corresponds to the orthorhombic crystal class analogous to the κ-polymorph of Al_2O_3, which is why the orthorhombic Ga_2O_3 is often denoted with κ, i.e., both classifications can be found in literature. Here, we follow the consistent labeling according to the Al_2O_3 phases. Up to now, studies of the κ-phase are scarce. It only appeared transiently during a conversion from $Ga_5O_7(OH)$ to the thermodynamically stable β-phase at 500°C [140].

Figure 3.8 shows the Ga and O coordination in the two polymorphs. It can be immediately seen that the coordination in both polymorphs is similar: the Ga atoms are tetragonally bonded with the neighboring O atoms. For the O atoms a trigonal-planar and tetragonal coordination can be found. Noticeable differences can be found if the arrangement of the nearest neighbors of the same atom type is considered. In κ-Ga_2O_3 we find a higher number of nearest Ga atoms than in the β-phase, as shown in Fig. 3.8, panel b. An almost identical nearest-neighbor structure in the two phases is found for the trigonally-coordinated O atom, where the central O atom is enclosed in a cage-like structure with the same number of nearest neighbors (Fig. 3.8, panel c). However, the tetragonally-coordinated O atom has a significantly different environment in the two polymorphs (Fig. 3.8, panel d). Moreover, there are additional building blocks in κ-Ga_2O_3, which are not present in the β-phase.

Electronic structure. Our analysis of the geometries unveiled minor differences in the coordination of the two atoms Ga and O in the β- and κ-phase. Similarly, we find for the electronic properties large similarities. The PBE band gap changes only by 0.09 eV from 1.99 eV for the β phase to 2.08 eV for the κ-phase. In both phases, the top-most valence bands (dominated by oxygen states) are very flat, and the the bottom of the conduction band (dominated by Ga states) has a parabolic shape with a high curvature (Fig. 3.9). However, the values of the band masses reveal that the valence bands are significantly flatter in κ-Ga_2O_3 than in the β-phase (m_b=57 and =6.7-36 for the κ- and β-phase, respectively), which is supported by the more pronounced peak in the DOS close to the VBM. Even lower-energy valence bands remain flat in κ-Ga_2O_3. The conduction bands exhibit the opposite behavior: the band mass is smaller in κ-Ga_2O_3. This is in good agreement with our geometric analysis, where we found that some of the Ga atoms have a higher number of nearest neighbors, and some of the oxygen atoms have a lower number in the κ phase. Based on these observations one can conclude that if holes get self-trapped in the β-phase, the self-trapping should be even more pronounced in the κ-phase.

Phonon properties. Due to the large number of atoms in the conventional unit cell (20 and 40 atoms for β and κ phases, respectively), the system's response to an excess charge cannot be described by a few well-defined phonon modes (Fig. 3.10). Both β and κ phases exhibit optical modes with rather low frequencies around 2.5 THz. For the highest optical mode we find 22.5 THz and 22.3 THz for the β and κ phase,

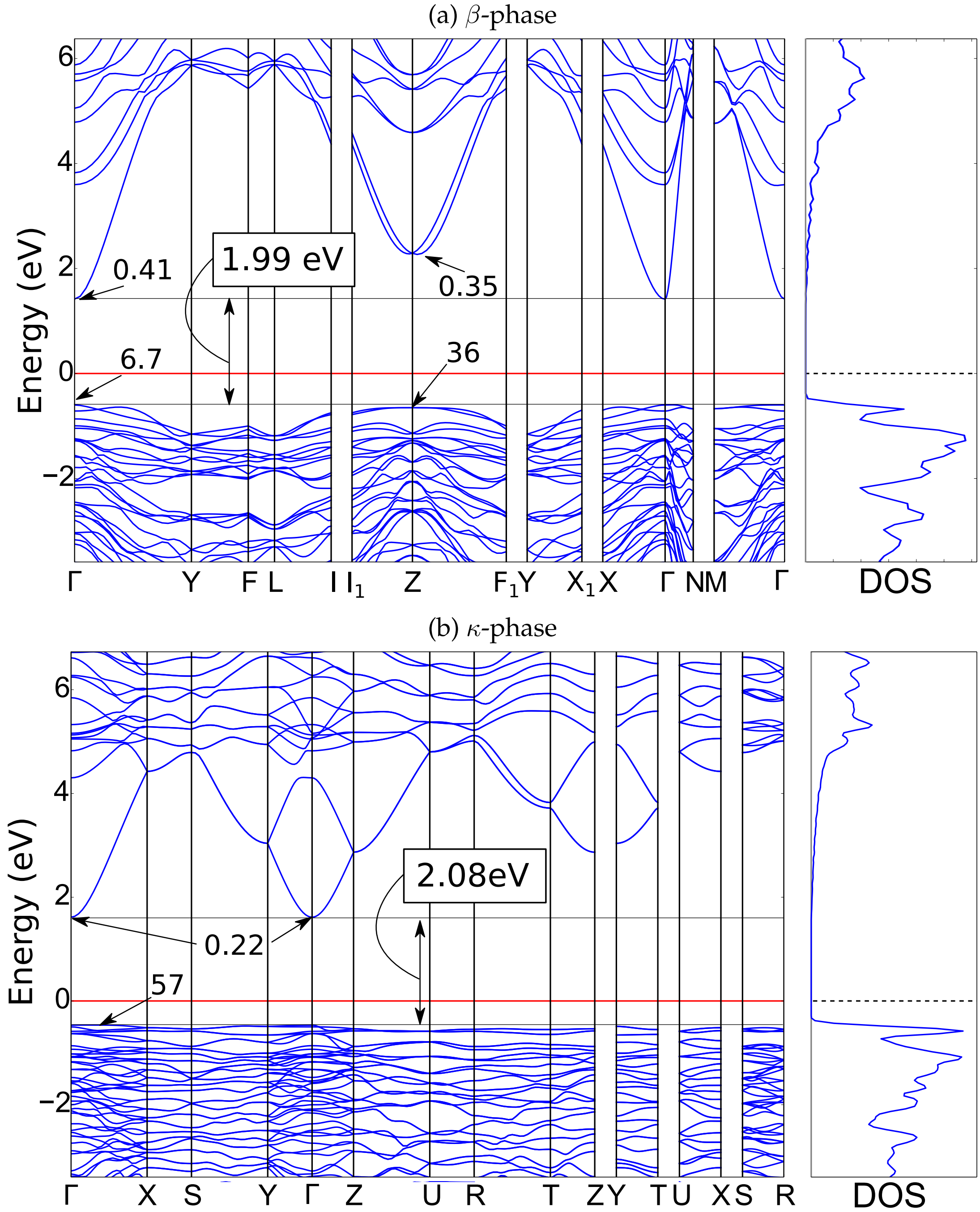

FIGURE 3.9: The electronic band structure for the (a) β- and (b) κ-phase of Ga_2O_3 along a path connecting high-symmetry points, calculated with the PBE XC functional. The corresponding DOS is shown on the right side. The numbers in the boxes show the PBE band gap, and the numbers with arrows are the calculated band masses of the conduction and valence bands at the extrema.

respectively. Note that the non-analytic correction [75] has not been applied to the LO modes in Ga_2O_3. According to the literature [142], the correction is rather small for β-Ga_2O_3.

Small-polaron formation. We proceed in the same way as in the case of TiO_2. A fraction of exact exchange $\alpha = 0.4$ is needed to obtain the value of the gap close to the experimental band gap of 4.8-4.9 eV for β-Ga_2O_3. Since we could not find any measured band gap for the κ-phase, we used $\alpha = 0.4$ for κ-Ga_2O_3 as well. The dielectric parameters and polaron radii needed for the finite-size correction are listed in the Appendix G.

Fig. 3.11 summarizes the results of the calculations of the polaron binding energy E^0_{bind} and the hole-polaron level E_0. An electron polaron has not been found using supercells up to 240 and 320 atoms for the β- and κ-phase, respectively. On the other hand, we find strongly localized holes corresponding to deep polaron levels with 1.9 eV and 2.2 eV with a large binding energy of -0.85 eV and -1.12 eV in the β- and κ-phase, respectively. The dielectric tensors used for the finite-size correction can be found in the App. G.1 and G.2. The explicit supercell size dependence was tested for the κ phase (using the PBE functional) and was tested against our finite-size correction (cf. App. G.3). Again we find that the finite-size correction for both the binding energy and the polaron level for every supercell size is close to the explicitly evaluated dilute limit (the uncertainty is below 0.1 eV).

Photoluminescence data are only available for β-Ga_2O_3. Three characteristic luminescence bands have been detected in the region of UV [143, 144], blue [145, 146, 144], and green [147] wavelengths with energies of 3.4 eV, 2.95 eV, and 2.48 eV. The UV luminescence has been observed to be independent of the sample (doping and history) from which is concluded that it appears due to the recombination of the self-trapped exciton [143]. No mechanism has been proposed for the green luminescence so far. The blue luminescence (BL) is usually attributed to Ga-O defect complexes. The BL was first claimed to be observed only for n-doped (e.g. Si or Sn) Ga_2O_3. However, a recent study [148] showed that a shoulder at around 3.0 eV is present in the spectra independent of the type of doping : (n-, p-, or pristine). Consequently, the BL can be also attributed to intrinsic properties. However, it remains unclear whether this spectral feature can be at least partly attributed to self-trapped hole polarons. According to our calculations (Fig. 3.11) this can be the case. The broad luminescence band indicates that there are several states in the sub-gap region, responsible for multiple channels of the broad-band luminescence. In Fig. 3.12 we summarize pictorially the experimental results of Onuma *et al.* [148]. The panel (a) shows the situation for the Mg-doped Ga_2O_3, where the samples were insulating or p-type semiconducting. Clearly, in this case the BL should appear strongest, if the Fermi level is below the polaron level. Panel (b) explains why in case of n-doped samples the BL is suppressed. In this case, the Fermi level is close to the CBm, and all defect states below should be filled. As a result, lower-energy optical transitions within the gap become possible.

(a) β-phase

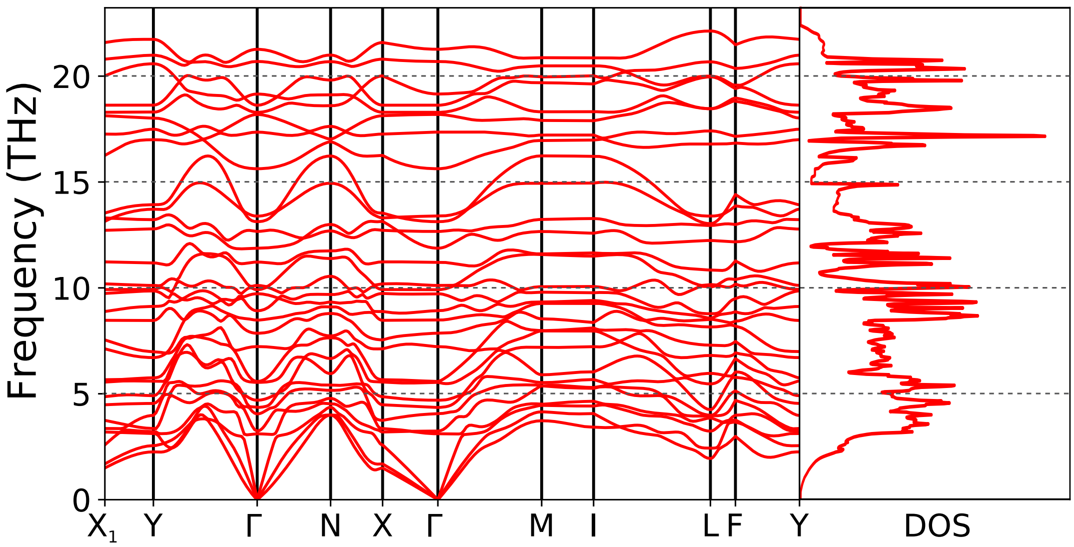

(b) κ-phase

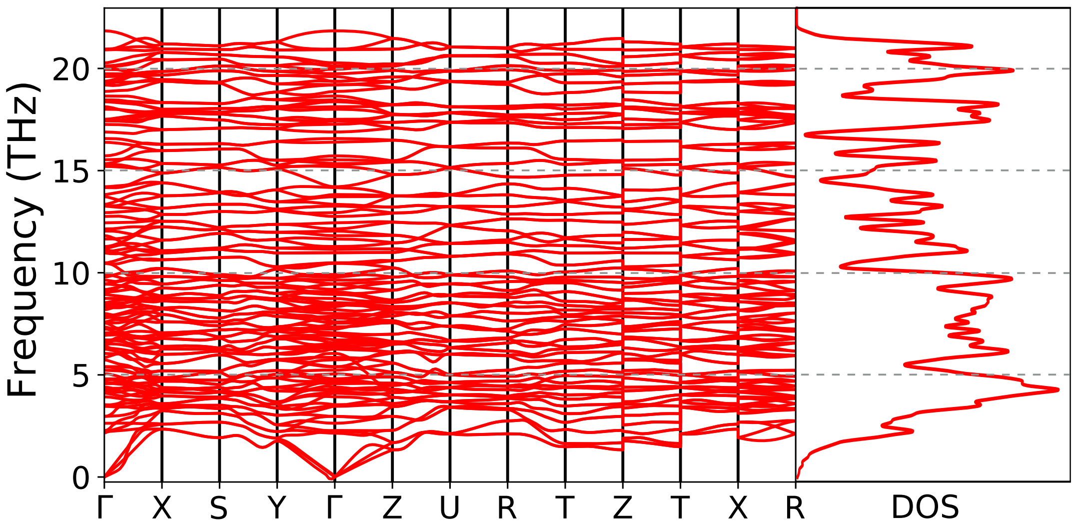

FIGURE 3.10: The phonon band structures for the (a) β- and (b) κ-phase of Ga_2O_3 along the path connecting high-symmetry points, calculated with the PBE XC functional. For (a) the primitive unit cell is used. The corresponding DOS is shown on the right side. The non-analytic term correction has not been taken into account for the LO/TO splitting, i.e., the actual highest LO mode should be higher than shown here.

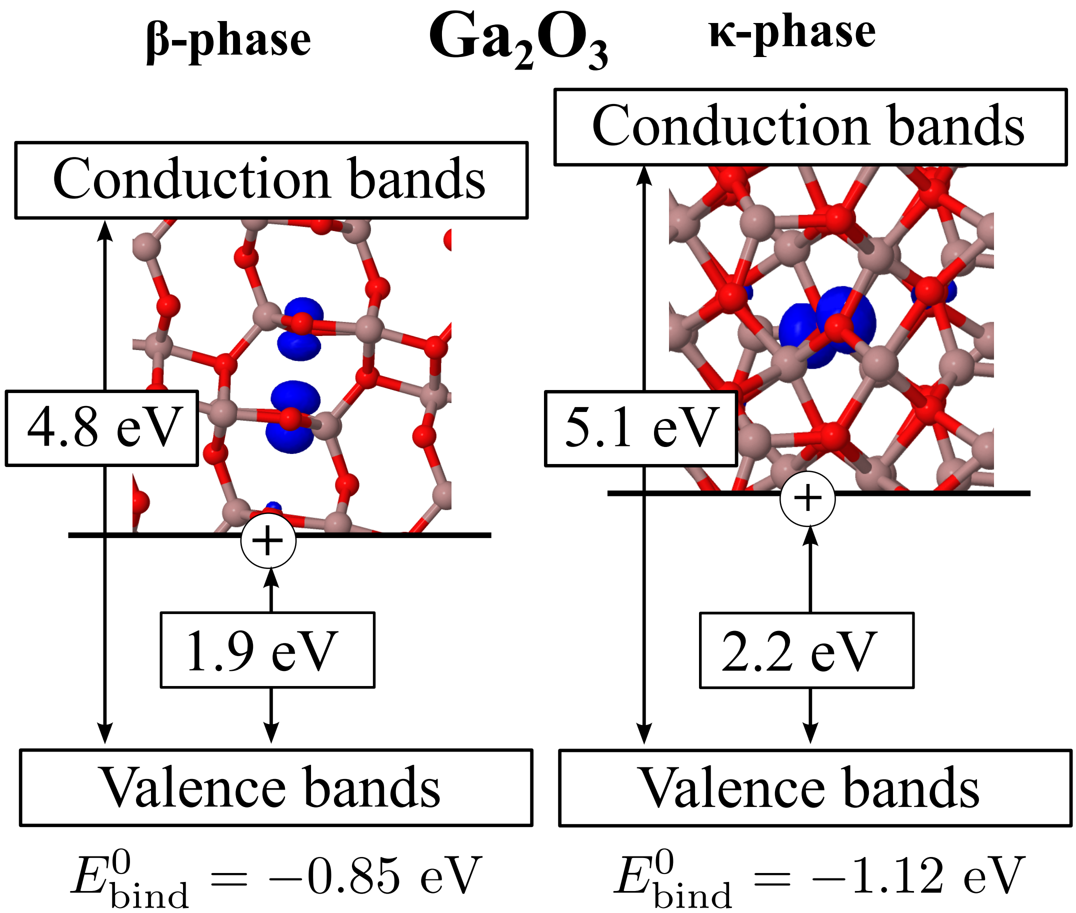

FIGURE 3.11: The hole polarons in β- and κ-Ga_2O_3. The numbers are calculated with the HSE06(α=0.4) functional and are finite-size corrected (i.e., correspond to the dilute limit). The KS eigenstate densities of the corresponding polaron are shown as insets, where the isosurfaces encompass 95% of the eigenstate density.

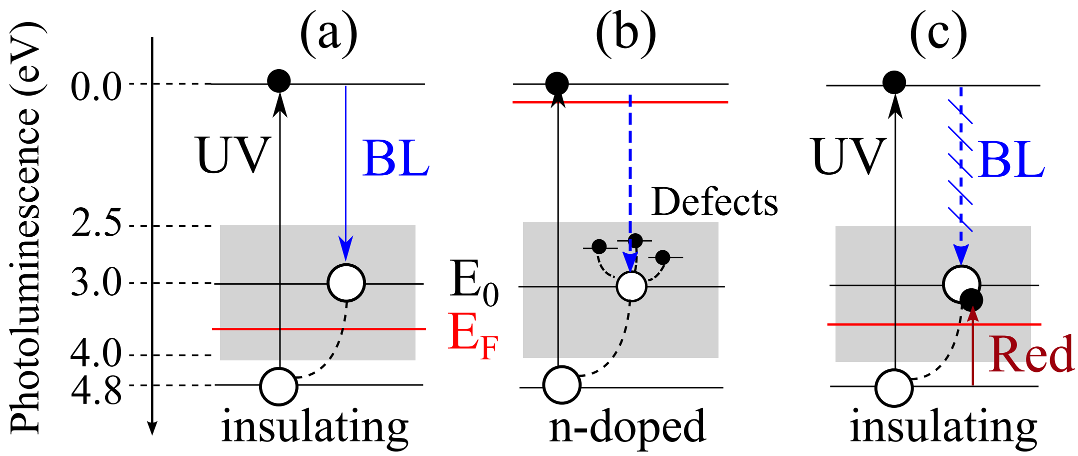

FIGURE 3.12: Photoluminescence (PL) of β-Ga_2O_3 according to the experimental results [148]. The gray shaded area indicates the upper and lower limit of the observed PL, E_0 is the self-trapped hole polaron level position with respect to VBM. The red line marks the Fermi level E_F for different scenarios: (a) the insulating case for an Mg-doped sample and (b) n-doped samples Panel (c) suggests a pump-probe experiment to estimate the position of the polaron level with respect to the VBM (or Fermi level) by pumping the sample with red light and subsequently probing UV-induced luminescence.

Based on our results and analysis, we suggest the following pump-probe type experiment to determine the position of the polaron level in p-doped Ga_2O_3. An illumination of the sample with red light in the region of 2 eV with UV radiation 4.9 eV[3] at the same time will pump electrons from the valence band to the states of the polaron. When the pump photon energy of the red light matches the polaron state energy, an increased absorption should be observed (e.g. compare with the experiment in [149]) or, alternatively, a suppression of the BL following a UV probe illumination should be observed.

[3]The UV light of 4.9 eV excites electrons from the VBM to the CBm and creates holes at the VBM, which then relax to the final polaron state.

Chapter 4

Conclusions

In the present work we developed a new *ab initio* supercell approach for the simulation of small polarons. The approach overcomes severe shortcomings of the traditional charged supercell approach, in particular the strong exchange-correlation functional dependence, which makes even a qualitative prediction of small polaron stability uncertain. This uncertainty was demonstrated for the HSE06 functional by varying the fraction of exact exchange from 0 to 1. The reformulation of the polaron binding energy in terms of energies calculated in the neutral supercell fixed this strong dependence on the functional approximation. However, we found much more pronounced finite-size effects in the neutral cell by comparing supercells of different sizes. An analysis of the classical polaron theories based on the semi-empirical Hamiltonian of Fröhlich shows that the adiabatic el-ph potential Eq. (2.9) proposed by Pekar can properly model the missing long-range electron-phonon interactions in the supercell. Pekar's potential of this long-range interaction was used in the *a posteriori* finite-size correction similar to the correction of Freysoldt *et al.* to obtain the polaron binding energy and the corresponding level in the dilute limit. The new approach is completed with the proposal of Sadigh *et al.*, who suggested a way to calculate forces in a supercell with a localized charge using only the neutral supercell. Thus, the approach opened the possibility to obtain qualitatively correct polaron properties using computationally inexpensive XC-functionals such as PBE for large supercells with up to 1,000 atoms. The approach suggested in this study was thoroughly tested with respect to supercell size and the XC functional dependence, and was demonstrated to work for electron and hole polarons likewise. As a continuation of our study, it would be interesting to investigate how the proposed generalized long-range el-ph response Eq. (2.7) of the solid to an isotropic excess charge improves the description of anisotropic and complex materials.

The new insights into the DFT supercell approach were applied to investigate the formation of small polarons in polymorphs of TiO_2 and Ga_2O_3. The rutile and anatase phases of TiO_2 show a very unique behavior. Despite their equal chemical composition and small changes in the crystal structure, we only found small electron polarons in rutile, whereas in anatase only small hole polarons have been found. This is in good agreement with the experimental data available in the literature. The different self-trapping behavior opens new possibilities for understanding and manipulating chemical reactions at the surfaces, e.g., for photocatalysis. By contrast the polymorphs of Ga_2O_3 exhibit a uniform self-trapping behavior. The electrons in the β- and κ-phase

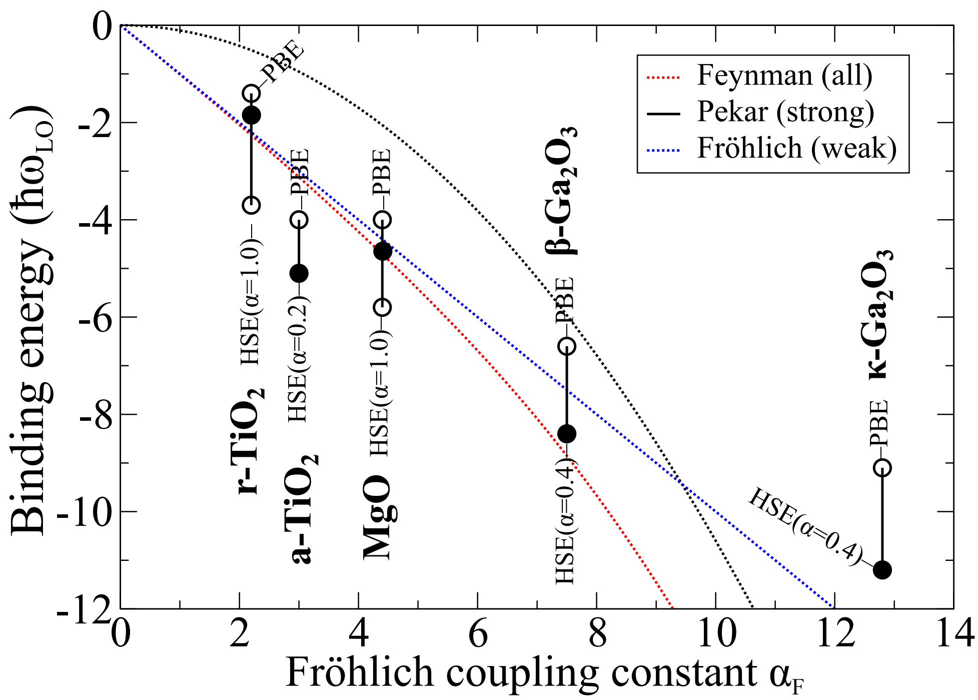

FIGURE 4.1: The polaron binding energies E^0_{bind} obtained with the DFT supercell approach, in comparison with different solutions of Fröhlich's Hamiltonian. The pairs of circles connected by the vertical lines represent the DFT results in the dilute limit for the small polarons in the simulated materials, where the empty circles indicate the range of the simulated functionals (HSE06(α=0) corresponds to PBE). The black filled circles show E^0_{bind} for the fraction of exact exchange to reproduce experimental band gaps as it was described in the previous chapter (for MgO HSE06(α=0.35) was used). In MgO, anatase TiO_2 (a-TiO_2), and β- and κ-Ga_2O_3 stable hole polarons have been found, while in rutile TiO_2 (r-TiO_2) a stable electron polaron is found.

couple weakly to the polar phonon modes, whereas the holes exhibit a very strong el-ph interaction. Consistently, we find strongly bound hole polarons with a level deep in the gap. Due to their high binding energy small polarons in Ga_2O_3 could serve as reasonable explanation for the observed broad luminescence bands. Traditionally, the observed blue luminescence is attributed to defects. However, recent experiments showed that blue luminescence is present in n-, p-, and undoped samples [148]. Based on our results, we provide an alternative interpretation of the blue luminescence signal, namely as due to the self-trapped hole polaron level at about 2 eV above the VBM.

Our findings are summarized and compared to common approximate solutions of the Fröhlich Hamiltonian in Fig. 4.1. One of the advantages of our DFT approach for calculating polaron properties over Fröhlich's Hamiltonian is that the ionic lattice is considered explicitly in our polaron approach. Such a description is particularly appropriate for small polarons that have been of interest here. The DFT approach is based on the adiabatic (Born-Oppenheimer) approximation. As such, in the strong-coupling limit, it physically corresponds to Pekar's polaron model, the adiabatic static description of polarons, where the polarization of the lattice is treated classically. Pekar's model predicts smaller (in absolute values) polaron binding energies compared to DFT. Considering that in Pekar's model (as well as in Fröhlich's Hamiltonian) the electron (or hole) only interacts with a single phonon mode, it is not surprising that Pekar's solution only provides an upper limit to the polaron binding energy. The el-ph interaction for the small polaron includes couplings to almost all the phonon modes throughout the Brillouin zone, leading to a further stabilization of the polaron in our simulations. The DFT results are close to Feynman's approximate solution of the Fröhlich Hamiltonian [82]. However, Feynman's model includes quantum fluctuations and non-adiabatic effects [150] due to the interaction with a single dispersionless phonon mode, not accounted for in our DFT approach and, therefore, should not be compared with the DFT results directly. Thus, on the one hand the comparison between Pekar's and Feynman's approximate solution shows the significance of possible non-adiabatic effects for polarons in oxides. The impact of non-adiabatic effects can be crucial in the range of the weak and intermediate coupling ($\alpha_{\mathrm{F}} < 5$), where the difference of the binding energies obtained from the Pekar and Feynman models is large. For $\alpha_{\mathrm{F}} > 5$, the binding energies calculated with the two models are very close and only shifted by a constant, cf. Eq. (1.83). On the other hand, by comparing Pekar's solution with our DFT results the importance of the proper microscopic treatment of the lattice polarization is illustrated. This becomes obvious for the Ga_2O_3-phases, where the el-ph interaction is very strong. Fröhlich's Hamiltonian predicts for increasing coupling strength a collapse towards a point charge. This, however, is not physical, since only a finite polaron radius is reasonable. Indeed, as can be seen in Fig. 4.1, the binding of a hole polaron in the κ-phase of Ga_2O_3 is significantly weaker than the binding predicted by Pekar's solution, despite the strong el-ph coupling. This underlines the importance of *ab initio* calculations for predictive modeling of small polarons.

Chapter 5

Outlook

Number of distinct polarons in a crystal

For rocksalt MgO, and rutile and anatase TiO_2 phases investigated in this thesis, all species of the same type occupy identical Wyckoff position, i.e., all atoms of the same species are equivalent. Therefore, as expected, we find only one stable small polaron (if at all) localized near the corresponding atomic species (hole polarons at O atoms and electron polarons at metal atoms). However, the situation is different for the polymorphs of Ga_2O_3. Since in Ga_2O_3 only the formation of small hole polarons is predicted, we focus on distinct oxygen positions. In the β-phase, all O atoms occupy the Wyckoff position $2i$, but at different spatial positions (cf. Tab. G.1). In the κ-phase, the O atoms occupy six different Wyckoff positions $4a$. Consequently, we expect that three different hole polarons in the β-phase and six different hole polarons in the κ-phase could exist.

Indeed, in a preliminary analysis using the PBE functional (but the neutral cell approach, so that the functional dependence is reduced), we find different hole polarons in both phases. To stabilize the polaron at sites with different symmetry (i.e., at different Wyckoff positions or same Wyckoff position but inequivalent atoms), we initially distort randomly the surrounding atoms of the corresponding site, where we expect distinct meta-stable polarons to be protected by barriers. For β-Ga_2O_3 we find self-trapped hole polarons for the oxygen atoms O2 and O3 (labeling is according to Tab. G.1). The O3 polaron corresponds to the one shown in Fig. 3.11. The KS eigenstate densities of the polarons are shown in Fig. 5.1. We do not find a stable hole polaron at

β-Ga_2O_3

	O1	O2	O3
E_{bind} (eV)	—	-0.61	-0.77
E_0 (eV)	—	1.65	1.78

κ-Ga_2O_3

	O1	O2	O3	O4	O5	O6
E_{bind} (eV)	—	—	-0.82	—	-0.88	—
E_0 (eV)	—	—	1.86	—	2.00	—

TABLE 5.1: The binding energy E_{bind} and the polaron level E_0 for the hole polarons in β- and κ-Ga_2O_3 calculated with the PBE functional and with long-range corection included. For the β phase a $1 \times 3 \times 2$ and for the κ phase a $2 \times 1 \times 1$ supercell has been used. The hyphens indicate that no stable hole polaron localized at a corresponding O atom could be found.

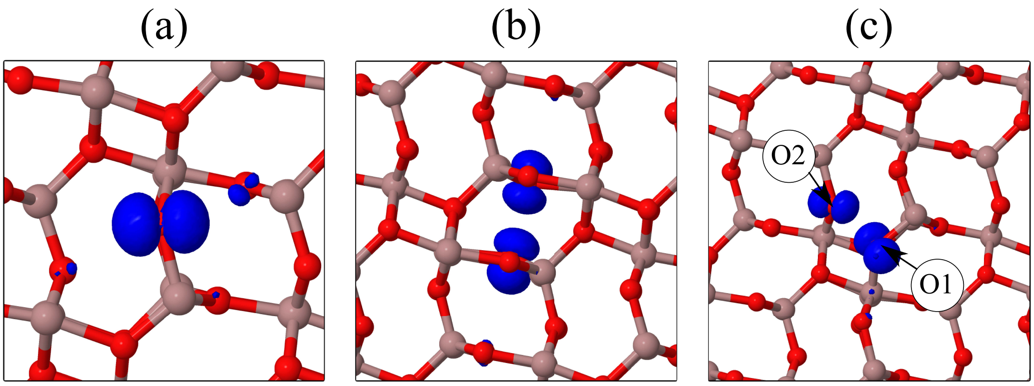

FIGURE 5.1: The KS eigenstate densities for the self-trapped hole polarons in β–Ga_2O_3 at the (a) O2 and (b) O3 atoms. While in (a) the polaron is atom-centered, the polaron in (b) is bond centered and localized on two neighboring O3 atoms. In (c) an interim relaxation step is shown, where the polaron "jumps" from the O1 to O2 atom. The polarons are simulated with the PBE functional in a $1 \times 3 \times 2$ supercell. The point of view is along the b axis.

the O1 atom. Instead, we observe during interim relaxation steps that the charge density originally localized at the O1 atom jumps to an O2 atom, cf. Fig. 5.1(c). A plausible reason why we did not find the O1 polaron is the position of band extrema of the O1 bands within the valence bands. Pronounced peaks in the DOS are indicating band extrema with a high band mass and, thus, a strong el-ph coupling according to the Fröhlich coupling constant Eq. (1) can be expected. The analysis of the atom-projected DOS unveils that the O1 atom contributes least to the VBM and has its largest contribution $\sim$1 eV below the VBM, cf. Fig. 5.2. Due to their lower energies, bands of the O1 atoms coupling to LO phonon modes are leading to a shallower polaron level and, consequently, to an increased binding energy according to Eq. (2.18)[1]. Assuming a similar coupling for the O1 polaron as for the O2 or O3 polaron, the binding energy would be increased by 1 eV just due to the position of the O1 electronic band and, with this, not stable anymore. The position of the bands might be sensitive to the used XC functional and, therefore, we will investigate this as function of the exact exchange in the HSE functional in future work. However, the total valence band width of 7.37 eV obtained from photo-emission spectra of β-Ga_2O_3 at room temperature [151] is already in good agreement with the PBE band width of 7.1 eV (corresponding to $T = 0$ K). Therefore, we do not expect qualitative changes in stability of the polaron at the O1 atom when computed with a different functional. Another interesting fact is that the polarons at O2 and O3 show different kinds of localization: while O2 is atom-centered, we find at the O3 atom a bond-centered polaron, where the polaron mainly localizes between two neighboring O3 atoms. It is often assumed that only one kind of polaron exists for a certain material. However, our analysis indicates that due to their

[1]According to our convention an increased binding energy refers to less stable polaron.

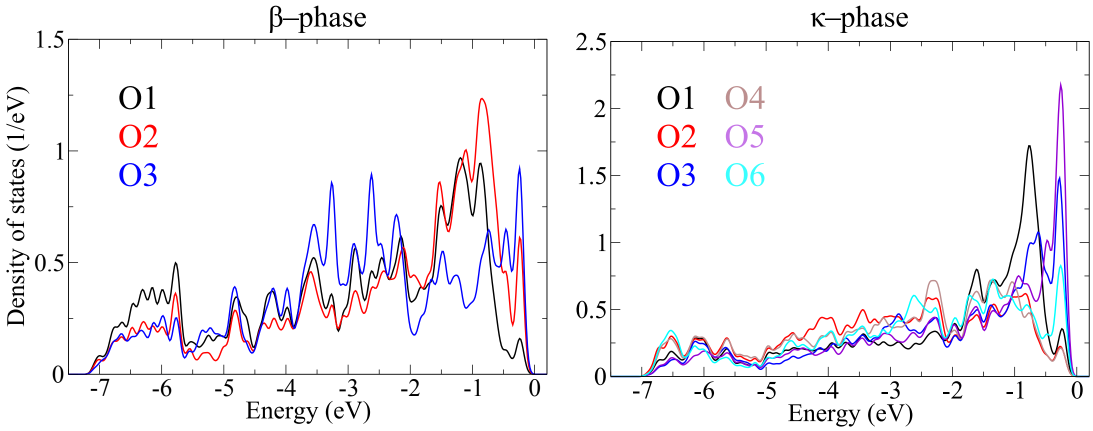

FIGURE 5.2: The density of states of pristine β– and κ–Ga_2O_3 projected on the oxygen atoms of different site symmetries calculated with the PBE functional. The labeling of the atomic positions is as given in Tab. G.1. The energy zero was shifted to the VBM.

different structural environments, the O2 and O3 atoms accommodate chemically different small polarons. The finite-size corrected polaron binding energies and levels calculated with the PBE functional are summarized in Tab. 5.1.

For the κ–phase we could find so far only two stable out of six possible small hole polarons. Again, this is in good agreement with the contribution of the different oxygen atoms to the VBM. We find that the O3 and O5 atoms, that are the oxygen atoms where we could find trapped hole polarons, contribute most to the VBM, whereas the O1, O2, and O4 contribute least and have their largest peaks in the DOS at around 1 eV below the VBM. More uncertain is the analysis of the DOS w.r.t. the O6 atom having a main peak at the VBM as well (but less pronounced). More different initial configurations for the O6 site have to be used in order to decisively exclude the trapping of hole polarons at this site. Additionally, due to the deep polaron levels of the trapped hole polaron we found so far, the simulation with the PBE functional suffers from the clearly underestimated band gap, that is, 2 eV for PBE band gap compared to 4.9 eV measured in experiments. This problem is particularly severe for the κ phase, suggesting that polaron levels may be found at higher energies with a better electronic-structure method.

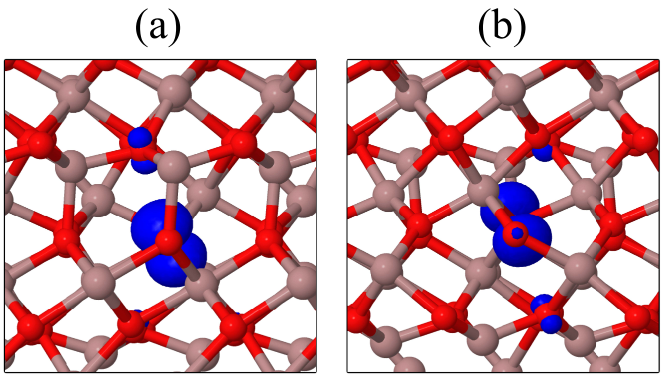

FIGURE 5.3: The KS eigenstate densities for the self-trapped hole polarons in κ Ga_2O_3 at the (a) O3 and (b) O5 atoms. Both polarons are atom-centered. The point of view is along the b axis.

Appendix A

Homogeneous electron gas

The homogeneous electron gas (HEG) is a simple model system, e.g., for metals, which will be used here to demonstrate important concepts in the field of solid-state physics. It is assumed that the ground-state density of the electrons as well as the nuclei is uniformly distributed in a unit cell with volume Ω, and lattice vectors $\boldsymbol{a}$, $\boldsymbol{b}$, $\boldsymbol{c}$ and reciprocal lattice vectors $\boldsymbol{a}^*$, $\boldsymbol{b}^*$, $\boldsymbol{c}^*$. In order to simulate a solid we use Born-von Karman (BvK) boundary conditions, i.e., the unit cell is repeated L-times in each spatial direction, where the states should fulfill $\psi\left(\boldsymbol{r}+L\boldsymbol{a}\right)=\psi\left(\boldsymbol{r}\right)$ and equally for $\boldsymbol{b}$ and $\boldsymbol{c}$ directions. Due to the periodic arrangement, the Hamiltonian $\hat{H}$ has the same periodicity, too, and from the Bloch theorem follows that any eigenfunction ψ must have the form:

$$\psi_{\boldsymbol{k}}(\boldsymbol{r})=\mathrm{e}^{i\boldsymbol{k}\boldsymbol{r}}u_{\boldsymbol{k}}(\boldsymbol{r}) \tag{A.1}$$

As a consequence of the BvK boundary conditions, the states ψ are described by quantum numbers $\boldsymbol{k}_i$:

$$\boldsymbol{k}_i=\frac{n_{a_i}}{L}\boldsymbol{a}^*+\frac{n_{b_i}}{L}\boldsymbol{b}^*+\frac{n_{c_i}}{L}\boldsymbol{c}^*,\; n_x=0,1,\ldots,L-1 \tag{A.2}$$

within the first Brillouin zone (BZ).

A.1 Non-interacting electrons

The Hamiltonian of the non-interacting HEG is just described by the kinetic operator:

$$\hat{H}\left|\psi\right\rangle=-\frac{\hbar^2}{2m}\nabla^2\left|\psi\right\rangle=\epsilon\left|\psi\right\rangle \tag{A.3}$$

and by plugging Eq. (A.1) the solution is simply given by plane waves:

$$\psi_{\boldsymbol{k}_i}(\boldsymbol{r})=\frac{1}{\sqrt{\Omega}}\mathrm{e}^{i\boldsymbol{k}_i\boldsymbol{r}} \tag{A.4}$$

with the energy:

$$\epsilon_{\boldsymbol{k}_i} = \frac{\hbar^2 k_i^2}{2m} \tag{A.5}$$

The total energy per non-interacting electron is given by:

$$E/N \equiv e(n) = \frac{\hbar^2}{2m}\frac{3}{5}(3\pi^2 n)^{\frac{2}{3}} \tag{A.6}$$

A.2 The Hartree-Fock approximation for the HEG

The purpose of this section is twofold. Fist, we introduce the approximation proposed by Fock, whose equations are used for the computation of the exact exchange energy of solids. Second, we derive the exchange energy of the HEG, which is important for functionals such as LDA and GGA.

The idea of Hartree was to start with a simple form of the wave function. He derived single particle equations with the following *ansatz* for total wave function for N electrons (we ignore the spin degrees of freedom, since none of the operators considered below is acting on them):

$$\Psi_{\mathrm{H}}(\boldsymbol{r}_1, \boldsymbol{r}_2, \ldots, \boldsymbol{r}_N) = \phi_1(\boldsymbol{r}_1)\phi_2(\boldsymbol{r}_2)\ldots\phi_N(\boldsymbol{r}_N) \tag{A.7}$$

Fock additionally enforced the proper symmetry for the fermionic wave function by building a Slater determinant:

$$\Psi_{\mathrm{HF}} = \frac{1}{N!}\begin{vmatrix} \phi_1(\boldsymbol{r}_1) & \phi_2(\boldsymbol{r}_1) & \ldots & \phi_N(\boldsymbol{r}_1) \\ \vdots & \vdots & \ddots & \vdots \\ \phi_1(\boldsymbol{r}_N) & \phi_2(\boldsymbol{r}_N) & \ldots & \phi_N(\boldsymbol{r}_N) \end{vmatrix} \tag{A.8}$$

The idea of Hartree and Fock was to find the best wave function of the form Ψ_{HF} by the variation of the total energy Eq. (1.15) (we follow Ashcroft and Mermin):

$$\delta \langle \hat{H} \rangle_{\Psi_{\mathrm{HF}}} = 0 \tag{A.9}$$

with respect to the single-electron orbital ϕ_i^*. As a result, we obtain the (canonical) Hartree-Fock equations:

$$-\frac{\hbar^2}{2m}\nabla^2\phi_i(\boldsymbol{r}) - \sum_j \int \mathrm{d}\boldsymbol{r}' \frac{e^2}{|\boldsymbol{r}-\boldsymbol{r}'|}\phi_j^*(\boldsymbol{r}')\phi_i(\boldsymbol{r}')\phi_j(\boldsymbol{r}) = \epsilon_i\phi_i(\boldsymbol{r}) \tag{A.10}$$

Assuming that the ground state is homogeneous, it can be shown that the eigenstates are plane waves, too. Substituting the Fourier transform of the second term:

$$\frac{e^2}{|\boldsymbol{r}-\boldsymbol{r'}|} \to 4\pi e^2 \int \frac{\mathrm{d}\boldsymbol{q}}{(2\pi)^3}\frac{1}{q^2}\mathrm{e}^{i\boldsymbol{q}(\boldsymbol{r}-\boldsymbol{r'})} \tag{A.11}$$

into Eq. (A.10), one can obtain (c.f. Ashcroft/Mermin, p. 334 for details):

$$\begin{aligned}\epsilon(\boldsymbol{k}) \quad &= \frac{\hbar^2 k^2}{2m} - 4\pi e^2 \int_{\boldsymbol{k}<\boldsymbol{k'}} \frac{\mathrm{d}\boldsymbol{k'}}{(2\pi)^3}\frac{1}{|\boldsymbol{k}-\boldsymbol{k'}|^2} \\ &= \frac{\hbar^2 k^2}{2m} - \frac{2e^2 k_F}{\pi} F\left(\frac{k}{k_f}\right)\end{aligned} \tag{A.12}$$

with the function:

$$F(x) = \frac{1}{2} + \frac{1-x^2}{4x}\ln\left|\frac{1+x}{1-x}\right|. \tag{A.13}$$

Finally, we give the important result of the total energy in the Hartree-Fock approximation per electron:

$$\begin{aligned}e_{\mathrm{HF}}(n) \quad &= t_s(n) + e_{\mathrm{x}}(n) \\ &= \frac{3}{5}\frac{\hbar^2}{2m}(3\pi^2 n)^{\frac{2}{3}} - \frac{3}{4}\frac{e^2}{\pi}(3\pi^2 n)^{\frac{1}{3}},\end{aligned} \tag{A.14}$$

which includes the exchange energy e_x of the HEG:

$$e_{\mathrm{x}} = -\frac{3}{4}\frac{e^2}{\pi}(3\pi^2 n)^{\frac{1}{3}}, \tag{A.15}$$

and the kinetic energy of the non-interacting electrons:

$$t_{\mathrm{s}} = \frac{3}{5}\frac{\hbar^2}{2m}(3\pi^2 n)^{\frac{2}{3}} \tag{A.16}$$

A.2.1 Fully interacting HEG

To summarize what we have so far, we write down all terms calculated previously:

$$e(N) = t_{\mathrm{s}}(n) + e_{\mathrm{x}}(n) + e_{\mathrm{c}}(n), \tag{A.17}$$

where we have collected the remaining unknown terms in $e_c(n)$, the so-called correlation energy, which is defined formally by:

$$e_{\mathrm{c}}(n) = t(n) - t_{\mathrm{s}}(n) + e_{\mathrm{ee}}(n) - e_{\mathrm{x}}(n). \tag{A.18}$$

where $t(n)$ is the kinetic energy of the interacting electrons and $e_{\mathrm{ee}}(n)$ the energy of the electron-electron interaction as introduced in Eq. (1.2). The evaluation of e_{c} is challenging even for the HEG, and a closed analytical expression as for the exchange energy cannot be found. However, due to work by Ceperley and Alder, who computed the correlation energy using quantum Monte Carlo method, a very accurate parameterization of e_{c} exists. Most prominent parameterizations for recent density-functional software codes are Perdew and Zunger, or Vosko-Wilkes-Nusiar. A very recent and simple, but on the same side accurate parametrization was suggested by Chachiyo (2016). Here, we give just the one proposed by Perdew and Zunger (PZ), which is used in case of LDA calculations in our work:

$$e_{\mathrm{c}}^{\mathrm{PZ}}(r_s) = \begin{cases} -0.0480 + 0.031\ln(r_s) - 0.0116 r_s + 0.0020 r_s \ln(r_s), & r_s < 1 \\ -0.1423/(1 + 1.0529\sqrt{r_s} + 0.3334 r_s), & r_s > 1, \end{cases} \tag{A.19}$$

where r_s denotes the radius of sphere containing one electron of the HEG and is related to the density n as $r_s = [\frac{3}{4\pi}\frac{me^2}{\hbar^2}\frac{1}{n}]^{1/3}$.

Appendix B

The Freysoldt *et al.* correction scheme

An important part of the developed method is the correction of finite-size effects for supercell calculations. For completeness we present the main ideas of the correction scheme proposed by Freysoldt *et al.*[99, 103]. Starting point is the simulation of a charged point defect in an otherwise pristine crystal causing a localized excess-charge distribution ρ. It is assumed that for a sufficiently large supercell the quantum nature of the defect is simulated properly and only long-ranged interactions affect the defect potential in neighboring cells. For simplicity, Freysoldt *et al.* suggest to model ρ with a simple isotropic function ρ_{model}, such as an exponential or a Gaussian (the fitting of ρ_d by ρ_{model} is demonstrated in App.C). The actual detailed excess-charge distribution is not necessary to know and would change the correction only negligibly. As Freysoldt *et al.* note in their original paper, it is not even important to imitate the proper localization of ρ as long as the distribution is well-localized within the supercell. With this, it is possible to evaluate the lattice sum of the long-range potential (i.e., the potential energy due to the periodic arrangement of the defects):

$$E_{\text{latt}} = \frac{1}{\Omega} \sum_{\mathbf{G} \neq \mathbf{0}} V^{\text{lr}}(\boldsymbol{G}) q_{\text{model}}(\boldsymbol{G}) \,, \tag{B.1}$$

where $V(\boldsymbol{G})$ is the Fourier-transform of the long-range potential, and the sum runs over all reciprocal lattice vectors $|\boldsymbol{G}| < G_{\text{cut}}$. The cut-off G_{cut} has to be chosen carefully to ensure convergence of the sum. Eq. (B.1) is the artificial energy, which has to be removed (e.g., from the polaron binding energy or level), the energy of the isolated defect has to be added. The latter is easily calculated by:

$$E_{\text{iso}} = \frac{1}{(2\pi)^3} \int V^{\text{lr}}(\boldsymbol{k}) q_{\text{model}}(\boldsymbol{k}) \mathrm{d}\boldsymbol{k} \,, \tag{B.2}$$

and the total correction is given by $E_{\text{corr}} = E_{\text{latt}} - E_{\text{iso}}$. To obtain the desired energy in the dilute limit E_{∞}, the correction $E_{\text{corr}}(\Omega)$ has to be applied to the energy $E(\Omega)$ calculated in the supercell of size Ω:

$$E_{\infty} = E(\Omega) - E_{\text{corr}}(\Omega) + q\Delta V. \tag{B.3}$$

The last term $q\Delta V$ is the so-called alignment term. It appears for two reasons. First, $E(\Omega)$ is usually calculated with respect to a reference system, often the pristine bulk system. Due to defect or the charge there might be difference in the potentials for the defect system and the pristine system even far away from the defect center. This difference can be removed by aligning the electrostatic potentials (or Hartree potentials). Second, the absolute magnitude of the long-range potential calculated from ρ_{model} might not be equal to the one from the original ρ. This difference must be also removed. The term $q\Delta V$ is the correction accounting for these two contributions.

Appendix C

Pekar's polaron and its relation to KS eigenstates

The objective of this appendix is to show how we connected the analytical polaron model of Pekar with the actual many-electron problem treated with DFT. In particular, the relation of the electronic part of the polaron wave function to the highest occupied (ho) or lowest unoccupied (lu) KS state is discussed below.

Pekar's polaron model [7] can be derived from the Fröhlich Hamiltonian [8] in the adiabatic static strong-coupling limit, as was shown for example by Devreese [89] (cf. also references therein for original work). In this limit, assuming adiabatic separation of the ionic and electronic dynamics, the potential of the electron-phonon interaction has the form (here it is shown in real space and not its Fourier transform as in Eq. (2.9)):

$$V_{\text{el-ph}}(\boldsymbol{r}) = -\frac{1}{\kappa}\int \frac{\rho(\mathbf{r}')}{|\mathbf{r}-\mathbf{r}'|} d^3r' \,, \tag{C.1}$$

which is the classical response of a polar dielectric to an extended excess charge distribution $\rho(\mathbf{r})$. Due to the adiabatic limit the el-ph potential in Eq. (C.1) depends only on the electron coordinates. The inverse dielectric constant $\kappa^{-1} = \varepsilon_\infty^{-1} - \varepsilon_0^{-1}$ describes the polarization of the rigid ions in the medium by the electron or hole. For simplicity, here we assume an excess electron in an isotropic medium (the dielectric response is described by a single constant).

Let us regard Eq. (C.1) as a perturbation of the perfect (undistorted) system H_{perf} – the single-particle KS Hamiltonian of the system where an additional electron has been placed at the bottom of the conduction band minimum (CBm) ϕ_{CBm} with energy ϵ_{CBm}:

$$H_{\text{perf}}\phi_{\text{CBm}} = \epsilon_{\text{CBm}}\phi_{\text{CBm}} \tag{C.2}$$

Following the Kohn-Luttinger perturbation theory [152] the solution of:

$$(H_{\text{perf}} + V_{\text{el-ph}})\Psi = \epsilon\Psi \tag{C.3}$$

in first order is given by:

$$\begin{aligned} \epsilon &= \epsilon_{\text{CBm}} + E_0 \\ \Psi &= \phi_{\text{CBm}}\Phi \end{aligned} \tag{C.4}$$

where E_0 and Φ are obtained from the solution of the effective Hamiltonian [152]:

$$\begin{aligned} (H_{\text{kin,eff}} + V_{\text{el-ph}})\Phi &= E_0\Phi \\ \left(-\frac{\nabla}{2m^*} - \frac{1}{\kappa}\int \frac{|\Phi(\mathbf{r}')|^2}{|\mathbf{r}-\mathbf{r}'|}d^3r'\right)\Phi(\mathbf{r}) &= E_0\Phi(\mathbf{r})\,, \end{aligned} \tag{C.5}$$

with the effective mass m^* from the CBm. With Eq. (C.5) we recover the original problem of Pekar's polaron, with E_0 being the energy of the bound (polaron) state relative to the conduction-band edge for the case of an electron polaron.

Eq. (C.5) does not contain microscopic details. However, it can be regarded as describing the asymptotic el-ph interaction far away from the localized part of the excess electron charge distribution. According to Eq. (C.4), $\Phi(\mathbf{r})$ represents the envelop of the original electronic state ϕ_{CBm} and in this work is assumed as exponentially decaying function ρ_{model}, cf. Eq. (2.13). The electron KS eigenstate $\phi_{\text{lu}}^{\text{DFT}}$ corresponding to $\epsilon_{\text{lu}}(N)$ in the DFT calculation at the *distorted* (polaron) geometry is the polaron wave function Ψ. Thus, in an infinite extended crystal with a single polaron the envelop of $\phi_{\text{lu}}^{\text{DFT}}$ shows the localization of $\rho(\boldsymbol{r})$ needed for the correction scheme Eq. (2.11). However, for the supercell approach we have a superposition of polaron densities changing slightly the actual polaron radius. Therefor, in our correction model we use a superposition of $\rho_{\text{model}}(\boldsymbol{r})$ for each of the neighboring supercells as well to estimate the polaron radius. An example of the polaron KS eigenstate density $\rho(\boldsymbol{r})$ calculated with the PBE functional and the fitted envelope $\rho_{\text{model}}(\boldsymbol{r})$ is shown in Fig. 2.4 (a) and (b) for MgO and TiO_2, respectively.

C.1 Pekar's 1:2:3:4 theorem

For our correction scheme, we derived in Sec. 2.1 the proper long-range el-ph potential. However, the binding energy and the polaron level as a function of the supercell do show different slopes (cf. Fig. 2.3) indicating a different dependence on the el-ph interaction potential on the supercell size. The ratio of the slopes is obtained using the theorem introduced in this section. The result is used to correct the polaron level.

For arbitrary coupling constants in the Fröhlich Hamiltonian:

$$H_{\text{Fröhlich}} = H_{\text{kin,eff}} + H_{\text{ph}} + V_{\text{el-ph}}, \tag{C.6}$$

with the Hamiltonian of the phonons H_{ph}, it has been shown [111] that there exist fixed ratios of the effective kinetic energy $E_{\text{kin,eff}}$, lattice distortion (phonon field) energy $\Delta E^{\text{polaron}}$, the polaron state energy E_0, and the electron-phonon interaction energy $E_{\text{el-ph}}$:

$$E_{\text{kin,eff}} : \Delta E^{\text{polaron}} : -E_0 : -E_{\text{el-ph}} = 1 : \eta(\alpha_F) : 3 : 4\,, \tag{C.7}$$

where η depends on the value of Fröhlich coupling constant α_{F}. In the limit of strong electron-phonon coupling (i.e. where the adiabatic approximation is reasonable), the polaron energy is dictated by the polarization of the lattice, and η approaches 2. From this it follows:

$$E_{\text{bind}} = E_{\text{kin,eff}} + \Delta E^{\text{polaron}} + E_{\text{el-ph}} = E_{\text{kin,eff}} + \frac{1}{2}E_{\text{el-ph}} \tag{C.8}$$

$$E_0 = E_{\text{kin,eff}} + E_{\text{el-ph}} \tag{C.9}$$

Eqs. (C.8) and (C.9) clearly show the dependence of the binding energy and the polaron level on the energy of the el-ph interaction. The latter energy is the one that remains to be corrected for the artificial supercell interactions, and thus the correction for the polaron level has to be twice the correction for the binding energy, which leads to Eq. (2.24).

However, the ratios Eq. (C.7) are only based on an effective single-particle model (Eq. (C.5)). In our microscopic (DFT) model, additional (short-range) contributions to the energy components and variations of $\eta \leq 2$ lead to violation of the above ratios. In particular for TiO_2 the ratios are not preserved.

Appendix D

The electronic properties of rocksalt MgO

D.1 The electronic structure

For the sake of completeness we report the electronic structure of rocksalt MgO. The band structure shown in Fig. D.1 has been computed with the PBE functional with a lattice constant of a = 4.211 Å[1]. MgO has a direct band gap with an isotropic minimum at Γ for the conduction band with a small band mass of $m_b = 0.35 m_e$. On the contrary, the valence bands exhibit an anisotropic maximum with high band masses for the hole of $m_b = 2.0...5.4 m_e$. The high band mass for the holes leads to a strong coupling to the LO modes and in turn to the formation of a small polaron.

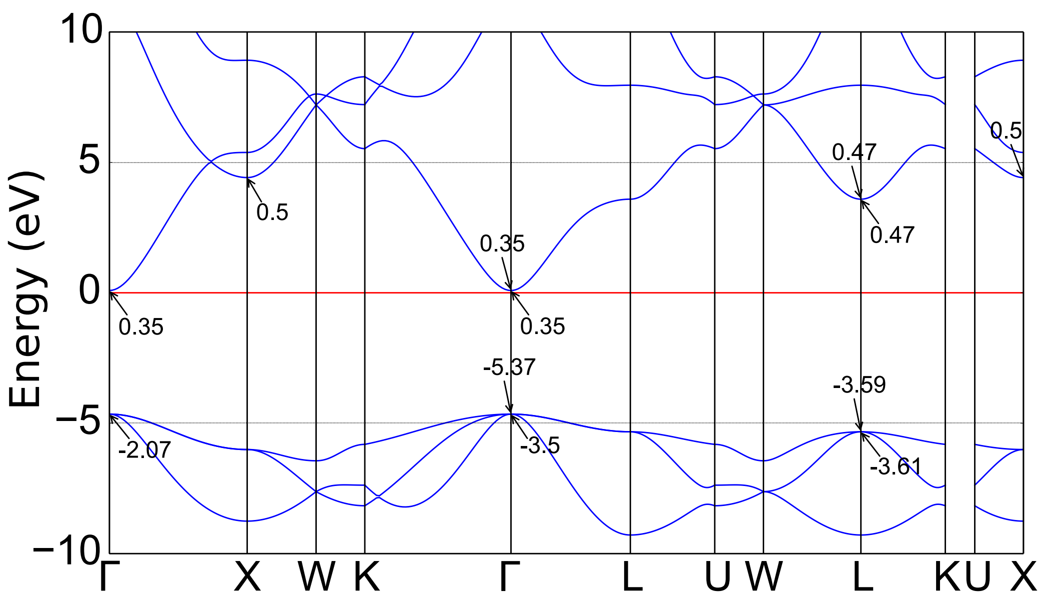

FIGURE D.1: Band structure of rocksalt MgO calculated with PBE. Band masses (in units of electron mass) at particular extrema are shown.

[1]This is the equilibrium lattice constant of MgO calculated with HSE(α=0.25), which is used for all calculations of MgO in this thesis.

D.2 The high-frequency dielectric constants for functionals including exact exchange

A straightforward way of obtaining ε_∞ is to determine the coefficients in Eq. (2.1) for several supercell sizes of a structure including a localized excess charge distribution without relaxing atomic positions. For this purpose we calculated the formation energy of the unrelaxed singly-charged oxygen vacancy. We obtained $\varepsilon_\infty = 2.4$ from the fit, as shown in Fig. D.2(a). For a general understanding of the importance of the local field effects for functionals including exact exchange [50] we plotted ε_∞ as a function of the fraction of exact exchange in the HSE functional for rock salt MgO, shown in Fig. D.2(b).

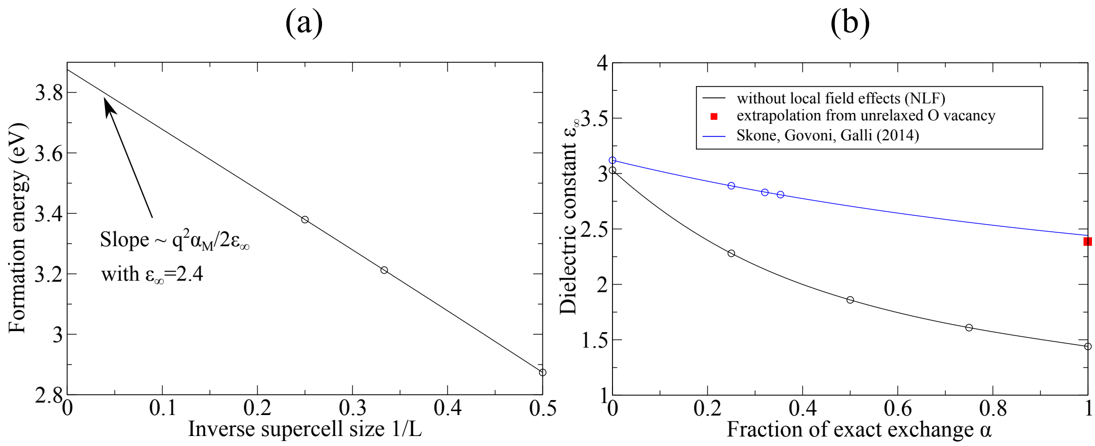

FIGURE D.2: (a) The formation energy of the unrelaxed singly-charged oxygen vacancy in MgO calculated with HSE(α=1.0). For large supercell sizes the slope of the line approaches $q^2\alpha_{\mathrm{M}}/2\varepsilon_\infty$, where α_{M} is the Madelung constant (α_{M} = 2.8373 for MgO), and q is the charge of the defect ($q = 1$ in our case). By determining the coefficients in Eq. (2.1) we find $\varepsilon_\infty = 2.4$. (b) Comparison of ε_∞ calculated with (blue line) and without local field (no local field, NLF) effects (black line). The values with local field effects included are obtained from Ref. [50] – and the values without are calculated according to Ref. [153] as implemented in the FHI-aims code. The result from (a) is indicated by the red square.

Appendix E

Convergence tests for the polaron in MgO

E.1 Comparing *light* and *tight* settings in FHI-aims

For the smallest used supercell of MgO containing 216 atoms in our polaron study we compare different standard settings of FHI-aims, namely the change in energies between *light* and *tight* settings, where *light* and *tight* settings refer to numerical standard parameters for the integration grid, basis set, and convergence criteria. All values are given in eV. As a result we see that the binding energies are shifted by about $+0.02$ eV. So, we conclude that *light* settings are sufficient to demonstrate the effect of polaron trapping.

	PBE			HSE(α=1)		
	$\Delta E^{\text{polaron}}$	E_0	E^0_{bind}	$\Delta E^{\text{polaron}}$	E_0	E^0_{bind}
light	0.630	0.644	-0.014	0.703	0.768	-0.065
tight	0.637	0.612	0.025	0.711	0.758	-0.048

TABLE E.1: The relaxation energy $\Delta E^{\text{polaron}}$, the polaron level E_0, and the polaron binding energy E^0_{bind} calculated with different numerical settings (*light* and *tight*) and different functionals for the fixed geometry optimized with the PBE functional.

E.2 Geometry optimization with PBE

Here, we show that the geometry optimization using the method of Sadigh *et al.* [108] introduced in Sec. 2.2.2 is sufficient, if carried out only with the PBE functional. It will be tested for the $3\times3\times3$ supercell of MgO including 216 atoms. We compare structures relaxed with PBE and HSE06($\alpha = 1.0$) using forces computed from the $\Delta E^{\text{polaron}} - E_0$ potential-energy surface, as well as from the usual $E(N-1)$ potential-energy surface calculated with HSE06($\alpha = 0.4$). For each of these different structures we perform a

Functional, Method	E^0_{bind} (eV)	E_0 (eV)	RMSD (Å)	Max. Dev. (Å)
HSE(α=0.4), conv.	-0.109	1.045	0.0000	0.000
PBE, Sadigh	-0.064	0.768	0.0040	0.028
HSE(α=1.0), Sadigh	-0.111	1.027	0.0023	0.015

TABLE E.2: The polaron binding energy E^0_{bind} and the polaron level E_0 computed as a function of the geometry optimized with different functionals and force evaluations. In the conventional approach (conv.) the forces are calculated as derivatives of $E(N-1)$ and in the Sadigh approach as derivatives of $E(N) - \epsilon_{\text{ho}}(N)$. In the two last columns a measure for the deviations of the geometries w.r.t. the first row is given, namely the RMSD and the maximum deviation of a single atom.

single-point calculation with HSE06($\alpha = 1.0$) to estimate the largest differences with this functional. The geometry from the conventional optimization is used as reference for *root mean square deviation* (RMSD) of the atomic positions:

$$\text{RMSD} = \sqrt{\frac{1}{N}\sum_i (\boldsymbol{x}_i - \boldsymbol{y}_i)^2} \tag{E.1}$$

E.3 Supercell convergence of the polaron geometry

In a solid, the long-range response to an excess charge involves a large number of atoms, so that even small displacements of the atoms far from the charge add up to a significant contribution to the PES of the polaron. However, in a supercell the displacements are limited to a finite volume. Figure E.1 shows the sensitivity of the displacements for the optimized polaron geometry in a $3\times3\times3$ MgO supercell compared to a $5\times5\times5$ supercell. In general, it can be observed that while the absolute value of the displacements decreases fast with the distance to the polaron center, their contribution to the polaron energy ($\sim \Delta R \cdot R^2$) is long-ranged and strongly depends on the supercell size, as illustrated in Fig. E.1. Thus, this contribution and, consequently, polaron properties converge very slowly with the supercell size, as we have already pointed out, cf. Fig. 2.3. However, as we demonstrate in this thesis, there is no need to explicitly treat the atomic displacements at long range in the dilute limit, since the finite-size effects can be accounted for via a simple physical model of the long-range response, provided the supercell size is large enough to explicitly include the remaining, more complex but also more localized effects. Indeed, as shown in Tab. E.3, the polaron radius obtained from the KS eigenstate density is smaller than the size of the smallest supercell we have considered, and is only weakly dependent on the size for larger supercells.

The proper asymptotic behavior of the atomic displacements for a polaron in the dilute limit can be estimated as follows. For small displacements the polarization at atom κ due to the displacement $\boldsymbol{u}_\kappa$ is given as $\boldsymbol{P} = \frac{e\boldsymbol{Z}_\kappa \boldsymbol{u}_\kappa}{\Omega_0}$ with the Born effective charge tensor $\boldsymbol{Z}_\kappa$, and the unit cell size Ω_0. The source of the polarization of the atoms is the el-ph potential determining the displacements as a function of the distance from the polaron center $\boldsymbol{u}_\kappa = \boldsymbol{u}_\kappa(\boldsymbol{R})$. The asymptotic behavior of the el-ph potential $V_{\text{el-ph}}$ is described by Eq. (C.1). It is related to the polarization as $\boldsymbol{P} \sim \boldsymbol{\nabla} V_{\text{el-ph}}$. Assuming a strong localization of the polaron (electron) density $\rho(r) \sim \delta(0)$, we obtain $\boldsymbol{P} \sim \boldsymbol{u}_\kappa(\boldsymbol{R}) \sim \boldsymbol{R}/R^3$. Thus, the product $\Delta R \cdot R^2$ should approach a constant, which is depicted as black dotted line in Fig. E.1 for the oxygen atoms. But in a finite supercell, the displacements of the atoms far away from the polaron center decrease faster than $1/R^2$ (see Fig. E.1), which is the effect of the periodic boundary conditions.

supercell size	polaron radius (Å)
$3 \times 3 \times 3$	1.861
$4 \times 4 \times 4$	1.634
$5 \times 5 \times 5$	1.638

TABLE E.3: The radius of the polaron in MgO as a function of the supercell size obtained by fitting the envelop of the KS eigenstate density (calculated with the PBE functional). The $3 \times 3 \times 3$, $4 \times 4 \times 4$, and $5 \times 5 \times 5$ supercells contain 216, 512, and 1000 atoms, respectively.

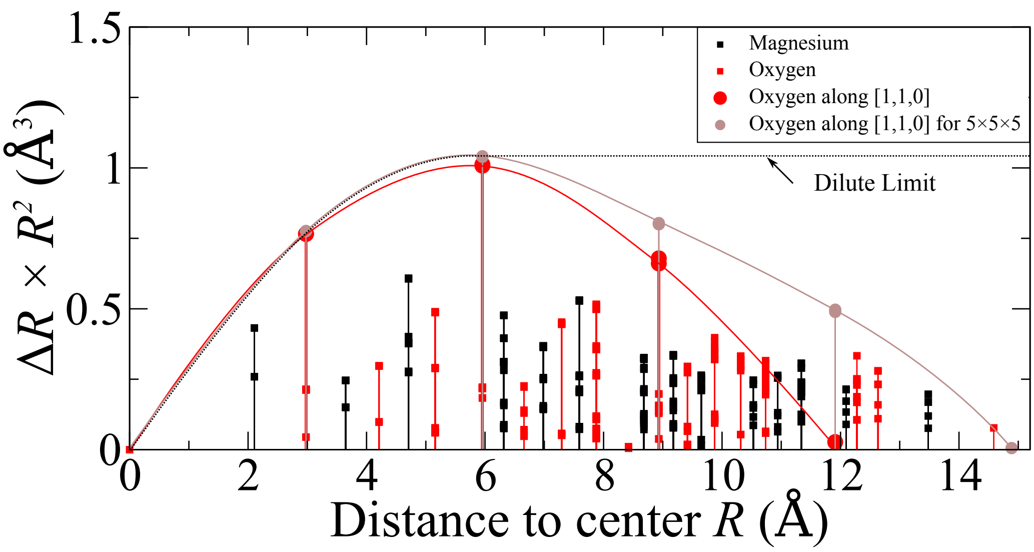

FIGURE E.1: The displacements ΔR times the squared distance to the polaron center R^2 for the Mg (black squares) and O (red squares) atoms in a $3 \times 3 \times 3$ MgO supercell at the optimized polaron geometry, obtained using the approach of Sadigh *et al.* [108] presented in Sec. 2.2.2. The largest displacements can be observed for the oxygen atoms along the [1,1,0] direction (red circles connected by the red line). For comparison, the O displacements along the same direction are shown for the $5 \times 5 \times 5$ supercell (brown circles). The displacements should approach the black dotted line in the dilute limit.

E.4 Dependence of the polaron radius on the fraction of exact exchange

In order to check the dependence of the polaron radius obtained by fitting the KS eigenstate density we optimized the geometry for $\alpha = 0.0, 0.5, 1.0$ (cf. Fig. E.2) according to the approach by Sadigh *et al.* [108] presented in the manuscript, cf. Sec.2.2.2. We find only a small variation of the radius, which is in line with the calculated energy differences in the polaron binding energy and the polaron level as fraction of exact exchange obtained with our approach, cf. Fig. 2.3.

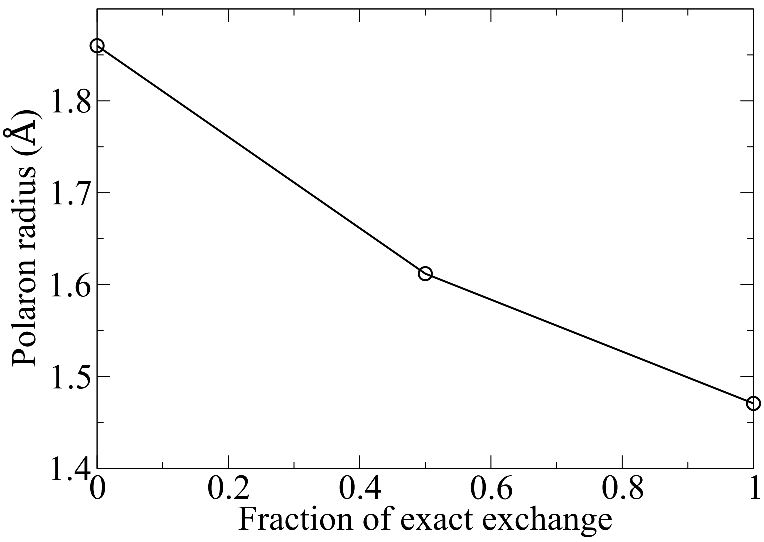

FIGURE E.2: The polaron radius fitted as the envelop of the KS eigenstate density for three different fractions of exact exchange in the HSE functional.

Appendix F

Properties of rutile and anatase TiO_2

F.1 Rutile TiO_2

(a) Lattice parameters

	a (Å)	c (Å)
PBE	4.650	2.982
Expt. [154]	4.594	2.959

(b) Atomic coordinates

	Ti1	O1
$\boldsymbol{a}$	0.0	0.3045106
$\boldsymbol{b}$	0.0	0.3045106
$\boldsymbol{c}$	0.0	0.0437906

TABLE F.1: Structural properties of the rutile phase obtained from the optimization with the PBE functional. The lattice parameters of Ref. [154] are measured at T=30°C and ambient pressure, where the PBE results refer to T=0 K (without zero-point effects). The atomic coordinates in (b) are given in fractional coordinates of the lattice vectors $\boldsymbol{a}$, $\boldsymbol{b}$, and $\boldsymbol{c}$.

With PBE we find a crystal structure with slightly reduced symmetry corresponding to the space group $P4_2nm$ (space group number 102). The position of the O1 atom for $P4_2nm$ can be represented by two parameters u and v as (u, u, v) However, in experiments the space group $P4_2/mnm$ (space group number 136) is found. The difference can be observed for the z coordinate of the O1 atom: for perfect rutile $v = 0.0$. The energy difference between this two configurations, that is $v = 0.0$ and $v = 0.043906$ calculated with PBE is 15 meV and, thus, rather small. Further, we investigate the dependence of the u and v parameters obtained with HSE06(α) on the fraction of exact exchange α. The lattice constants are kept fixed at the PBE values (see Tab. F.1). The result is shown in Fig. F.1. We observe an abrupt change between $\alpha = 0.5$ and $= 0.75$, where the system's symmetry changes abruptly to the space group $P4_2/mnm$, since $v = 0.0$ for $\alpha = 0.75$. Similarly, using PBE+U with U=7.5 for the 3d orbital of the Ti atom results in the optimized structure of $P4_2/mnm$ symmetry. For this value of U the calculated KS band gap is close to the experimentally measured optical gap. However, since the changes are small we use the PBE functional for the polaron simulations.

The high-frequency dielectric tensor ϵ_∞ used for the finite-size correction for rutile supercells is calculated with the DFPT formalism at PBE level (for details of implementation cf. Ref [74]), but the tensor of the static dielectric constants ϵ_0 is taken from experiment [155]:

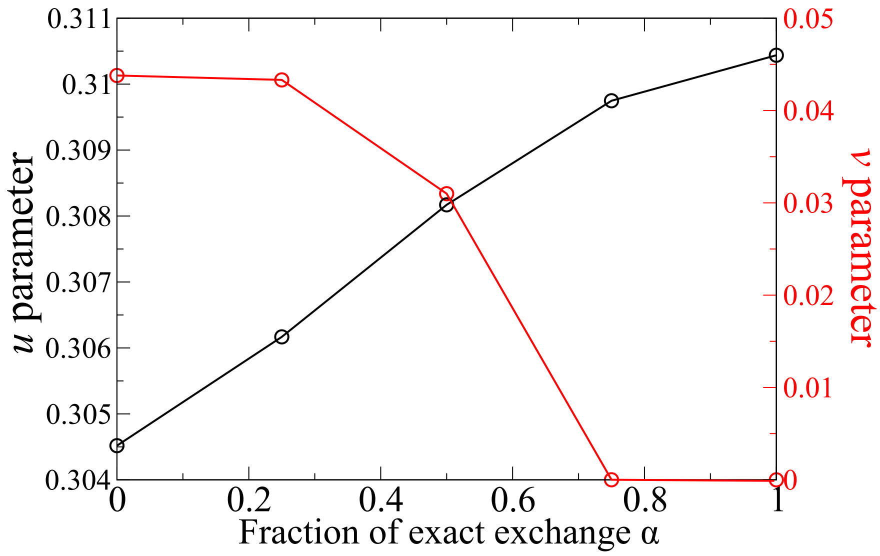

FIGURE F.1: The u (black) and v (red) parameters for rutile TiO_2 determining the position of the O1 atom in the space group $P4_2nm$ as a function of the fraction of exact exchange α in the HSE06 functional.

$$\varepsilon_\infty = \begin{pmatrix} 6.859 & 0 & 0 \\ 0 & 6.859 & 0 \\ 0 & 0 & 8.033 \end{pmatrix} \tag{F.1}$$

$$\varepsilon_0 = \begin{pmatrix} 86 & 0 & 0 \\ 0 & 86 & 0 \\ 0 & 0 & 170 \end{pmatrix} \tag{F.2}$$

The dielectric tensor ε_∞ of rutile obtained from DFPT are in good agreement with experimental findings at room temperature [156] $\varepsilon_\infty = \mathrm{diag}(6.8, 6.8, 8.4)$. Note that in principle ϵ_0 can be calculated within the DFT framework, but we use here the experimental values due to the minor significance of ϵ_0 for the correction scheme. The same consideration is valid for the materials discussed below.

F.2 Anatase TiO_2

(a) Lattice parameters

	a (Å)	c (Å)
PBE	3.80	9.74
Expt. [154]	3.785	9.514

(b) Atomic coordinates

	Ti1	O1
$\boldsymbol{a}$	0.0	0.5
$\boldsymbol{b}$	0.0	0.5
$\boldsymbol{c}$	0.0	0.2941

TABLE F.2: Structural properties of the anatase phase of TiO_2 obtained from the optimization with the PBE functional. The lattice parameters of Ref. [154] are measured at T=28°C and ambient pressure, where the PBE results refer to T=0 K (without zero-point effects). The atomic coordinates in (b) are given in fractional coordinates of the lattice vectors $\boldsymbol{a}$, $\boldsymbol{b}$, and $\boldsymbol{c}$.

Proceeding as for rutile, we get for anatase the following dielectric tensors:

$$\varepsilon_\infty = \begin{pmatrix} 6.74 & 0 & 0 \\ 0 & 6.74 & 0 \\ 0 & 0 & 6.27 \end{pmatrix} \tag{F.3}$$

$$\varepsilon_0 = \begin{pmatrix} 45 & 0 & 0 \\ 0 & 45 & 0 \\ 0 & 0 & 23 \end{pmatrix}, \tag{F.4}$$

where the static dielectric tensor was taken from experiments [12]. Also the dielectric tensor ε_∞ of anatase obtained from DFPT is in reasonable agreement with experimental findings at room temperature [12] $\varepsilon_\infty = \mathrm{diag}(5.8, 5.8, 5.4)$.

Appendix G

Properties of the β– and κ–phase of Ga_2O_3

G.1 β–Ga_2O_3

(a) Lattice parameters

	a (Å)	b (Å)	c (Å)	β
PBE	12.463	3.084	5.877	103.7°
Expt. [157]	12.233	3.038	5.807	103.8°

(b) Atomic coordinates

	Ga1	Ga2	O1	O2	O3
$\boldsymbol{a}$	0.34145	0.08978	0.17372	0.16352	0.49611
$\boldsymbol{c}$	0.18569	0.29479	0.06431	0.60921	0.75685

TABLE G.1: Structural properties of the β-phase of Ga_2O_3 obtained from the optimization with the PBE functional. For all atoms given in (b) $y = 0.0$. The atomic coordinates in (b) are given in fractional coordinates of the lattice vectors $\boldsymbol{a}$ and $\boldsymbol{b}$. The experimental values of Ref. [157] were obtained at ambient temperature and pressure, where the PBE values refer to T=0 K (without zero-point effects).

The high-frequency dielectric tensor $\boldsymbol{\epsilon}_\infty$ used for the finite-size correction is calculated with the DFPT formalism at PBE level (for details of implementation cf. Ref [74]), but the tensor of the static dielectric constants has been approximated by a single constant ϵ_0 and is taken from experiment [158]:

$$\varepsilon_\infty = \begin{pmatrix} 4.02 & 0 & 1 \cdot 10^{-2} \\ 0 & 4.15 & 0 \\ 1 \cdot 10^{-2} & 0 & 4.16 \end{pmatrix} \tag{G.1}$$

$$\varepsilon_0 \approx 10 \tag{G.2}$$

From the experimental data of Ref. [159] we obtain for T=0 K dielectric constants in the range of $\varepsilon_\infty = 3.49..3.62$ showing a clear deviation from our calculations as we have similar observed for the band gap, too.

G.2 κ–Ga_2O_3

(a) Lattice parameters

	PBE	Expt. [140]
a (Å)	5.122	5.0557
b (Å)	8.801	8.68842
c (Å)	9.417	9.27585

(b) Atomic coordinates

	x	y	z
Ga1	0.17995	0.65144	0.99776
Ga2	0.81285	0.66190	0.30893
Ga3	0.19192	0.65075	0.58685
Ga4	0.67845	0.53124	0.79567
O1	0.97357	0.82575	0.42725
O2	0.52167	0.98748	0.43307
O3	0.65004	0.50332	0.20180
O4	0.15415	0.65894	0.19780
O5	0.85009	0.67144	0.67217
O6	0.52310	0.66673	0.93840

TABLE G.2: Structural properties of the κ-phase of Ga_2O_3 obtained from the optimization with the PBE functional. All atomic coordinates in (b) are given in fractional coordinates of the lattice vectors $\boldsymbol{a}$, $\boldsymbol{b}$, and $\boldsymbol{c}$. The lattice parameters of Ref. [140] were measured at 550°C and ambient pressure, where the PBE results refer to T=0 K (without zero-point effects).

The high-frequency dielectric tensor $\boldsymbol{\epsilon}_\infty$ used for the finite-size correction is calculated with the DFPT formalism at PBE level (for details of implementation cf. Ref [74]), but the tensor of the static dielectric constants has been approximated by a single constant ϵ_0 and is taken from experiment [158] of the β-phase, since no data is available for the κ-phase:

$$\varepsilon_\infty = \begin{pmatrix} 4.38 & 0 & 0 \\ 0 & 4.32 & 0 \\ 0 & & 4.30 \end{pmatrix} \tag{G.3}$$

$$\varepsilon_0 \approx 10 \tag{G.4}$$

G.3 Test of the supercell-size dependence for the hole polaron in κ–Ga_2O_3

To confirm the validity of our approach we explicitly tested the supercell-size dependence of the polaron properties for the κ-phase. We performed calculations up to supercells containing 480 atoms. The result is shown in Fig. G.1. We find a good agreement (within 0.1 eV) of the finite-size corrected energies with the actual dilute limit obtained from the linear fit of the data as a function of the inverse supercell size. The polaron energies for the $2 \times 1 \times 1$ supercell computed with HSE06(α=0.4) are shown as reference as well in Fig. G.1.

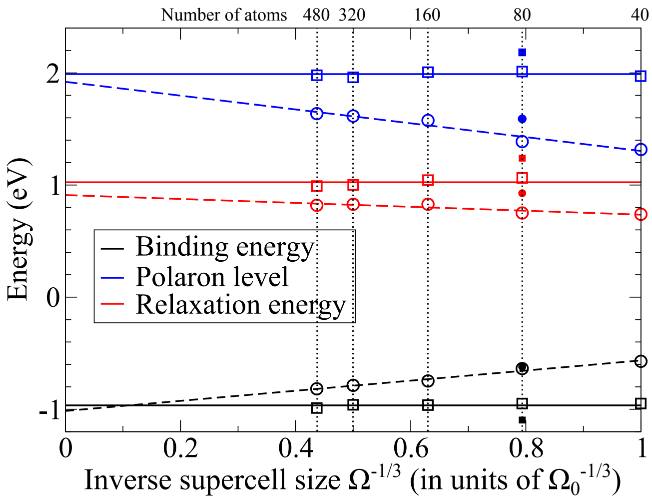

FIGURE G.1: The polaron binding energy E^0_{bind} (black line), the polaron level E_0 (blue line), and the relaxation energy $\Delta E^{\text{polaron}}$ (red line) as a function of the inverse supercell size $\Omega^{-1/3}$ given in units of the unit cell size $\Omega_0^{-1/3}$, calculated with the PBE functional. The dashed lines represent the calculated energies, whereas the solid lines are the long-range corrected energies. The filled symbols represent the results for the polaron energies calculated with HSE06(α=0.4).

Bibliography

[1] Kenji Nomura et al. "Room-temperature fabrication of transparent flexible thin-film transistors using amorphous oxide semiconductors". In: *Nature* 432.7016 (2004), pp. 488–492.
DOI: 10.1038/nature03090.

[2] S. David Jackson and Justin S. J. Hargreaves, eds. *Metal Oxide Catalysis*. Wiley-VCH Verlag GmbH & Co. KGaA, 2008.
DOI: 10.1002/9783527626113.

[3] Akira Fujishima and Kenichi Honda. "Electrochemical Photolysis of Water at a Semiconductor Electrode". In: *Nature* 238.5358 (1972), pp. 37–38.
DOI: 10.1038/238037a0.

[4] Rajan Jose, Velmurugan Thavasi, and Seeram Ramakrishna. "Metal Oxides for Dye-Sensitized Solar Cells". In: *Journal of the American Ceramic Society* 92.2 (2009), pp. 289–301.
DOI: 10.1111/j.1551-2916.2008.02870.x.

[5] Zhicai He et al. "Enhanced power-conversion efficiency in polymer solar cells using an inverted device structure". In: *Nature Photonics* 6.9 (2012), pp. 591–595.
DOI: 10.1038/nphoton.2012.190.

[6] LD Landau. "Über die Bewegung der Elektronen in Kristalgitter". In: *Phys. Z. Sowjetunion* 3 (1933), pp. 644–645.

[7] SI Pekar. "Autolocalization of the electron in an inertially polarizable dielectric medium". In: *Zh. Eksp. Teor. Fiz* 16 (1946), p. 335.

[8] H. Fröhlich. "Electrons in lattice fields". In: *Advances in Physics* 3.11 (1954), pp. 325–361.
DOI: 10.1080/00018735400101213.

[9] T. Holstein. "Studies of polaron motion". In: *Annals of Physics* 8.3 (1959), pp. 343–389.
DOI: 10.1016/0003-4916(59)90003-x.

[10] Otfried Madelung. *Semiconductors: data handbook*. Springer Science & Business Media, 2012.
DOI: 10.1007/978-3-642-18865-7.

[11] J. G. Traylor et al. "Lattice Dynamics of Rutile". In: *Phys. Rev. B* 3 (10 1971), pp. 3457–3472.
DOI: 10.1103/PhysRevB.3.3457.

[12] R. J. Gonzalez, R. Zallen, and H. Berger. “Infrared reflectivity and lattice fundamentals in anatase TiO_2s”. In: *Phys. Rev. B* 55 (11 1997), pp. 7014–7017.
DOI: 10.1103/PhysRevB.55.7014.

[13] M. Schubert et al. “Anisotropy, phonon modes, and free charge carrier parameters in monoclinic β-gallium oxide single crystals”. In: *Phys. Rev. B* 93 (12 2016), p. 125209.
DOI: 10.1103/PhysRevB.93.125209.

[14] Szczepan Chelkowski et al. “Dissociation, ionization, and Coulomb explosion of H_2^+ in an intense laser field by numerical integration of the time-dependent Schrödinger equation”. In: *Phys. Rev. A* 52 (4 1995), pp. 2977–2983.
DOI: 10.1103/PhysRevA.52.2977.

[15] M Born and K Huang. *Dynamical theories of crystal lattices*. Vol. 265. 1954, p. 266.

[16] Saul T. Epstein. “Ground-State Energy of a Molecule in the Adiabatic Approximation”. In: *The Journal of Chemical Physics* 44.2 (1966), pp. 836–837.
DOI: 10.1063/1.1726771.

[17] Chr. Møller and M. S. Plesset. “Note on an Approximation Treatment for Many-Electron Systems”. In: *Physical Review* 46.7 (1934), pp. 618–622.
DOI: 10.1103/physrev.46.618.

[18] Jiří Čížek. “On the Correlation Problem in Atomic and Molecular Systems. Calculation of Wavefunction Components in Ursell-Type Expansion Using Quantum-Field Theoretical Methods”. In: *The Journal of Chemical Physics* 45.11 (1966), pp. 4256–4266.
DOI: 10.1063/1.1727484.

[19] Isaiah Shavitt. “The Method of Configuration Interaction”. In: *Methods of Electronic Structure Theory*. Springer US, 1977, pp. 189–275.
DOI: 10.1007/978-1-4757-0887-5_6.

[20] P. Hohenberg and W. Kohn. “Inhomogeneous Electron Gas”. In: *Phys. Rev.* 136 (3B 1964), B864–B871.
DOI: 10.1103/PhysRev.136.B864.

[21] W. Kohn and L. J. Sham. “Self-Consistent Equations Including Exchange and Correlation Effects”. In: *Phys. Rev.* 140 (4A 1965), A1133–A1138.
DOI: 10.1103/PhysRev.140.A1133.

[22] Reiner M. Dreizler and Eberhard K. U. Gross. *Density Functional Theory*. Springer Berlin Heidelberg, 1990.
DOI: 10.1007/978-3-642-86105-5.

[23] Enrico Smargiassi and Paul A. Madden. “Orbital-free kinetic-energy functionals for first-principles molecular dynamics”. In: *Physical Review B* 49.8 (1994), pp. 5220–5226.
DOI: 10.1103/physrevb.49.5220.

[24] Weitao Yang, Paul W. Ayers, and Qin Wu. “Potential Functionals: Dual to Density Functionals and Solution to the v-Representability Problem”. In: *Phys. Rev. Lett.* 92 (14 2004), p. 146404.
DOI: 10.1103/PhysRevLett.92.146404.

[25] J. F. Janak. “Proof that $\frac{\partial E}{\partial n_i} = \epsilon$ in density-functional theory”. In: *Phys. Rev. B* 18 (12 1978), pp. 7165–7168.
DOI: 10.1103/PhysRevB.18.7165.

[26] John P. Perdew et al. “Density-Functional Theory for Fractional Particle Number: Derivative Discontinuities of the Energy”. In: *Phys. Rev. Lett.* 49 (23 1982), pp. 1691–1694.
DOI: 10.1103/PhysRevLett.49.1691.

[27] John P. Perdew and Mel Levy. “Physical Content of the Exact Kohn-Sham Orbital Energies: Band Gaps and Derivative Discontinuities”. In: *Phys. Rev. Lett.* 51 (20 1983), pp. 1884–1887.
DOI: 10.1103/PhysRevLett.51.1884.

[28] L. J. Sham and M. Schlüter. “Density-Functional Theory of the Energy Gap”. In: *Phys. Rev. Lett.* 51 (20 1983), pp. 1888–1891.
DOI: 10.1103/PhysRevLett.51.1888.

[29] Mel Levy, John P. Perdew, and Viraht Sahni. “Exact differential equation for the density and ionization energy of a many-particle system”. In: *Phys. Rev. A* 30 (5 1984), pp. 2745–2748.
DOI: 10.1103/PhysRevA.30.2745.

[30] J. P. Perdew and Alex Zunger. “Self-interaction correction to density-functional approximations for many-electron systems”. In: *Phys. Rev. B* 23 (10 1981), pp. 5048–5079.
DOI: 10.1103/PhysRevB.23.5048.

[31] Eli Kraisler and Leeor Kronik. “Piecewise Linearity of Approximate Density Functionals Revisited: Implications for Frontier Orbital Energies”. In: *Phys. Rev. Lett.* 110 (12 2013), p. 126403.
DOI: 10.1103/PhysRevLett.110.126403.

[32] A. R. Williams and U. von Barth. “Applications of Density Functional Theory to Atoms, Molecules, and Solids”. In: *Theory of the Inhomogeneous Electron Gas*. Springer US, 1983, pp. 189–308.
DOI: 10.1007/978-1-4899-0415-7_4.

[33] John P. Perdew et al. “Understanding band gaps of solids in generalized Kohn–Sham theory”. In: *Proceedings of the National Academy of Sciences* 114.11 (2017), pp. 2801–2806.
DOI: 10.1073/pnas.1621352114.

[34] Vincenzo Fiorentini and Alfonso Baldereschi. “Dielectric scaling of the self-energy scissor operator in semiconductors and insulators”. In: *Phys. Rev. B* 51 (23 1995), pp. 17196–17198.
DOI: 10.1103/PhysRevB.51.17196.

[35] John P. Perdew, Kieron Burke, and Matthias Ernzerhof. "Generalized Gradient Approximation Made Simple". In: *Phys. Rev. Lett.* 77 (18 1996), pp. 3865–3868. DOI: 10.1103/PhysRevLett.77.3865.

[36] Matthias Ernzerhof and Gustavo E. Scuseria. "Assessment of the Perdew-Burke-Ernzerhof exchange-correlation functional". In: *The Journal of Chemical Physics* 110.11 (1999), pp. 5029–5036. DOI: 10.1063/1.478401.

[37] David C. Patton, Dirk V. Porezag, and Mark R. Pederson. "Simplified generalized-gradient approximation and anharmonicity: Benchmark calculations on molecules". In: *Phys. Rev. B* 55 (12 1997), pp. 7454–7459. DOI: 10.1103/PhysRevB.55.7454.

[38] Aleš Zupan et al. "Pressure-induced phase transitions in solid Si, SiO_2, and Fe: Performance of local-spin-density and generalized-gradient-approximation density functionals". In: *Phys. Rev. B* 58 (17 1998), 11266 –11272. DOI: 10.1103/PhysRevB.58.11266.

[39] Axel D. Becke. "A new mixing of Hartree–Fock and local density-functional theories". In: *The Journal of Chemical Physics* 98.2 (1993), pp. 1372–1377. DOI: 10.1063/1.464304.

[40] John P. Perdew, Matthias Ernzerhof, and Kieron Burke. "Rationale for mixing exact exchange with density functional approximations". In: *The Journal of Chemical Physics* 105.22 (1996), pp. 9982–9985. DOI: http://dx.doi.org/10.1063/1.472933.

[41] J Harris and R O Jones. "The surface energy of a bounded electron gas". In: *Journal of Physics F: Metal Physics* 4.8 (1974), pp. 1170–1186. DOI: 10.1088/0305-4608/4/8/013.

[42] D.C. Langreth and J.P. Perdew. "The exchange-correlation energy of a metallic surface". In: *Solid State Communications* 17.11 (1975), pp. 1425–1429. DOI: 10.1016/0038-1098(75)90618-3.

[43] O. Gunnarsson and B. I. Lundqvist. "Exchange and correlation in atoms, molecules, and solids by the spin-density-functional formalism". In: *Phys. Rev. B* 13 (10 1976), pp. 4274–4298. DOI: 10.1103/PhysRevB.13.4274.

[44] Stephan Lany and Alex Zunger. "Polaronic hole localization and multiple hole binding of acceptors in oxide wide-gap semiconductors". In: *Phys. Rev. B* 80 (8 2009), p. 085202. DOI: 10.1103/PhysRevB.80.085202.

[45] Viktor Atalla et al. "Hybrid density functional theory meets quasiparticle calculations: A consistent electronic structure approach". In: *Phys. Rev. B* 88 (16 2013), p. 165122. DOI: 10.1103/PhysRevB.88.165122.

[46] Viktor Atalla et al. "Enforcing the linear behavior of the total energy with hybrid functionals: Implications for charge transfer, interaction energies, and the random-phase approximation". In: *Phys. Rev. B* 94 (3 2016), p. 035140. DOI: `10.1103/PhysRevB.94.035140`.

[47] Norina A. Richter et al. "Concentration of Vacancies at Metal-Oxide Surfaces: Case Study of MgO(100)". In: *Physical Review Letters* 111.4 (2013). DOI: `10.1103/physrevlett.111.045502`.

[48] Audrius Alkauskas, Peter Broqvist, and Alfredo Pasquarello. "Defect levels through hybrid density functionals: Insights and applications". In: *physica status solidi (b)* 248.4 (2011), pp. 775–789. DOI: `10.1002/pssb.201046195`.

[49] Miguel A. L. Marques et al. "Density-based mixing parameter for hybrid functionals". In: *Phys. Rev. B* 83 (3 2011), p. 035119. DOI: `10.1103/PhysRevB.83.035119`.

[50] Jonathan H. Skone, Marco Govoni, and Giulia Galli. "Self-consistent hybrid functional for condensed systems". In: *Physical Review B* 89.19 (2014). DOI: `10.1103/physrevb.89.195112`.

[51] Lars Hedin. "New Method for Calculating the One-Particle Green's Function with Application to the Electron-Gas Problem". In: *Physical Review* 139.3A (1965), A796–A823. DOI: `10.1103/physrev.139.a796`.

[52] Jochen Heyd, Gustavo E. Scuseria, and Matthias Ernzerhof. "Hybrid functionals based on a screened Coulomb potential". In: *The Journal of Chemical Physics* 118.18 (2003), pp. 8207–8215. DOI: `http://dx.doi.org/10.1063/1.1564060`.

[53] Jochen Heyd, Gustavo E. Scuseria, and Matthias Ernzerhof. "Erratum: Hybrid functionals based on a screened Coulomb potential, J. Chem. Phys.118, 8207 (2003)". In: *The Journal of Chemical Physics* 124.21, 219906 (2006). DOI: `http://dx.doi.org/10.1063/1.2204597`.

[54] P. J. Stephens et al. "Ab Initio Calculation of Vibrational Absorption and Circular Dichroism Spectra Using Density Functional Force Fields". In: *The Journal of Physical Chemistry* 98.45 (1994), pp. 11623–11627. DOI: `10.1021/j100096a001`.

[55] Yong Xu et al. "Space-Charge Transfer in Hybrid Inorganic-Organic Systems". In: *Phys. Rev. Lett.* 111 (22 2013), p. 226802. DOI: `10.1103/PhysRevLett.111.226802`.

[56] Roi Baer and Daniel Neuhauser. "Density Functional Theory with Correct Long-Range Asymptotic Behavior". In: *Phys. Rev. Lett.* 94 (4 2005), p. 043002. DOI: `10.1103/PhysRevLett.94.043002`.

[57] Ester Livshits and Roi Baer. "A well-tempered density functional theory of electrons in molecules". In: *Physical Chemistry Chemical Physics* 9.23 (2007), p. 2932. DOI: `10.1039/b617919c`.

[58] Oleg A. Vydrov et al. “Importance of short-range versus long-range Hartree-Fock exchange for the performance of hybrid density functionals”. In: *The Journal of Chemical Physics* 125.7 (2006), p. 074106.
DOI: 10.1063/1.2244560.

[59] Volker Blum et al. “Ab initio molecular simulations with numeric atom-centered orbitals”. In: *Computer Physics Communications* 180.11 (2009), pp. 2175 –2196.
ISSN: 0010-4655.
DOI: http://dx.doi.org/10.1016/j.cpc.2009.06.022.

[60] V. Havu et al. “Efficient O(N) integration for all-electron electronic structure calculation using numeric basis functions”. In: *Journal of Computational Physics* 228.22 (2009), pp. 8367–8379.
DOI: 10.1016/j.jcp.2009.08.008.

[61] VI Lebedev and DN Laikov. “A quadrature formula for the sphere of the 131st algebraic order of accuracy”. In: *Doklady. Mathematics*. Vol. 59. MAIK Nauka/Interperiodica. 1999, pp. 477–481.

[62] A. D. Becke. “A multicenter numerical integration scheme for polyatomic molecules”. In: *The Journal of Chemical Physics* 88.4 (1988),
2547–2553.
DOI: 10.1063/1.454033.

[63] B. Delley. “An all-electron numerical method for solving the local density functional for polyatomic molecules”. In: *The Journal of Chemical Physics* 92.1 (1990), pp. 508–517.
DOI: 10.1063/1.458452.

[64] P. Pulay. “Ab initiocalculation of force constants and equilibrium geometries in polyatomic molecules”. In: *Molecular Physics* 17.2 (1969), pp. 197–204.
DOI: 10.1080/00268976900100941.

[65] B. Delley. “Analytic energy derivatives in the numerical local-density-functional approach”. In: *The Journal of Chemical Physics* 94.11 (1991), pp. 7245–7250.
DOI: 10.1063/1.460208.

[66] P. P. Ewald. “Die Berechnung optischer und elektrostatischer Gitterpotentiale”. In: *Annalen der Physik* 369.3 (1921), pp. 253–287.
DOI: 10.1002/andp.19213690304.

[67] Bernard Delley. “Fast Calculation of Electrostatics in Crystals and Large Molecules”. In: *The Journal of Physical Chemistry* 100.15 (1996), pp. 6107–6110.
DOI: 10.1021/jp952713n.

[68] A Marek et al. “The ELPA library: scalable parallel eigenvalue solutions for electronic structure theory and computational science”. In: *Journal of Physics: Condensed Matter* 26.21 (2014), p. 213201.
DOI: 10.1088/0953-8984/26/21/213201.

[69] Xinguo Ren et al. "Resolution-of-identity approach to Hartree–Fock, hybrid density functionals, RPA, MP2 and GW with numeric atom-centered orbital basis functions". In: *New Journal of Physics* 14.5 (2012), p. 053020.
DOI: `10.1088/1367-2630/14/5/053020`.

[70] Sergey V. Levchenko et al. "Hybrid functionals for large periodic systems in an all-electron, numeric atom-centered basis framework". In: *Computer Physics Communications* 192 (2015), pp. 60 –69. ISSN: 0010-4655.
DOI: `http://dx.doi.org/10.1016/j.cpc.2015.02.021`.

[71] Feliciano Giustino. "Electron-phonon interactions from first principles". In: *Rev. Mod. Phys.* 89 (1 2017), p. 015003.
DOI: `10.1103/RevModPhys.89.015003`.

[72] Atsushi Togo and Isao Tanaka. "First principles phonon calculations in materials science". In: *Scripta Materialia* 108 (2015), pp. 1–5.
DOI: `10.1016/j.scriptamat.2015.07.021`.

[73] Xavier Gonze. "Perturbation expansion of variational principles at arbitrary order". In: *Phys. Rev. A* 52 (2 1995), pp. 1086–1095.
DOI: `10.1103/PhysRevA.52.1086`.

[74] Honghui Shang et al. "Lattice dynamics calculations based on density-functional perturbation theory in real space". In: *Computer Physics Communications* 215 (2017), pp. 26–46.
DOI: `10.1016/j.cpc.2017.02.001`.

[75] Robert M. Pick, Morrel H. Cohen, and Richard M. Martin. "Microscopic Theory of Force Constants in the Adiabatic Approximation". In: *Physical Review B* 1.2 (1970), pp. 910–920.
DOI: `10.1103/physrevb.1.910`.

[76] P B Allen and V Heine. "Theory of the temperature dependence of electronic band structures". In: *Journal of Physics C: Solid State Physics* 9.12 (1976), pp. 2305–2312.
DOI: `10.1088/0022-3719/9/12/013`.

[77] P. B. Allen and M. Cardona. "Temperature dependence of the direct gap of Si and Ge". In: *Phys. Rev. B* 27 (8 1983), pp. 4760–4769.
DOI: `10.1103/PhysRevB.27.4760`.

[78] Feliciano Giustino, Steven G. Louie, and Marvin L. Cohen. "Electron-Phonon Renormalization of the Direct Band Gap of Diamond". In: *Phys. Rev. Lett.* 105 (26 2010), p. 265501.
DOI: `10.1103/PhysRevLett.105.265501`.

[79] G. Antonius et al. "Dynamical and anharmonic effects on the electron-phonon coupling and the zero-point renormalization of the electronic structure". In: *Phys. Rev. B* 92 (8 2015), p. 085137.
DOI: `10.1103/PhysRevB.92.085137`.

[80] Guo meng Zhao et al. "Evidence for polaronic supercarriers in the copper oxide superconductors La2–xSr x CuO4". In: *Nature* 385.6613 (1997), pp. 236–239. DOI: 10.1038/385236a0.

[81] A. S. Alexandrov, J. Ranninger, and S. Robaszkiewicz. "Bipolaronic superconductivity: Thermodynamics, magnetic properties, and possibility of existence in real substances". In: *Phys. Rev. B* 33 (7 1986), pp. 4526–4542. DOI: 10.1103/PhysRevB.33.4526.

[82] R. P. Feynman. "Slow Electrons in a Polar Crystal". In: *Phys. Rev.* 97 (3 1955), pp. 660–665. DOI: 10.1103/PhysRev.97.660.

[83] R. P. Feynman et al. "Mobility of Slow Electrons in a Polar Crystal". In: *Phys. Rev.* 127 (4 1962), pp. 1004–1017. DOI: 10.1103/PhysRev.127.1004.

[84] W. Becker, B. Gerlach, and H. Schliffke. "Monte Carlo calculation of the ground-state energy of an optical polaron". In: *Phys. Rev. B* 28 (10 1983), pp. 5735–5738. DOI: 10.1103/PhysRevB.28.5735.

[85] A. S. Mishchenko et al. "Diagrammatic quantum Monte Carlo study of the Fröhlich polaron". In: *Phys. Rev. B* 62 (10 2000), pp. 6317–6336. DOI: 10.1103/PhysRevB.62.6317.

[86] Gerald D. Mahan. *Many-Particle Physics*. Springer US, 2000. DOI: 10.1007/978-1-4757-5714-9.

[87] J. Appel. "Polarons". In: *Solid State Physics*. Elsevier, 1968, pp. 193–391. DOI: 10.1016/s0081-1947(08)60741-9.

[88] Jozef T Devreese and Alexandre S Alexandrov. "Fröhlich polaron and bipolaron: recent developments". In: *Reports on Progress in Physics* 72.6 (2009), p. 066501. DOI: 10.1088/0034-4885/72/6/066501.

[89] JT Devreese. "Fröhlich Polarons. Lecture course including detailed theoretical derivations". In: *arXiv preprint arXiv:1611.06122* (2016).

[90] Marilyn M. Morrell, Robert G. Parr, and Mel Levy. "Calculation of ionization potentials from density matrices and natural functions, and the longrange behavior of natural orbitals and electron density". In: *The Journal of Chemical Physics* 62.2 (1975), pp. 549–554. DOI: 10.1063/1.430509.

[91] Satoru J. Miyake. "The Ground State of the Optical Polaron in the Strong-Coupling Case". In: *Journal of the Physical Society of Japan* 41.3 (1976), pp. 747–752. DOI: 10.1143/JPSJ.41.747.

[92] Stephen J. Nettel. "Interaction of a Polarizable Potassium Chloride Crystal with a Valence-Band Hole". In: *Phys. Rev.* 121 (2 1961), pp. 425–435. DOI: 10.1103/PhysRev.121.425.

[93] Matthias Scheffler, Jean Pol Vigneron, and Giovanni B. Bachelet. "Total-energy gradients and lattice distortions at point defects in semiconductors". In: *Physical Review B* 31.10 (1985), pp. 6541–6551.
DOI: 10.1103/physrevb.31.6541.

[94] Matthias Scheffler, Jean Pol Vigneron, and Giovanni B. Bachelet. "Tractable Approach for Calculating Lattice Distortions around Simple Defects in Semiconductors: Application to the Single Donor Ge in GaP". In: *Phys. Rev. Lett.* 49 (24 1982), pp. 1765–1768.
DOI: 10.1103/PhysRevLett.49.1765.

[95] A L Shluger et al. "Self-trapping holes and excitons in the bulk and on the (100) surfaces of MgO". In: *Journal of Physics: Condensed Matter* 3.41 (1991), pp. 8027–8036.
DOI: 10.1088/0953-8984/3/41/002.

[96] Emanuele Finazzi et al. "Excess electron states in reduced bulk anatase TiO_2: Comparison of standard GGA, GGA+U, and hybrid DFT calculations". In: *The Journal of Chemical Physics* 129.15 (2008), p. 154113.
DOI: 10.1063/1.2996362.

[97] J. B. Varley et al. "Role of self-trapping in luminescence and p-type conductivity of wide-band-gap oxides". In: *Phys. Rev. B* 85 (8 2012), p. 081109.
DOI: 10.1103/PhysRevB.85.081109.

[98] G. Makov and M. C. Payne. "Periodic boundary conditions in *ab initio* calculations". In: *Phys. Rev. B* 51 (7 1995), pp. 4014–4022.
DOI: 10.1103/PhysRevB.51.4014.

[99] Christoph Freysoldt, Jörg Neugebauer, and Chris G. Van de Walle. "Fully *Ab Initio* Finite-Size Corrections for Charged-Defect Supercell Calculations". In: *Phys. Rev. Lett.* 102 (1 2009), p. 016402.
DOI: 10.1103/PhysRevLett.102.016402.

[100] Hannu-Pekka Komsa, Tapio T. Rantala, and Alfredo Pasquarello. "Finite-size supercell correction schemes for charged defect calculations". In: *Phys. Rev. B* 86 (4 2012), p. 045112.
DOI: 10.1103/PhysRevB.86.045112.

[101] Carla Verdi and Feliciano Giustino. "Fröhlich Electron-Phonon Vertex from First Principles". In: *Physical Review Letters* 115.17 (2015).
DOI: 10.1103/physrevlett.115.176401.

[102] H. Fock, B. Kramer, and H. Büttner. "Polarons and effective electron-hole interaction in anisotropic polar crystals". In: *physica status solidi (b)* 67.1 (1975), pp. 199–206.
DOI: 10.1002/pssb.2220670118.

[103] Christoph Freysoldt, Jörg Neugebauer, and Chris G. Van de Walle. "Electrostatic interactions between charged defects in supercells". In: *physica status solidi (b)* 248.5 (2011), pp. 1067–1076. ISSN: 1521-3951.
DOI: 10.1002/pssb.201046289.

[104] Stephan Lany. "Predicting polaronic defect states by means of generalized Koopmans density functional calculations". In: *physica status solidi (b)* 248.5 (2011), pp. 1052–1060. ISSN: 1521-3951.
DOI: 10.1002/pssb.201046274.

[105] Matthias Dauth et al. "Piecewise linearity in the *GW* approximation for accurate quasiparticle energy predictions". In: *Phys. Rev. B* 93 (12 2016), p. 121115.
DOI: 10.1103/PhysRevB.93.121115.

[106] Sivan Refaely-Abramson, Roi Baer, and Leeor Kronik. "Fundamental and excitation gaps in molecules of relevance for organic photovoltaics from an optimally tuned range-separated hybrid functional". In: *Phys. Rev. B* 84 (7 2011), p. 075144.
DOI: 10.1103/PhysRevB.84.075144.

[107] Tamar Stein et al. "Fundamental Gaps in Finite Systems from Eigenvalues of a Generalized Kohn-Sham Method". In: *Phys. Rev. Lett.* 105 (26 2010), p. 266802.
DOI: 10.1103/PhysRevLett.105.266802.

[108] Babak Sadigh, Paul Erhart, and Daniel Åberg. "Variational polaron self-interaction-corrected total-energy functional for charge excitations in insulators". In: *Phys. Rev. B* 92 (7 2015), p. 075202.
DOI: 10.1103/PhysRevB.92.075202.

[109] Pawe Zawadzki, Karsten Wedel Jacobsen, and Jan Rossmeisl. "Electronic hole localization in rutile and anatase TiO2 Self-interaction correction in -SCF DFT". In: *Chemical Physics Letters* 506.1 (2011), pp. 42 –45. ISSN: 0009-2614.
DOI: 10.1016/j.cplett.2011.03.001.

[110] S. R. Bahn and K. W. Jacobsen. "An object-oriented scripting interface to a legacy electronic structure code". English. In: *Comput. Sci. Eng.* 4.3 (2002), pp. 56–66. ISSN: 1521-9615.
DOI: 10.1109/5992.998641.

[111] L.F. Lemmens and J.T. Devresse. "The 1: 2: 3: 4 theorem and the ground state of free polarons". In: *Solid State Communications* 12.10 (1973), pp. 1067–1069. ISSN: 0038-1098.
DOI: 10.1016/0038-1098(73)90038-0.

[112] Martin Setvin et al. "Direct View at Excess Electrons in TiO_2 Rutile and Anatase". In: *Phys. Rev. Lett.* 113 (8 2014), p. 086402.
DOI: 10.1103/PhysRevLett.113.086402.

[113] N. Aaron Deskins and Michel Dupuis. "Electron transport via polaron hopping in bulk TiO_2: A density functional theory characterization". In: *Phys. Rev. B* 75 (19 2007), p. 195212.
DOI: 10.1103/PhysRevB.75.195212.

[114] Clelia Spreafico and Joost VandeVondele. "The nature of excess electrons in anatase and rutile from hybrid DFT and RPA". In: *Phys. Chem. Chem. Phys.* 16 (47 2014), pp. 26144–26152.
DOI: 10.1039/C4CP03981E.

[115] A. Janotti et al. “Dual behavior of excess electrons in rutile TiO2”. In: *physica status solidi (RRL) - Rapid Research Letters* 7.3 (2013), pp. 199–203. DOI: 10.1002/pssr.201206464.

[116] Z. A. Rachko and J. A. Valbis. “Luminescence of Free and Relaxed Excitons in MgO”. In: *Physica Status Solidi (b)* 93.1 (1979), pp. 161–166. DOI: 10.1002/pssb.2220930118.

[117] J. Pascual, J. Camassel, and H. Mathieu. “Fine structure in the intrinsic absorption edge of TiO_2”. In: *Phys. Rev. B* 18 (10 1978), pp. 5606–5614. DOI: 10.1103/PhysRevB.18.5606.

[118] Nadica D. Abazović et al. “Photoluminescence of Anatase and Rutile TiO2 Particles”. In: *The Journal of Physical Chemistry B* 110.50 (2006), pp. 25366–25370. DOI: 10.1021/jp064454f.

[119] Hendrik Kathrein and Friedemann Freund. “Electrical conductivity of magnesium oxide single crystal below 1200 K”. In: *Journal of Physics and Chemistry of Solids* 44.3 (1983), pp. 177–186. DOI: 10.1016/0022-3697(83)90052-5.

[120] Michael Grätzel. “Photoelectrochemical cells”. In: *Nature* 414.6861 (2001), pp. 338–344. DOI: 10.1038/35104607.

[121] Rong Wang et al. “Light-induced amphiphilic surfaces”. In: *Nature* 388.6641 (1997), pp. 431–432. DOI: 10.1038/41233.

[122] B Montanari and N.M Harrison. “Lattice dynamics of TiO2 rutile: influence of gradient corrections in density functional calculations”. In: *Chemical Physics Letters* 364.5-6 (2002), pp. 528–534. DOI: 10.1016/s0009-2614(02)01401-x.

[123] C. J. Howard, T. M. Sabine, and F. Dickson. “Structural and thermal parameters for rutile and anatase”. In: *Acta Crystallographica Section B Structural Science* 47.4 (1991), pp. 462–468. DOI: 10.1107/s010876819100335x.

[124] Jinfeng Zhang et al. “New understanding of the difference of photocatalytic activity among anatase, rutile and brookite TiO2”. In: *Phys. Chem. Chem. Phys.* 16.38 (2014), pp. 20382–20386. DOI: 10.1039/c4cp02201g.

[125] Maofeng Dou and Clas Persson. “Comparative study of rutile and anatase SnO2 and TiO2: Band-edge structures, dielectric functions, and polaron effects”. In: *Journal of Applied Physics* 113.8 (2013), p. 083703. DOI: 10.1063/1.4793273.

[126] H. Tang et al. “Urbach tail of anatase TiO_2”. In: *Phys. Rev. B* 52 (11 1995), pp. 7771–7774. DOI: 10.1103/PhysRevB.52.7771.

[127] I.G. Austin and N.F. Mott. "Polarons in crystalline and non-crystalline materials". In: *Advances in Physics* 18.71 (1969), pp. 41–102.
DOI: 10.1080/00018736900101267.

[128] D. C. Cronemeyer. "Infrared Absorption of Reduced Rutile TiO_2 Single Crystals". In: *Phys. Rev.* 113 (5 1959), pp. 1222–1226.
DOI: 10.1103/PhysRev.113.1222.

[129] H. Tang et al. "Photoluminescence in TiO2 anatase single crystals". In: *Solid State Communications* 87.9 (1993), pp. 847–850.
DOI: 10.1016/0038-1098(93)90427-o.

[130] L. Forro et al. "High mobilityn-type charge carriers in large single crystals of anatase (TiO2)". In: *Journal of Applied Physics* 75.1 (1994), pp. 633–635.
DOI: 10.1063/1.355801.

[131] Tim Luttrell et al. "Why is anatase a better photocatalyst than rutile? - Model studies on epitaxial TiO2 films". In: *Scientific Reports* 4.1 (2014).
DOI: 10.1038/srep04043.

[132] Masataka Higashiwaki et al. "Gallium oxide (Ga2O3) metal-semiconductor field-effect transistors on single-crystal β-Ga2O3 (010) substrates". In: *Applied Physics Letters* 100.1 (2012), p. 013504.
DOI: 10.1063/1.3674287.

[133] Masataka Higashiwaki et al. "Depletion-mode Ga2O3 metal-oxide-semiconductor field-effect transistors on β-Ga2O3 (010) substrates and temperature dependence of their device characteristics". In: *Applied Physics Letters* 103.12 (2013), p. 123511.
DOI: 10.1063/1.4821858.

[134] Takayoshi Oshima et al. "Vertical Solar-Blind Deep-Ultraviolet Schottky Photodetectors Based on β-Ga2O3Substrates". In: *Applied Physics Express* 1.1 (2008), p. 011202.
DOI: 10.1143/apex.1.011202.

[135] Yoshihiro Kokubun et al. "Sol-gel prepared β-Ga2O3 thin films for ultraviolet photodetectors". In: *Applied Physics Letters* 90.3 (2007), p. 031912.
DOI: 10.1063/1.2432946.

[136] Naoyuki Ueda et al. "Synthesis and control of conductivity of ultraviolet transmitting β-Ga2O3 single crystals". In: *Applied Physics Letters* 70.26 (1997), pp. 3561–3563.
DOI: 10.1063/1.119233.

[137] Masahiro Orita et al. "Deep-ultraviolet transparent conductive β-Ga_2O_3 thin films". In: *Applied Physics Letters* 77.25 (2000), pp. 4166–4168.
DOI: 10.1063/1.1330559.

[138] H. H. Tippins. "Optical Absorption and Photoconductivity in the Band Edge of $\beta - \mathrm{Ga_2O_3}$". In: *Phys. Rev.* 140 (1A 1965), A316–A319.
DOI: 10.1103/PhysRev.140.A316.

[139] Encarnación G. Víllora et al. “Electrical conductivity and carrier concentration control in β-Ga2O3 by Si doping”. In: *Applied Physics Letters* 92.20 (2008), p. 202120.
DOI: 10.1063/1.2919728.

[140] Helen Y. Playford et al. “Structures of Uncharacterised Polymorphs of Gallium Oxide from Total Neutron Diffraction”. In: *Chemistry - A European Journal* 19.8 (2013), pp. 2803–2813.
DOI: 10.1002/chem.201203359.

[141] Rustum Roy, V. G. Hill, and E. F. Osborn. “Polymorphism of Ga_2O_3 and the System Ga_2O_3—H_2O”. In: *Journal of the American Chemical Society* 74.3 (1952), pp. 719–722.
DOI: 10.1021/ja01123a039.

[142] Marco D. Santia, Nandan Tandon, and J. D. Albrecht. “Lattice thermal conductivity in β-Ga2O3 from first principles”. In: *Applied Physics Letters* 107.4 (2015), p. 041907.
DOI: 10.1063/1.4927742.

[143] T. Harwig, F. Kellendonk, and S. Slappendel. “The ultraviolet luminescence of β-galliumsesquioxide”. In: *Journal of Physics and Chemistry of Solids* 39.6 (1978), pp. 675–680.
DOI: 10.1016/0022-3697(78)90183-x.

[144] Kiyoshi Shimamura et al. “Excitation and photoluminescence of pure and Si-doped β-Ga2O3 single crystals”. In: *Applied Physics Letters* 92.20 (2008), p. 201914.
DOI: 10.1063/1.2910768.

[145] T. Harwig and F. Kellendonk. “Some observations on the photoluminescence of doped β-galliumsesquioxide”. In: *Journal of Solid State Chemistry* 24.3-4 (1978), pp. 255–263.
DOI: 10.1016/0022-4596(78)90017-8.

[146] Laurent Binet and Didier Gourier. “ORIGIN OF THE BLUE LUMINESCENCE OF β-Ga2O3”. In: *Journal of Physics and Chemistry of Solids* 59.8 (1998), pp. 1241–1249.
DOI: 10.1016/s0022-3697(98)00047-x.

[147] Encarnación G. Víllora et al. “Cathodoluminescence of undoped β–Ga_2O_3 single crystals”. In: *Solid State Communications* 120.11 (2001), pp. 455–458.
DOI: 10.1016/s0038-1098(01)00409-4.

[148] T. Onuma et al. “Correlation between blue luminescence intensity and resistivity in β-Ga2O3 single crystals”. In: *Applied Physics Letters* 103.4 (2013), p. 041910.
DOI: 10.1063/1.4816759.

[149] Hikmet Sezen et al. “Evidence for photogenerated intermediate hole polarons in ZnO”. In: *Nature Communications* 6.1 (2015).
DOI: 10.1038/ncomms7901.

[150] G.R. Allcock. “On the polaron rest energy and effective mass”. In: *Advances in Physics* 5.20 (1956), pp. 412–451.
DOI: 10.1080/00018735600101215.

[151] Christoph Janowitz et al. “Experimental electronic structure of In2O3 and Ga2O3”. In: *New Journal of Physics* 13.8 (2011), p. 085014.
DOI: 10.1088/1367-2630/13/8/085014.

[152] J. M. Luttinger and W. Kohn. “Motion of Electrons and Holes in Perturbed Periodic Fields”. In: *Phys. Rev.* 97 (4 1955), pp. 869–883.
DOI: 10.1103/PhysRev.97.869.

[153] Claudia Ambrosch-Draxl and Jorge O. Sofo. “Linear optical properties of solids within the full-potential linearized augmented planewave method”. In: *Computer Physics Communications* 175.1 (2006), pp. 1–14.
DOI: 10.1016/j.cpc.2006.03.005.

[154] K. V. KRISHNA RAO, S. V. NAGENDER NAIDU, and LEELA IYENGAR. “Thermal Expansion of Rutile and Anatase”. In: *Journal of the American Ceramic Society* 53.3 (1970), pp. 124–126.
DOI: 10.1111/j.1151-2916.1970.tb12051.x.

[155] Rebecca A. Parker. “Static Dielectric Constant of Rutile (TiO_2), 1.6 – 1060°K”. In: *Phys. Rev.* 124 (6 1961), pp. 1719–1722.
DOI: 10.1103/PhysRev.124.1719.

[156] T. A. Davis and K. Vedam. “Pressure Dependence of the Refractive Indices of the Tetragonal Crystals: ADP, KDP, CaMoO_4, CaWO_4, and Rutile”. In: *Journal of the Optical Society of America* 58.11 (1968), p. 1446.
DOI: 10.1364/josa.58.001446.

[157] Kristina E. Lipinska-Kalita et al. “Equation of state of gallium oxide to 70 GPa: Comparison of quasihydrostatic and nonhydrostatic compression”. In: *Phys. Rev. B* 77 (9 2008), p. 094123.
DOI: 10.1103/PhysRevB.77.094123.

[158] M. Passlack et al. “Ga2O3films for electronic and optoelectronic applications”. In: *Journal of Applied Physics* 77.2 (1995), pp. 686–693.
DOI: 10.1063/1.359055.

[159] Indranil Bhaumik et al. “Temperature-dependent index of refraction of monoclinic Ga2O3 single crystal”. In: *Applied Optics* 50.31 (2011), p. 6006.
DOI: 10.1364/ao.50.006006.

Selbstständigkeitserklärung

Ich erkläre, dass ich die Dissertation selbständig und nur unter Verwendung der von mir gemäß § 7 Abs. 3 der Promotionsordnung der Mathematisch-Naturwissenschaftlichen Fakultät, veröffentlicht im Amtlichen Mitteilungsblatt der Humboldt-Universität zu Berlin Nr. 126/2014 am 18.11.2014 angegebenen Hilfsmittel angefertigt habe.

Ort, Datum:
09.06.2018

Unterschrift:
Sebastian Kokott